I. SMALL ANGLE SCATTERING OF RADIATION

II. MOLECULAR EMISSION LINES AROUND EVOLVED STARS

Thesis by

Charles Alcock

In partial fulfillment of the

requirements for the degree of

Doctor of Philosophy

California Institute of Technology

Pasadena, California

1978

(Submitted September 30, 1977)

ACKNOWLEDGEMENTS

Individual help on each of the projects described here is acknowledged in each of the papers. What is missing from these 'thank you's' is the gratitude I feel to my advisor, Peter Goldreich, for a superb introduction to creative science; to my friends - in particular Janet and John Bloom, Anneila and Wal Sargent, and Kaaren and David Slauson - for their support; to my parents, for always expecting that I would 'do something'; and most of all to my wife, Anna Żytkow, for her encouragement when I most needed it.

ABSTRACT

This dissertation is in two Parts. Part I consists of a paper on the effect of small angle scattering on a pulse of radiation, and an analysis of the particular case of X-rays scattering off interstellar grains. Part II concerns the excitation of SiO emission lines around evolved stars. There are two papers, the first on 'thermal' emission lines and the second on maser emission lines. Each paper has its own abstract.

TABLE OF CONTENTS

PART I

Paper I. The Effect of Small Angle Scattering on a Pulse of Radiation with an Application to X-ray Bursts (in collaboration with Stephen Hatchett) Page 1

PART II

Paper 2. Molecular Emission Lines From Expanding Envelopes Around Evolved Stars I. Non-Maser Emission Lines (in collaboration with Mark Morris) Page 47

Paper 3. Molecular Emission Lines From Expanding Envelopes Around Evolved Stars II. Maser Emission lines (in collaboration with Mark Morris) Page 84

PAPER 1

THE EFFECTS OF SMALL ANGLE SCATTERING ON A PULSE OF RADIATION WITH AN APPLICATION OF X-RAY BURSTS AND INTERSTELLAR DUST

CHARLES ALCOCK and STEPHEN HATCHETT

Division of Physics, Mathematics and Astronomy

California Institute of Technology, Pasadena, California 91125

*Supported in part by the National Science Foundation [AST76-80801] and [MPS72-05045-A02].

ABSTRACT

We have analyzed in detail the general problem of the propagation of a pulse of radiation through a uniform medium containing small angle scatterers. Simple expressions for the first moment of the arrival time delay and for the second and fourth moments of the arrival angle of the pulse photons are given, valid for any optical depth. Using the first two of these we find a simple method of distance determination. Joint and individual distribution functions for arrival time and angle are derived in the small and large optical depth limits. An exponential tail in the arrival time distribution is characteristic in both limits. The analysis has been applied to a burst of x-rays from a source near the galactic center propagating through the dust of the interstellar medium. The grains responsible for interstellar reddening can have very little observable effect. However, the observed lengths, energy dependence, and variability of the burst tails can be readily accounted for by a population of large $\sim 3\mu$ grains. We derive useful constraints on the grain distribution from observations of the burst tails.

Key Words: distance determination, grains, scattering, x-rays, x-ray bursts

I. INTRODUCTION

Since the first detections of intense bursts of cosmic x-rays (Babushkina et al. 1975; Grindlay et al. 1976) a large number of x-ray burst sources have been discovered. Comprehensive reviews of the observations have recently appeared (Lewin 1977; Clark 1976). The interested reader is urged to consult those reviews and the references therein, since we summarize below only those data relevant to our discussion.

The majority of burst sources have been observed in the range 1.2-30 keV; the burst activity is most prominent in the range 3-20 keV. A typical burst has a rise time of 1-2 sec, a "peak" lasting a few seconds, followed by an "exponential tail" with a decay time of 10-20 sec. In most sources the tail is noticeably longer in the lower energy channels – that is, the burst spectrum softens in the tail. A well-documented, typical source is MXB 1728-34 for which a seven burst composite (Lewin et al. 1976) displays the characteristic behavior described above. It was noted for this source that after the "burst" of $\sim$ 20 sec the background was enhanced, the data suggesting a second underlying tail with a time constant of 50-200 sec. This longer tail is most pronounced in the lowest energy channels.

The distribution of burst sources on the sky is strongly concentrated around the galactic center and flattened toward the plane, strongly suggesting that the space distribution is in fact concentrated toward the galactic center.

The tails on burst profiles and the likely concentration of sources towards the galactic center have led us to consider the effects of propagation through 10 kpc of dusty interstellar medium on a brief burst of x-rays. We have concluded that the very small angle scattering of x-rays by interstellar grains may easily account for the burst tails seen from many burst

sources. Conversely, we are able to derive constraints on the grain number and size distribution from the burster data. In §II we present the hypothesis and motivate the later discussion with order of magnitude estimates, X-ray scattering by grains is briefly reviewed in §III, and in §IV we carefully study the development of a pulse of radiation as it propagates through a medium containing small angle scatterers. We have considered all optical depths. Many of these results are quite general and may be useful in contexts other than x-ray scattering by grains. Our model for the development of x-ray burst profiles is confronted with the data in §V, and we discuss future prospects.

II. AN OVERVIEW

Overbeck (1965) first considered the scattering of x-ray photons by interstellar grains. He proposed the hypothesis that all of the x-rays seen from the Crab nebula originated in the pulsar, and that the diffuse, unpulsed component was a halo of scattered radiation. [However, a recent analysis by Ryter (1970) shows that the optical depth to scattering along the line of sight to the Crab is almost certainly too low, and this hypothesis should be discarded.] The scattering of x-rays by grains was discussed further by Slysh (1969) and Hayakawa (1970), who analyzed somewhat more carefully the intensity structure of an x-ray halo around a steady point-like x-ray source. Trümper and Schönfelder (1973) have considered the case of singly scattered x-rays and propose a scheme of distance determination based on observing (in a narrow energy band) the time variations of a small angular region of the halo around an intrinsically varying x-ray source. For most observable

sources this scheme demands too much from the data; we present a more powerful technique in this paper.

The x-ray burst sources are much more promising objects for an analysis of scattering effects than sources that have previously been considered, for several reasons. The first is their very brief, intense variability, so that one may estimate the efficiency of scattering precisely. Their spectra are prominent in the energy range (2-20 keV) where interstellar absorption is relatively unimportant, but where scattering may be significant. Since there exist many observations in several energy channels, it is possible to test the hypothesis that grain scattering is responsible for the tails of the bursts. Finally, since their distribution on the sky shows such a strong concentration to the galactic center, one may assume (with some confidence) that they are indeed clustered around the galactic center and are $\sim$10 kpc distant from us. This statistical estimate of the distance allows us to infer properties of the grain distribution over a large path length through the disk of our galaxy.

Before proceeding with detailed calculations, we estimate the magnitude of some of the effects of scattering of x-rays by grains. If θ is the typical scattering angle when a photon of energy ϵ scatters off a grain of radius a, then

$$\theta \sim \frac{\lambda}{2\pi a} = 7 \left(\frac{1\mu}{a}\right)\left(\frac{6\ \text{keV}}{\epsilon}\right)\ \text{arc sec}\ .$$

If there is a uniform distribution of grains along the line of sight, the typical time delay t of photons scattered once is

$$t \sim \frac{\theta^2 R}{8c} = 130 \left(\frac{1\mu}{a}\right)^2 \left(\frac{6\ \text{keV}}{\epsilon}\right)^2 \left(\frac{R}{10\ \text{kpc}}\right)\ \text{sec}$$

where R is the distance to the source and c the speed of light. This is

a considerable delay; notice that for the small ($\sim 0.1\mu$) grains generally believed to be responsible for interstellar reddening and extinction, delays $\sim 10^4$ sec are produced. Clearly the optical depth to scattering by these small grains must be very low, or the short bursts observed would not be possible. If this scattering process is responsible for the $\sim$ 10-sec tails observed in the bursters, then $\sim 3\mu$ grains must be doing the scattering. We will have to estimate the optical depth to scattering by such grains.

The total scattering cross section σ_s of a grain with radius a is

$$\sigma_s \equiv Q_s \pi a^2$$

where the scattering efficiency Q_s (discussed in §III) varies with radius in the rather complex way shown in Figure 1. It may be approximated for our purposes here (and for the typical material magnesium silicate) by

$$Q_s \simeq 0.7 \left(\frac{6 \text{ keV}}{\epsilon}\right)^2 \left(\frac{a}{1\mu}\right)^2 \qquad \text{if } Q_s < 1$$

$$Q_s \approx 2 \text{ otherwise}$$

The "break" in the shape of Q_s occurs when $a \approx 1\mu$ in the example.

There is a useful and fairly general constraint on the grain distribution, based on the total mass density of material available to make up the grains. We can write

$$\frac{4\pi}{3} a^3 n_g \rho_g < 5 \times 10^{-26} \text{ g cm}^{-3}$$

where n_g is the number density of grains in the interstellar medium, ρ_g is the grain mass density. We have assumed the canonical mean interstellar gas density, and that 3 percent of the mass is in heavy elements. It is probable

that most of the heavy elements are locked up in grains. Since the optical depth, $\tau \propto a^4 n_g$ for small grains, and $\tau \propto a^2 n_g$ for large grains, the constraints above will admit $\tau \sim 1$ only for a range of a centered around $a \sim 1\,\mu$. A careful calculation yields:

$$0.3\ \mu \lesssim a \lesssim 3\,\mu \qquad \text{for 6 keV photons and } MgSiO_3 \text{ grains.}$$

A similar calculation may be based on the visual extinction to the galactic center, which is generally taken to be 25 magnitudes (Becklin and Neugebauer 1968). Since reddening as well as extinction is observed, the grains responsible must have $a \lesssim 0.2\ \mu$. Using the argument based on mass density above, and the Rayleigh scattering cross section we find that

$$0.1\ \mu \lesssim a \lesssim 0.2\ \mu \ .$$

These two sets of limits are not (as they may appear) contradictory since they refer to two different populations of grains. We simply require that a significant fraction of the mass be in each of these two populations. These calculations have all assumed that all grains have the same radius. This is an oversimplification, but the limits above do refer to typical sizes of the grains responsible for these processes.

We note finally that, given 25 magnitudes of visual extinction to the galactic center, every photon passes through many grains. It is only because $Q_s \ll 1$ for most of the grains that the x-ray optical depths are so low.

III. THE SCATTERING OF X-RAYS BY GRAINS

We need to know the total and differential cross sections for the scattering of x-rays by grains. A brief review of the assumptions and results is presented here, and we refer to van de Hulst (1957) for a detailed discussion.

Previous authors (cited in §I) have used the "Rayleigh-Gans" approximation for spherical grains. Each volume element of the grain is polarized by and in phase with the incident wave, and so acts as a source for a scattered wave amplitude. The sum of scattered amplitudes is sharply peaked in the forward direction. (Even though the energy of the photon may greatly exceed the binding energy of the electrons in the grain, the momentum imparted to an electron in this forward scattering is too low to change its state and thus distinguish it. We could sum scattering amplitudes for all of the electrons quantum mechanically and obtain the classical result.) The validity of this approximation requires $|m - 1| \ll 1$, where m is the refractive index; and $|\rho| = (4\pi a/\lambda)|m - 1| \ll 1$ where ρ is the phase shift across the grain. The first of these assumptions holds in all situations we consider. Using $MgSiO_3$ to provide a "typical" value of m:

$$|\rho| \cong 1 \cdot 1 \left(\frac{\epsilon}{6\ \mathrm{keV}}\right)^{-1} \left(\frac{a}{1\mu}\right) \quad . \tag{1}$$

We see that the second assumption holds in the situations discussed by previous authors of x-ray scattering by the grains responsible for interstellar reddening, but is clearly invalid for the larger grains we consider here. Accordingly, we relax this condition in favor of the "anomalous diffraction" approximation where the conditions $|m - 1| \ll 1$ and $(2\pi a/\lambda) \gg 1$ are required. In this case the phase changes through the grain are evaluated

using ray optics. The Rayleigh-Gans formulae are still appropriate for limiting cases where $\rho \to 0$.

We show the "anomalous diffraction" differential cross section, $1/\sigma_T \; d\sigma/dz$ [where $z = (2\pi a/\lambda)\theta$ is the appropriately scaled angular coordinate and σ_T is the total cross section], for the typical case $|\rho| = 4$ in Figure 2. On the same figure the Rayleigh-Gans case ($\rho \to 0$) is plotted. The difference between the two curves is certainly no larger than the error made in assuming the grains are spherical. Since the Rayleigh-Gans solution is simple and analytic we will use it whenever we need an explicit form for the angular distribution. It is, in the small angle limit:

$$\frac{1}{\sigma_T} \frac{d\sigma}{dz} = \frac{4}{z} j_1^2 (z) \tag{2}$$

where j_1 is a spherical Bessel function of the first kind.

The scattering efficiency Q_s, defined in §II, is plotted against $\rho_R = \Re e\{\rho\}$ on Figure 1, for the special case of 6 keV photons and $MgSiO_3$ grains. The parameter β gives the relative importance of absorption:

$$\tan \beta = \frac{\Im m\{m\}}{\Re e\{m-1\}} = \left\{ \begin{array}{ll} 0.15 & 1 \text{ keV} \\ 0.093 & 3 \text{ keV} \\ 0.034 & 6 \text{ keV} \\ 0.020 & 9 \text{ keV} \end{array} \right\} \quad \text{at} \quad \epsilon = \; . \tag{3}$$

(Note that in all these treatments diffraction is treated as scattering so an amplitude for absorption leads to an amplitude for scattering.) On the same plot are the absorption efficiency Q_a, and the scattering efficiency Q_o for non-absorbing grains (i.e., $\beta = 0$).

There are four regions of interest. The first (not shown on Fig. 1)

occurs where $\rho_R < 8/3 \tan\beta$, so that $Q_a > Q_s$. The second, where $8/3 \tan\beta < \rho_R < 1$, is a region where $Q_s \approx Q_o$ and the Rayleigh-Gans approximation is useful. In this regime

$$Q_s \equiv 2\left(\frac{2\pi a}{\lambda}\right)^2 |m-1|^2 = \tfrac{1}{2}\rho_R^2 (1+\tan^2\beta) \ll 1 . \qquad (4)$$

When $1 < \rho_R < 0.03/\tan\beta$, Q_s departs significantly from Q_o because of the increasing importance of absorption. The Rayleigh-Gans differential cross section is useful in a general sense (see Fig. 2) but now $Q_s \sim 1$ [quite different from eq. (4)]. Finally, when $\rho_R > 0.3/\tan\beta$ we have $Q_s \to Q_a \to 1$. For $MgSiO_3$ grains this corresponds to

$$\left(\frac{a}{3\mu}\right)\left(\frac{\epsilon}{3\ \text{keV}}\right)^{-2.4} \gtrsim 0.5 .$$

In this regime it is unlikely that one can consider multiple scattering because absorption is so important.

IV. THE SMEARING OF TEMPORAL AND SPATIAL STRUCTURE BY SMALL ANGLE SCATTERING

We derive here some formulae that show how the temporal and spatial structure of a source of radiation is smeared by small angle scattering of the photons as they propagate to the observer. These formulae are all developed under the assumption that the resultant angle of the photon trajectory after any number of scatterings is small. This requirement keeps the analysis in a quantitatively different regime from that of random walk analyses, and the results are qualitatively different. In subsection (a) we derive some exact formulae for the second and fourth moments of the distribution of

arrival angles of the photons and the first moment of the distribution of their delays. These formulae provide a powerful tool for analysis of observational data. In (b) a general equation describing the evolution of a burst of radiation is derived. Approximate solutions valid at low and high optical depths are developed in (c) and (d) respectively, and compared in (e). These analyses are specialized to the case in which the source of radiation is point-like in space and time, and the scatterers are uniformly and randomly distributed in space. In (f) we give simple relationships between this special case and some more general cases. In (g) we show how to use the results to analyze observational data.

We will use the symbol $P(\alpha,\beta,\ldots;A)$ for any probability density function, where the $\alpha,\beta,\ldots$ represent the random variables, and A represents some parameter. The precise meaning of all the variables will be obvious in context.

a) Moments of the Photon Distribution

We use Θ to denote a scattering angle, φ to denote the angle a photon trajectory makes to a radius vector, t to denote delay (with respect to an unscattered photon) and R to denote the distance between source and observer. In Figure 3 we have schematically shown the progress of a photon that scatters several times. We have oriented axes so that the photon starts out along the z-axis. Suppose there are n scattering events between the origin and radius R. The expected value of φ_n^2 at R is given by

$$\langle \varphi_n^2 \rangle = \left\langle \left(\sum_{i=1}^{n} \Theta_i \cos \xi_i - \frac{1}{R} \sum_{i=1}^{n} \ell_i \sum_{j \le i} \Theta_j \cos \xi_j \right)^2 + \left(\sum_{i=1}^{n} \Theta_i \sin \xi_i - \frac{1}{R} \sum_{i=1}^{n} \ell_i \sum_{j \le i} \Theta_j \sin \xi_j \right)^2 \right\rangle \tag{5}$$

where ξ_j is the azimuthal angle of the jth scattering; all other new quantities are defined in the figure caption. If we expand the squares in equation (5) the expression may be simplified rapidly. The ξ_i are uniformly distributed independent random variables, so terms like $\langle \cos \xi_i \rangle$ vanish. The θ_i are independent random variables drawn from a distribution with second moment $\langle \theta^2 \rangle$. If we express the ℓ_i in terms of their partial sums $s_i = \sum_{j=0}^{i-1} \ell_j$ and note that the $\{s_i\}$ are an ordered sample of n numbers drawn randomly from the interval (0,R) we can show that

$$\langle \varphi_n^2 \rangle = \frac{n}{3} \langle \theta^2 \rangle \quad . \tag{6a}$$

The number of scatterings is a Poisson random variable with mean τ, so the expected value $\langle \varphi^2 \rangle$ averaged over n is:

$$\langle \varphi^2 \rangle = \frac{\tau}{3} \langle \theta^2 \rangle \quad . \tag{6b}$$

The central assumption in all of §IV is that $\langle \varphi^2 \rangle \ll 1$. A similar, but much more tedious calculation yields

$$\langle \varphi^4 \rangle = \frac{2\tau^2}{9} \left(\langle \theta^2 \rangle^2 + \frac{9}{10} \frac{\langle \theta^4 \rangle}{\tau} \right) . \tag{7}$$

This expression shows that for large τ only $\langle \theta^2 \rangle$ is needed to determine $\langle \varphi^4 \rangle$. This is true for all the higher moments of φ, and we see that for large τ the distribution function of φ is determined entirely by the quantity $\tau \langle \theta^2 \rangle$.

We use an alternative procedure, analogous to that used in the analysis of Brownian motion, to find the mean time delay. We consider a photon initially traveling along the z-axis, scattering through a small angle θ. It is clear that

$$|\Delta \underset{\sim}{v}| = c\theta; \quad \langle \Delta v_x \rangle = \langle \Delta v_y \rangle = 0; \quad \langle \Delta v_z \rangle \cong - \tfrac{1}{2} c \langle \theta^2 \rangle .$$

We can use this to represent the evolution of the photon velocity with time T:

$$\frac{d}{dT}\,\underset{\sim}{v} = -\,\tfrac{1}{2}\,c\kappa\langle\theta^2\rangle\,\underset{\sim}{v} + \underset{\sim}{F}(T) \tag{8}$$

where κ is the scattering coefficient and $\underset{\sim}{F}$ is a fluctuating quantity with mean zero. By taking the dot product of equation (8) with $\underset{\sim}{r}$ (the position vector at time T), taking an ensemble average and noting that $\underset{\sim}{v}\cdot\underset{\sim}{v} = c^2$ we obtain the simple equation

$$\frac{d^2}{dT^2}\langle r^2\rangle + \tfrac{1}{2}\,c\kappa\langle\theta^2\rangle\,\frac{d}{dT}\langle r^2\rangle = 2c^2 \quad .$$

Solving this equation and keeping only terms to first order in small quantities:

$$\langle r^2\rangle = R^2\left(1 - \frac{\tau\langle\theta^2\rangle}{6}\right)$$

where we have picked out the time at which $cT = R$. However, we really want $c\langle t\rangle = R - \langle r\rangle$, but the difference between $\langle r\rangle$ and $\langle r^2\rangle^{\frac{1}{2}}$ is second order in $\tau\langle\theta^2\rangle$, i.e. $\langle r^2\rangle - \langle r\rangle^2 \simeq \langle(\text{pulse width})^2\rangle$, so we may write:

$$\langle t\rangle = \frac{1}{12}\,\frac{\tau R}{c}\,\langle\theta^2\rangle \quad . \tag{9}$$

b) The Evolution of a Point-Like Burst of Radiation

In what follows it is convenient to use $\zeta \equiv \varphi^2$, $\gamma \equiv \kappa ct$ and τ as our independent variables. We define the probability density function for the distribution of photons at optical depth τ by:

$P(\zeta,\gamma;\tau)d\zeta d\gamma \equiv$ probability that a given photon has $\zeta < \varphi^2 < \zeta + d\zeta$,

and $\gamma < \kappa ct < \gamma + d\gamma$ at optical depth τ (10a)

with normalization

$$\int_0^\infty d\zeta \int_0^\infty d\gamma \; P(\zeta,\gamma;\tau) \;=\; 1 \qquad (10b)$$

and initial condition

$$P(\zeta,\gamma;\; \tau = 0) \;=\; \delta(\zeta)\; \delta(\gamma) \qquad (10c)$$

Consider the evolution of P from τ to $\tau + d\tau$ in the absence of scattering. We follow the particular trajectory shown in Figure 4. We can see immediately from the law of sines that:

$$d\zeta \;=\; -\frac{2\zeta d\tau}{\tau}$$

The increment in time delay is

$$d\gamma \;=\; PQ - d\tau = \tfrac{1}{2}\,\zeta\, d\tau$$

where we used the law of cosines and kept only terms of lowest order in $d\tau$. Keeping in mind the conservation condition in equation (10b) we can write:

$$P\left(\zeta - \frac{2\zeta d\tau}{\tau}\;,\;\; \gamma + \frac{1}{2}\,\zeta d\tau \;;\; \tau + d\tau\right)\left(1 - \frac{2d\tau}{\tau}\right) \;=\; P(\zeta,\, \gamma;\, \tau) \qquad (11a)$$

from which

$$\frac{\partial P}{\partial \tau} \;=\; \frac{2}{\tau}\,P - \frac{1}{2}\,\zeta\,\frac{\partial P}{\partial \gamma} + \frac{2\zeta}{\tau}\,\frac{\partial P}{\partial \zeta} \qquad (11b)$$

The evolution of P due to scattering is just the familiar radiative transfer equation in a scattering medium:

$$\frac{\partial P}{\partial \tau} = -P + \int_0^\infty P(\zeta', \gamma; \tau)\, S(\zeta,\zeta')\, d\zeta' \qquad (12a)$$

with

$S(\zeta,\zeta')d\zeta' \equiv$ Probability that a scattered photon shifts from $\zeta = \varphi^2$ to $\zeta' < \varphi^2 < \zeta' + d\zeta'$ (12b)

Putting the pieces from equations (11b) and (12a) together we obtain the equation that describes the evolution of P:

$$\frac{\partial P}{\partial \tau} = \left(\frac{2}{\tau} - 1\right)P - \frac{1}{2}\zeta\frac{\partial P}{\partial \gamma} + \frac{2\zeta}{\tau}\frac{\partial P}{\partial \zeta} + \int_0^\infty P(\zeta', \gamma; \tau)\, S(\zeta,\zeta')\, d\zeta' \qquad (13)$$

We need to evaluate the function S in terms of the differential cross section evaluated in §III. This is given by the integral:

$$S(\zeta,\zeta') = \frac{1}{\pi\sigma_T}\int_0^{2\pi} \frac{d\sigma}{d\theta}\left(\theta = \left[\zeta' + \zeta - 2\sqrt{\zeta\,\zeta'}\cos p\right]^{1/2}\right)\zeta'\, dp \qquad (14)$$

Equations (13) and (14) together with the initial condition in equation (10c) provide a prescription that completely describes the evolution of a pulse of radiation. In the general case, these equations may only be solved numerically. In the next two sections we study the limits of low and high optical depth analytically.

The observable quantity is $I(\varphi,t)$, the specific intensity (with units photons cm^{-2} s^{-1} $ster^{-1}$). If the pulse consists of N photons then:

$$I(\varphi,t) = \frac{N\kappa c}{4\pi^2 R^2}\, P(\varphi^2, \kappa ct;\tau) \qquad (15)$$

c) The Limit $\tau \to 0$

We can derive a simple analytic expression for the distribution in time delay and angle for those photons that have only scattered once. It will be

convenient here to use φ and $\Gamma = 2ct/R = 2\tau\gamma$ as our independent variables. If we denote this distribution by $P_1(\varphi,\Gamma)$ then as $\tau \to 0$, we have to high accuracy:

$$P(\varphi,\Gamma;\ \tau) = (1 - \tau)\ \delta(\varphi)\ \delta(\Gamma) + \tau P_1(\varphi,\Gamma) \tag{16}$$

The locus of scattering sites giving a fixed time delay is an ellipsoid of revolution (Fig. 5) with foci at the source and observer. This geometrical construction was used by Trümper and Schönfelder (1973); we present here a more complete computation. The problem was also discussed by Morrison and Sartori (1969) in connection with supernova light curves, and their results were applied to x-ray bursters by Grindlay and Gursky (1976b) and Canizares (1976). These latter authors considered large angle scattering in the vicinity of the source, where the surface is nearly a paraboloid. We consider here small angle scattering all along the line of sight; our geometry is almost cylindrical.

The distribution of scattering angles is just $\frac{1}{\sigma_T}\ \frac{d\sigma}{d\theta}$, and α (defined in Fig. 5) is uniformly distributed between 0 and 1. Using the geometric relationships between θ,α and φ,Γ we find (cf. Trümper and Schönfelder 1973)

$$P_1(\varphi,\Gamma) = \frac{1}{\Gamma + \varphi^2}\ \frac{1}{\sigma_T}\ \frac{d\sigma}{d\theta}\left(\theta = \varphi + \frac{\Gamma}{\varphi}\right) \tag{17}$$

We now compute a particular example of P_1, for the case where all of the scatterers are spheres of radius a, and the scattering function is that for the Rayleigh-Gans case discussed in §III. In view of the convenient scaling properties with a and λ we introduce scaled variables.

$$\eta \equiv \left(\frac{2\pi a}{\lambda}\right)^2 \Gamma \qquad \text{and} \qquad \chi \equiv \left(\frac{2\pi a}{\lambda}\right) \varphi$$

The quantity evaluated will actually be $P(\chi^2,\eta)$ because, as we showed in equation (15), this is proportional to the specific intensity. The result is

$$P_1(\chi^2,\eta) = 2\left[\frac{j_1(\chi + \eta/\chi)}{\chi^2 + \eta}\right]^2 \tag{18}$$

This function is plotted in Figure 6, where the relationship with intensity is explicitly given. The singularity about the origin is, of course, integrable. We discuss this figure more carefully in (e).

We can find from equation (18) the distributions in χ^2 and η separately. The former is:

$$P_1(\chi^2) = \frac{2}{\chi}\int_{\chi}^{\infty}\left[\frac{j_1(y)}{y}\right]^2 dy \tag{19}$$

$P_1(\chi^2)$ is proportional to the time integrated specific intensity in the burst, and is plotted against χ in Figure 7.

The integral over χ^2 is not so easy to simplify, but a form convenient for computation is:

$$P_1(\eta) = 8\int_{\sqrt{\eta}}^{\infty}\left[\frac{j_1(\chi + \eta/\chi)}{\chi^2 + \eta}\right]^2 \chi d\chi \tag{20}$$

This quantity is plotted in Figure 8.

d) The Limit $\tau \to \infty$

In this limit every photon has undergone many scatterings, and consequently the width of P in ζ is large compared to the width of $S(\zeta,\zeta')$ in $\zeta - \zeta'$. This permits us to expand the integrand in equation (13) in a Taylor series about ζ. Keeping only terms of comparable order yields zeroth, first and second derivatives of P with respect to ζ. The coefficients are easy to

evaluate in terms of ζ and $\langle\theta^2\rangle$. The resulting equation is

$$\frac{\partial P}{\partial \tau} = \frac{2}{\tau} P - \frac{1}{2} \zeta \frac{\partial P}{\partial \gamma} + \left(\langle\theta^2\rangle + \frac{2\zeta}{\tau}\right) \frac{\partial P}{\partial \zeta} + \zeta \langle\theta^2\rangle \frac{\partial^2 P}{\partial \zeta^2} \tag{21}$$

The solution of (21) is involved and has been left, for the interested reader, to an Appendix. The result is:

$$P(\zeta,\gamma;\tau) = \frac{1}{\langle\theta^2\rangle^2 \tau^3} G\left(\frac{\zeta}{\tau\langle\theta^2\rangle}, \frac{\gamma}{\tau^2\langle\theta^2\rangle}\right) \tag{22}$$

where $G(x,y)$ is given by an integral expression derived in the Appendix. This expression for G may be easily computed numerically. We have plotted $G(x,y)$ in Figure 9. This expression completely describes the asymptotic behavior of a burst as $\tau \to \infty$. We discuss the shape of G, and compare it with the similar function derived for the limit $\tau \to 0$, in (f).

If we integrate equation (22) over γ we obtain a particularly simple expression:

$$P(\zeta;\tau) = \frac{3}{\tau\langle\theta^2\rangle} \exp\left\{-\frac{3\zeta}{\tau\langle\theta^2\rangle}\right\} \tag{23}$$

i.e., the brightness of the halo, integrated over the pulse, is a Gaussian in φ. The integral of equation (22) over ζ gives the distribution in the time delay γ:

$$P(\gamma;\tau) = \frac{4\pi^2}{\tau^2\langle\theta^2\rangle} \sum_{n=1}^{\infty} (-1)^{n+1} n^2 \exp\left\{\frac{-2n^2\pi^2\gamma}{\tau^2\langle\theta^2\rangle}\right\} \tag{24}$$

This function is plotted in Figure 10, which shows the sharp rise followed by an exponential decline. A similar result derived quite differently by Williamson (1972) in the context of radio Pulsar pulse broadening. It is clear from the series above that once $\gamma/\tau^2\langle\theta^2\rangle \gtrsim 1$, only the leading term in the series is important — this leading term is dashed in Figure 10 to show how rapidly this asymptote is approached.

e) Some Comments on the Distribution Functions

It is clear that our solution for $P(\zeta,\gamma;\tau)$ in the low τ limit is the appropriate case for the x-ray scattering problem, however the other limit is intrinsically interesting and may have greater utility in other circumstances. The differences between the two are strikingly illustrated by the differences between Figure 6 and Figure 9, which give the joint probability density functions in φ^2 and t for the two limits, with appropriate scaling of coordinates. Recall that Figure 6 is just the distribution for singly scattered photons, and the full distribution includes a δ-function in φ^2 and t at the origin, for the unscattered photons. For the singly scattered distribution there are many photons with small time delay, whereas with $\tau \to \infty$ there are almost no photons at low time delays (cf. also Figs. 8 and 10). The singly scattered photons are unlikely to have very low φ^2, since there is very little solid angle for scattering directly forward. Contrast $\tau \to \infty$, where these effects wash out and there is a concentration of the halo towards the center, except for the large time delays. [The integrable singularity in the singly scattered distribution is a general property of eq. (17) and hence will occur in any scattering situation.] The distribution for $\tau \to \infty$ is smooth and independent of the shape of the scattering function; this property was indicated in the comment following equation (7).

The tails of the x-ray bursts are well fit by exponentials. The singly scattered time delay distribution [eq. (20)] is represented very precisely by the analytic fit

$$P_1(\eta) = 1.2\ e^{-1.4\eta} + 0.9\ e^{-9.5\eta} \qquad (25)$$

which also represents the data very well.

We have extensively checked all our analyses with Monte-Carlo computations, which confirm all of the above statements. In fact the distribution $P(\eta)$ given by equation (20) gives a reasonable representation of the results even when $\tau = 1$, and 26 percent of the photons have scattered more than once. The effect of multiple scattering is to reduce the slope of the decaying exponential. It is interesting to see how rapidly the asymptotic distribution is approached as τ increases. By $\tau \sim 5$ the general shape is clear, but the depth and width of the valley at small time delay is not reached until $\tau \gtrsim 20$. The individual distribution $P(\zeta;\tau)$ approaches the asymptotic form to within a few percent by $\tau \sim 10$, but $P(\gamma;\tau)$ does not reach its asymptotic form until $\tau > 20$ because the number of photons with small time delays decays slowly. Beyond this valley, however, the asymptotic form is an excellent approximation for $\tau \gtrsim 10$.

f) Extending the Results

Equation (10) describes an instantaneous pulse of radiation. If the pulse at the source has a normalized profile $\mathcal{L}(t)$ then:

$$P_{\mathcal{L}}(\zeta,\gamma;\tau) = \int_0^{\gamma} \mathcal{L}\left(\frac{\gamma'}{\mu c}\right) P(\zeta,\gamma - \gamma';\tau)d\gamma' \qquad (26)$$

where $P_{\mathcal{L}}$ is the observed distribution function and P is the distribution function defined in equation (10). A similar convolution integral shows the smearing of angular structure due to scattering.

It is more interesting to consider the possibility that the scatterers are not uniformly distributed along the line of sight. We mentioned earlier the work of Morrison and Sartori on a small scattering region around the

source. In a more general case, suppose the source of radiation is surrounded by spherical cloud of scatterers, of radius R_* and optical depth τ_*. The distribution of angles and time delays at the surface of the cloud, $P(\zeta,ct;R_*)$ say, is given by the analysis above. Suppose the observer is at a distance $R > R_*$ from the source, and that no scattering occurs between the cloud and the observer. Then we geometrically compute the distribution seen by the observer:

$$P(\zeta,ct;R) = \left(\frac{R}{R_*}\right)^2 P\left(\frac{\zeta R^2}{R_*^2}, ct - \frac{1}{6}\left(\frac{R - R_*}{R_*}\right) R\zeta;R_*\right) \tag{27}$$

We note that this is the general solution of equation (11b) for $R > R_*$ with an initial condition at R_*, if we replace τ by R and γ by ct in the differential equation. In this situation we may also calculate moments as in (b), with the small modifications

$$\begin{aligned} \langle\varphi^2\rangle &= \frac{\tau_*}{3}\left(\frac{R_*}{R}\right)^2 \langle\theta^2\rangle \\ \langle t\rangle &= \tau_* \frac{R_*}{c}\langle\theta^2\rangle\left\{\frac{1}{12} + \frac{1}{18}\left(\frac{R - R_*}{R}\right)\right\} \end{aligned} \tag{28}$$

Similar relationships between the distribution function defined in equations (10) and those appropriate to other distributions of scatterers exist. Fundamental to all of these analyses is the solution of equation (13).

Another case that may be considered occurs when there are very few scatterers, each of significant cross section. This description would be appropriate in the x-ray burster problem if all of the dust in the galactic plane were concentrated into a few dense clouds, each of which could then be regarded as a single scatterer. The scattering of photons traversing the universe by a cosmological density of collapsed objects (cf. Press and Gunn 1973) is a further example. We will not analyze either of these cases here.

g) Analysis of Data

The results derived above have some general features that can be particularly useful in the analysis of data. We consider first the moment equations. These may be very useful tools for studying the x-ray bursters as measurements with better angular resolution become available. Once the halos are resolved, the two moments $\langle\varphi^2\rangle$ and $\langle\varphi^4\rangle$ can be estimated (note that all of these moments include the unscattered component.) Under the (surely reasonable) assumption that the bursting object is point-like, the optical depth may be estimated from the ratio of the integrated energy in the halo to the total energy. Using these three numbers and equations (6b) and (7) we can estimate $\langle\theta^2\rangle$ and $\langle\theta^4\rangle$ for the scatterers, which give useful information about the grain distribution. Accurately estimating the mean time delay for the burster sources will not be easy, because it seems that the original burst has a width of a few seconds. However, an estimate will be possible, and we can use equations (6b) and (9) to obtain

$$R = \frac{c\langle t\rangle}{4\langle\varphi^2\rangle} \quad , \tag{29}$$

a purely geometrical distance to the source! With simultaneous data in many narrow energy bands we could better determine R by estimating $\langle t\rangle$ and $\langle\varphi^2\rangle$ in each band. A graph of $\langle t\rangle$ versus $\langle\varphi^2\rangle$ should be a straight line with slope $4R/c$. Obviously this estimate depends on the assumption that the dust is rather uniformly distributed in the disk.

This procedure is superior to that of Trümper and Schönfelder in several ways. First, it depends only on simple moments of observable quantities, rather than dubious model fitting. It is independent of any property of the scatterers, whereas their formulae explicitly include their maximum scattering

angle. Finally, our procedure is valid at any optical depth, whereas they have considered only singly scattered photons and consequently can be accurate only at very small optical depths.

V. COMPARISON WITH OBSERVATIONS

We discuss here the x-ray burst profiles in terms of our analysis. Only time data are available, and the shapes of the bursts indicate that the dust is optically thin to scattering. A general estimate of the power in the tails yields $\tau \approx 0.5$, so that the small τ limit is appropriate.

a) The Exponential Tails

There are a number of tests of the hypothesis that grains are responsible for the tails in the x-ray bursts. Since the mean time delay is proportional to ϵ^{-2} (where ϵ is the photon energy) the tails should be longer in the lower energy channels (i.e., the spectrum should soften in the tails). The number of $\sim 3\mu$ grains invoked must not violate any upper limits obtained in other spectral ranges. In any narrow energy channel the shape of the tail should be constant from burst to burst, and there should not be any structure in the tails that cannot be modeled by the convolution integral in equation (25). The restriction to narrow energy channels will eliminate confusion that occurs when the intrinsic spectra of the bursts vary.

Some of these criteria seem to be violated by the observations of some sources. The globular cluster source, 3U1820-30, exhibits spectral hardening in the tails. The tails have been observed to vary and in one observation almost disappeared. However, the globular cluster NGC6624 is not highly reddened (and probably not 10 kpc distant either: Liller and Liller (1976) give $E_{B-V} = 0.40$ and $R = 5.0 \pm 1.0$ kpc). It is true that the large grains we invoke would not contribute to the reddening, but a reasonable assumption is that

their distribution follows that of the small grains. We conclude that there are too few 3μ grains obscuring NGC6624 to produce any observable effect, and that the tails are not produced by grain scattering. There are two other instances in which the burst spectra are reported to harden. One of these is KGX 345-6 (Babushkina et al. 1975 ; Sagddeev 1976). The measurements here are at such high energy (40-200 keV) that is is not even clear that the objects belong to the same class. At these energies the scattering process will not produce an observable tail so we do not discuss their data. Grindlay and Gursky (1976a) reported that XB1608-52 showed spectral hardening during two bursts observed in earlier Uhuru data. They observed ~ 10 sec fragments of these bursts containing sharp rises but no clear decline [a lower limit to the decay timescale is 30 sec; Belian et al. (1976) had estimated upper limits of ~ 130 sec]. During these fragments the spectra hardened. However, two other events for which the rise occurred before the source entered the field of view had much softer spectra, suggesting that this object exhibits the 'standard' behavior but with a longer time constant. In view of the inconclusive state of the data we do not consider this source a counter-example to our model.

However, it is the property of most bursters that the spectra soften during the tail (Lewin 1977). In fact, the bursts for most objects show very accurately the time structure we would expect from this process, given an intrinsic burst having a sharp rise and width of a few seconds. The fraction of the power received in the tail is also a decreasing function of energy, as we would expect. A well observed, archetypal source is MXB 1728-34 (Hoffman et al. 1976, 1977). In the former paper their Figure 2 clearly shows how the time constant of the decay falls with increasing energy. This behavior is clear in Figure 3 of their second paper, where the decreasing fraction

of power in the tails with increasing energy is also evident. Data in narrower energy channels would test the ϵ^{-2} prediction quantitatively.

We conclude that the short tails observed in most of the burster sources could indeed be the result of scattering along the line of sight by 3μ grains. The anomalous behavior of 3U1820-30 does not contradict our model, and the evidence for anomalous behavior in KGX345-6 and XB1608-52 is not sufficiently convincing to discount this model for the other sources. Unless grain scattering can be discounted, astrophysical models that produce a softening tail in the vicinity of the source are unnecessary.

b) The Enhanced Post-Burst Emission from MXB1728-34

Hoffman et al. (1977) report an "enhanced emission" from MXB1728-34 following seven relatively hard bursts. They present a composite time series that exhibits all of the properties we ascribed above to dust scattering, but with a longer timescale and smaller amplitude. The enhanced emission is evident up to $\geq$ 150 seconds following the burst at 1.2-3 keV, up to $\sim$ 120 seconds at 3-6 keV, and $\sim$ 30 seconds at 6-12 keV and vanishes in the higher channels. The fraction of the pulse in these decays is $\sim$ 34% at 1.2-3 keV, $\sim$ 15% at 3-6 keV and down to $\sim$ 3% at 6-12 keV (Hoffman et al. 1977, Table 2). These observations are entirely consistent with scattering of a small fraction of the x-rays by 1μ grains.

There is one possible difficulty, however. Hoffman et al. (1977) state that four earlier bursts from MXB1728-34 do not show this enhancement after the bursts. If this is correct (i.e., there are sufficient counting statistics to discover this weak enhancement) then the post-burst enhancement is probably intrinsic to the source. The authors also note that Lewin et al. (1976) observed no post-burst enhancement in MXB1906+00, but the counting statistics in the latter measurement are not sufficient to rule out an enhancement

similar to that of MXB1728-34. A careful survey of all the bursters for this phenomenon could settle the question unambiguously: if 1μ grains are responsible for the post-burst enhancement in MXB1728-34, then similar behavior should be found in most of the other sources.

c) The Interstellar Grains

We saw in §II that we could have $\tau \geq 1$ when $0.3\mu \leq a \leq 3\mu$ without violating upper limits given by the density of matter. We now investigate whether or not these large grains produce observable effects in another spectral range. We will use MXB1728-34 as an archetype for this comparison. It is evident that in the energy range 3-6 keV about half the total power is in the tail; this implies $\tau \approx 0.5$. We are considering a distribution of grain sizes whose x-ray scattering optical depth peaks at 3μ (and perhaps also at 1μ). The only other measurements sensitive to this population of grains are infrared observations of the galactic center.

These grains have an extinction efficiency $Q_e \approx 2$ for most infrared wavelengths at which measurements are made. Consequently they contribute a "grey" opacity that produces no reddening of radiation. This "grey" extinction is obtained by subtracting selective extinction (from a measurement of reddening) from total extinction (which must be obtained indirectly). Neugebauer et al. (1977) estimate the total extinction to the galactic center, at 2.2μ, by observing the Brackett γ recombination line, whose intensity can (in principle) be predicted from a 5GHz measurement of the free-free emission from an HII region. They assume a temperature of 10^4°K for the HII region and that all of the 5GHz continuum arises there. They estimate $3^m.3$ of total extinction. They fit a reddening curve to their measurements in several colors and obtain $2^m.7$ of selective extinction. This indicates a "grey" extinction of $\sim 0^m.6$, but in fact the data are consistent with anything between 0^m and $\geq 1^m$ of grey

extinction. This is the best estimate of the extinction due to large grains, and is entirely consistent with the hypothesis that the tails of the x-ray bursts are due to scattering.

Our analysis can place more reliable limits on the grain distribution. From the observation that only $\sim 1/2$ of the photons in a given burst (between 3-6 keV) are in the tail, we argue that the total "grey" extinction to the objects due to 3μ grains is $\leq 0^m.5$. Should further observations invalidate the hypothesis, this upper limit will be lowered. Using the data discussed in (b) we find that the "grey" extinction due to 1μ grains $\leq 0^m.7$.

We note in passing that there is indirect evidence for unusually large grains in front of stars on the periphery of large dense clouds (Breger 1977 and references therein).

Several predictions of our proposed model can be tested with instrumentation on the latest generation of x-ray astronomy satellites. With its large collecting area, high energy resolution, and pointing capability HEAO-A can test the predicted ϵ^{-2} dependence of tail e-folding times. The high resolution imager on board HEAO-B (to be launched in late 1978) will be capable of detecting the predicted brightness distribution in halos around x-ray sources in the energy band $0.2 \lesssim \epsilon \lesssim 2$ keV; the search for such halos is one of the mission objectives. If and when such observations are made, the analysis presented in this paper should yield more than confirmation or denial of a grain scattering model for x-ray burst tails: It should yield much useful new information about the size and space distribution of interstellar grains.

We thank Peter Goldreich, Scott Tremaine, Gordon Garmire, Michael Jura, and Walter Lewin for helpful comments and (or) encouragement.

APPENDIX

We start with equation (21) and immediately introduce a change of variables:

$$\left.\begin{aligned} x &= \frac{\zeta}{\tau\langle\theta^2\rangle} \\ y &= \frac{\gamma}{\tau^2\langle\theta^2\rangle} \\ \tau &= \tau \end{aligned}\right\} \qquad \text{(A1)}$$

The equation becomes:

$$\tau \frac{\partial P}{\partial \tau} - 2P = (2y - \frac{x}{2}) \frac{\partial P}{\partial y} + (1 + 3x) \frac{\partial P}{\partial x} + x \frac{\partial^2 P}{\partial x^2} \qquad \text{(A2)}$$

We can separate variables:

$$P(x,y;\tau) = T(\tau)\, G(x,y) \qquad \text{(A3)}$$

and obtain the two equations

$$T = \tau^{2+k} \qquad \text{(A4a)}$$

and

$$x \frac{\partial^2 G}{\partial x^2} + (1 + 3x) \frac{\partial G}{\partial x} + (2y - \frac{1}{2} x) \frac{\partial G}{\partial y} - kG = 0 \qquad \text{(A4b)}$$

where k is the separation constant. We recall that P must satisfy the normalization condition given by equation (10b). It is clear that the form in equation (A3) can only satisfy this condition, given the solution (A4a), if

$$k = -5 \qquad \text{(A5)}$$

So we are left with the parabolic partial differential equation

$$x \frac{\partial^2 G}{\partial x^2} + (1 + 3x) \frac{\partial G}{\partial x} + (2y - \frac{1}{2} x) \frac{\partial G}{\partial y} + 5G = 0 \qquad \text{(A6)}$$

This equation is second order in x, but we do not have two boundary conditions in x. However, the regular singular point at the origin tells us that one of the two independent families of solutions (given an initial condition in y) will be irregular in x at the origin, and may be discarded. The normalization condition uniquely fixes the arbitrary multiplicative constant in G. We know that $G(x,y = 0) = 0$ since if there is no delay, then a photon can have no finite value of x.

Before proceeding to the general solution, if we integrate (A6) over y we obtain:

$$x \frac{d^2 G}{dx^2} + (1 + 3x) \frac{dG}{dx} + 3G = 0 \qquad \text{(A7)}$$

where we shall understand that G(x) is the integral of G(x,y) over all y, and similarly for G(y). The regular solution of (A7), appropriately normalized, is:

$$G(x) = 3 e^{-3x} \qquad \text{(A8)}$$

We proceed to solve (A6) for $x \geq 0$, $y \geq 0$ by extending the domain to include the entire xy plane, and then defining $G(x,y) = 0$ if either $x < 0$ or $y \leq 0$. This device enables us to use a double Fourier transform, whose utility becomes obvious later:

$$\mathcal{G}(s,t) = \int_{-\infty}^{\infty} e^{-isx} dx \int_{-\infty}^{\infty} e^{-ity} dy \, G(x,y) \qquad \text{(A9)}$$

Transforming (A6) yields:

$$(-is^2 - 3s + \frac{1}{2}t)\frac{\partial \tilde{G}}{\partial s} - 2t\frac{\partial \tilde{G}}{\partial t} - is\tilde{G} = 0 \quad . \tag{A10}$$

We seek the characteristic surfaces of (A10):

$$\frac{ds}{-is^2 - 3s + \frac{1}{2}t} = \frac{dt}{-2t} = \frac{d\tilde{G}}{is\tilde{G}} \tag{A11}$$

for which the general solution is:

$$\tilde{G}(s,t) = \mathscr{F}\left(\frac{i\sqrt{t}\, j_0 - sj_1}{i\sqrt{t}\, y_o - sy_1}\right) \frac{\sqrt{t}}{i\sqrt{t}\, j_o - sj_1} \tag{A12}$$

where $\mathscr{F}$ is an arbitrary function and the j's and y's are spherical Bessel and Neumann functions with argument $\frac{1}{2}\sqrt{t}$.

We have to pick out the particular function $\mathscr{F}$ which satisfies our requirements. This turns out to be straightforward. We perform both Fourier inversions and then integrate over y. For the correct choice of $\mathscr{F}$ this should yield (A8). If we integrate over y first a δ-function in t is obtained, so that the t inversion is then trivial. By identifying the remaining integrand with the Fourier transform of (A8) we find that $\mathscr{F}$ is a constant:

$$\mathscr{F} = -i \quad . \tag{A13}$$

Some further manipulation yields the integral expression for G:

$$G(x,y) = \frac{2i}{\pi}\int_C dp\, \frac{p^2}{j_1(p)} \exp\left\{-2p^2 y - xp\frac{j_0(p)}{j_1(p)}\right\} \tag{A14}$$

where the countour C approaches the origin in a straight line from $(1+i)\infty$, and then goes out to $(1-i)\infty$ in a straight line. The integral in (A14) is

easily evaluated numerically, and this is the expression plotted in Figure 9.

Finally we compute the integral (A14) over x. The x integral is trivial, so that:

$$G(y) = \frac{2i}{\pi} \int_C dp \ \frac{p}{j_o(p)} \ e^{-2p^2 y} \qquad \text{(A15)}$$

The contour may be closed and then (A15) evaluated by summing the residues at the poles. The result is:

$$G(y) = 4\pi^2 \sum_{n=1}^{\infty} (-1)^{n+1} \ n^2 \ e^{-2n^2\pi^2 y} \qquad \text{(A16)}$$

This is plotted in Figure 10.

REFERENCES

Babushkina, O. P., Bratolyubova-Tsulukidze, L. S., Kudryavtsev, M. I., Melioranski, A. S.. Savenko, I. A., and Yushkov, B. Yu. 1975, Soviet Astron. Lett., 1, 32.

Becklin, E. E., and Neugebauer, G. 1968, Ap. J., 151, 145.

Belian, R. D., Conner, J. P., and Evans, W. D. 1976, Ap. J. (Letters), 206, L135.

Breger, M. 1977, Ap. J., 215, 119.

Canizares, C. R. 1976, Ap. J. (Letters), 207, L101.

Clark, G. W. 1976, I.A.U. Meeting, August 1976, Grenoble, France.

Grindlay, J., and Gursky, H. 1976a, Ap. J. (Letters), 205, L131.

_____ 1976b, Ap. J. (Letters), 209, L61.

Grindlay, J., Gursky, H., Schnopper, H., Parsignault, D. R., Heise, J., Brinkman, A. C., and Schrijver, J. 1976, Ap. J. (Letters), 205, L127.

Hayakawa, S. 1970, Prog. Theor. Phys., 43, 1224.

Hoffman, J. A., Lewin, W. H. G., and Doty, J. 1977, M.N.R.A.S., 179, 57P.

Hoffman, J. A., Lewin, W. H. G., Doty, J., Hearn, D. R., Clark, G. W., Jernigan, G., and Li, F. K. 1976, Ap. J. (Letters), 210, L13.

Lewin, W. H. G. 1977, M.N.R.A.S., 170, 43.

Lewin, W. H. G., Li, F. K., Hoffman, J. A., Doty, J., Buff, J., Clark, G. W., and Rappaport, S. 1976, M.N.R.A.S., 177, 93P.

Liller, M. H., and Liller, W. 1976, Ap. J. (Letters), 207, L109.

Morrison, P., and Sartori, L. 1969, Ap. J., 158, 541.

Neugebauer, G., Becklin, E. E., Matthews, K., and Wynn-Williams, C. G. 1977, submitted to Ap. J.

Overbeck, J. W. 1965, Ap. J., 141, 864.

Press, W. H., and Gunn, J. E. 1973, Ap. J., 185, 397.

Ryter, C. 1970, Nature, 226, 1040.

Sagdeev, R. Z. 1976, I.A.U. Circ. 2959.

Slysh, V. I. 1969, Nature, 224, 159.

Trümper, J., and Shönfelder, V. 1973, Astr. and Ap., 25, 445.

Van de Hulst, H. C. 1957, Light Scattering by Small Particles (New York: Wiley).

Williamson, I. P. 1972, M.N.R.A.S., 157, 55.

FIGURE CAPTIONS

Fig. 1. The efficiency factor for both scattering and absorption is plotted versus the real part of the phase shift of a ray across a grain diameter. Q_o is a scattering efficiency if there is no absorption; this curve scales freely with λ, and m-1. Q_s is the scattering efficiency, Q_a the absorption efficiency for the particular case $\tan\beta = 0.034$ (e.g., $MgSiO_3$ at 6 keV). The upper scale illustrates the example of $MgSiO_3$ grains and 6 keV photons.

Fig. 2. The normalized differential cross section is plotted versus the appropriately scaled scattering angle. The Anomalous Diffraction curve is appropriate to the problem discussed in the text, but the analytically simpler Rayleigh-Gans curve is used for computations.

Fig. 3. The progress of a photon (wiggly line) suffering occasional scatterings is shown. Without loss of generality we assume that the photon starts out along the z-axis, and after its first scattering remains in the xz-plane. The ℓ_i are lengths between vertices, the ξ_i are azimuthal angles, the φ_i are angles made to a radius vector.

Fig. 4. The geometry used to derive equation (11a): O is the origin, P and Q are the intersections of a photon trajectory (wiggly line) with two radius vectors. The lengths of the radii are given in units of optical depth.

Fig. 5. The geometry used in the evaluation of the singly scattered photon distribution. The loci of constant delay are confocal ellipses. The arrival angles (φ) and delays (t) are simply related to scattering angle (θ) and fractional distance (α), whose distribution functions are known.

Fig. 6. The joint probability density function $P(\chi^2,\eta)$ for singly scattered photons (Rayleigh-Gans cross section).

Fig. 7. The normalized intensity distribution of the halo of singly scattered photons, when integrated over time delay (Rayleigh-Gans case). The asymptote $(2/15\chi)$ for small χ is shown.

Fig. 8. The probability density function $P(\eta)$ for singly scattered photons (Rayleigh-Gans case). The analytic fit, equation (25), is dashed where it differs noticeably from $P(\eta)$.

Fig. 9. The function $G(x,y)$ which describes the joint probability density function in ω^2 and t for photons in the limit $\tau \gg 1$.

Fig. 10. The function $G(y)$ which describes the probability density function in t for photons in the large τ limit. The leading term in equation (25) is dashed.

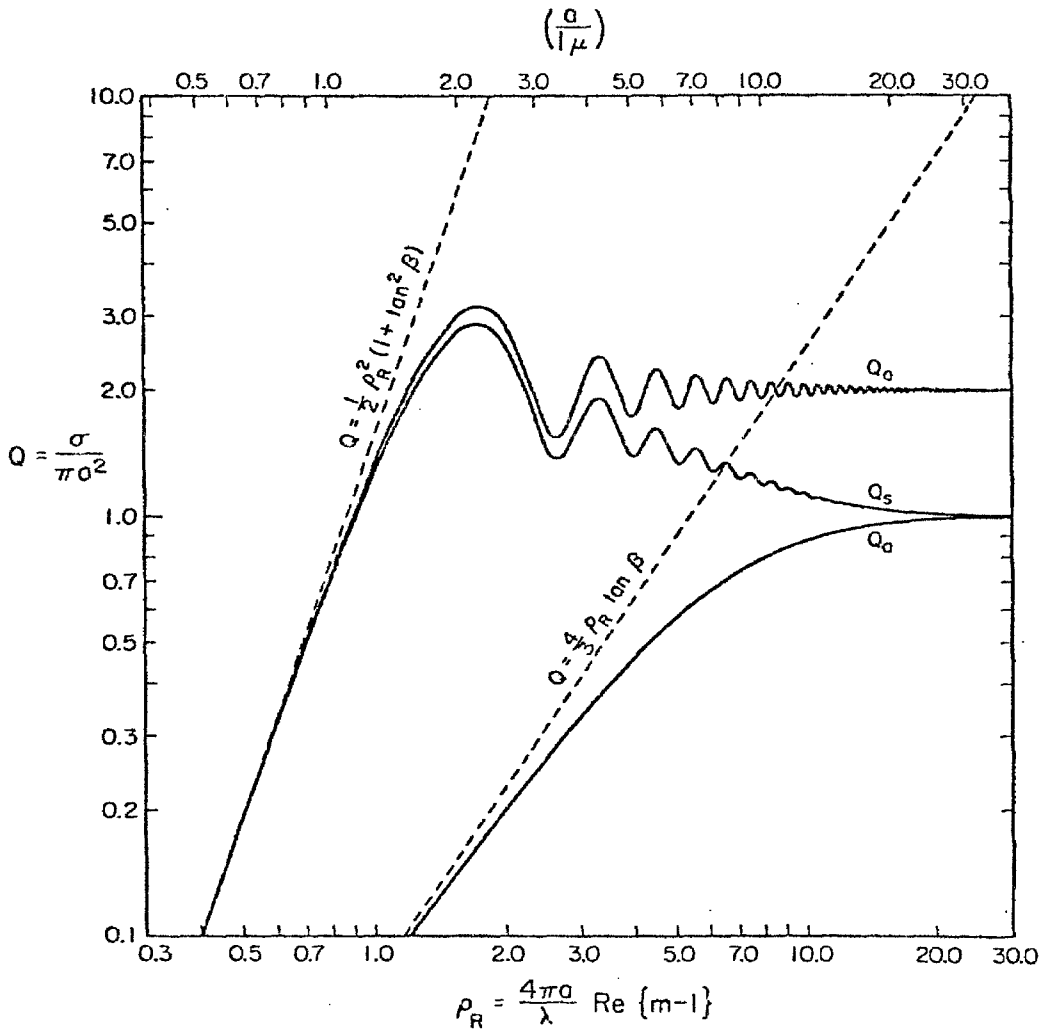
$\left(\frac{a}{|\mu|}\right)$
0.5 0.7 1.0 2.0 3.0 5.0 7.0 10.0 20.0 30.0
10.0 7.0 5.0 3.0 2.0 1.0 0.7 0.5 0.3 0.2 0.1
$Q = \frac{\sigma}{\pi a^2}$
$Q = \frac{1}{2}\rho_R^2(1+\tan^2\beta)$
$Q = 4\rho_R \tan\beta$
Q_a
Q_s
Q_a
0.3 0.5 0.7 1.0 2.0 3.0 5.0 7.0 10.0 20.0 30.0
$\rho_R = \frac{4\pi a}{\lambda}\,\mathrm{Re}\,\{m-1\}$

Fig. 1

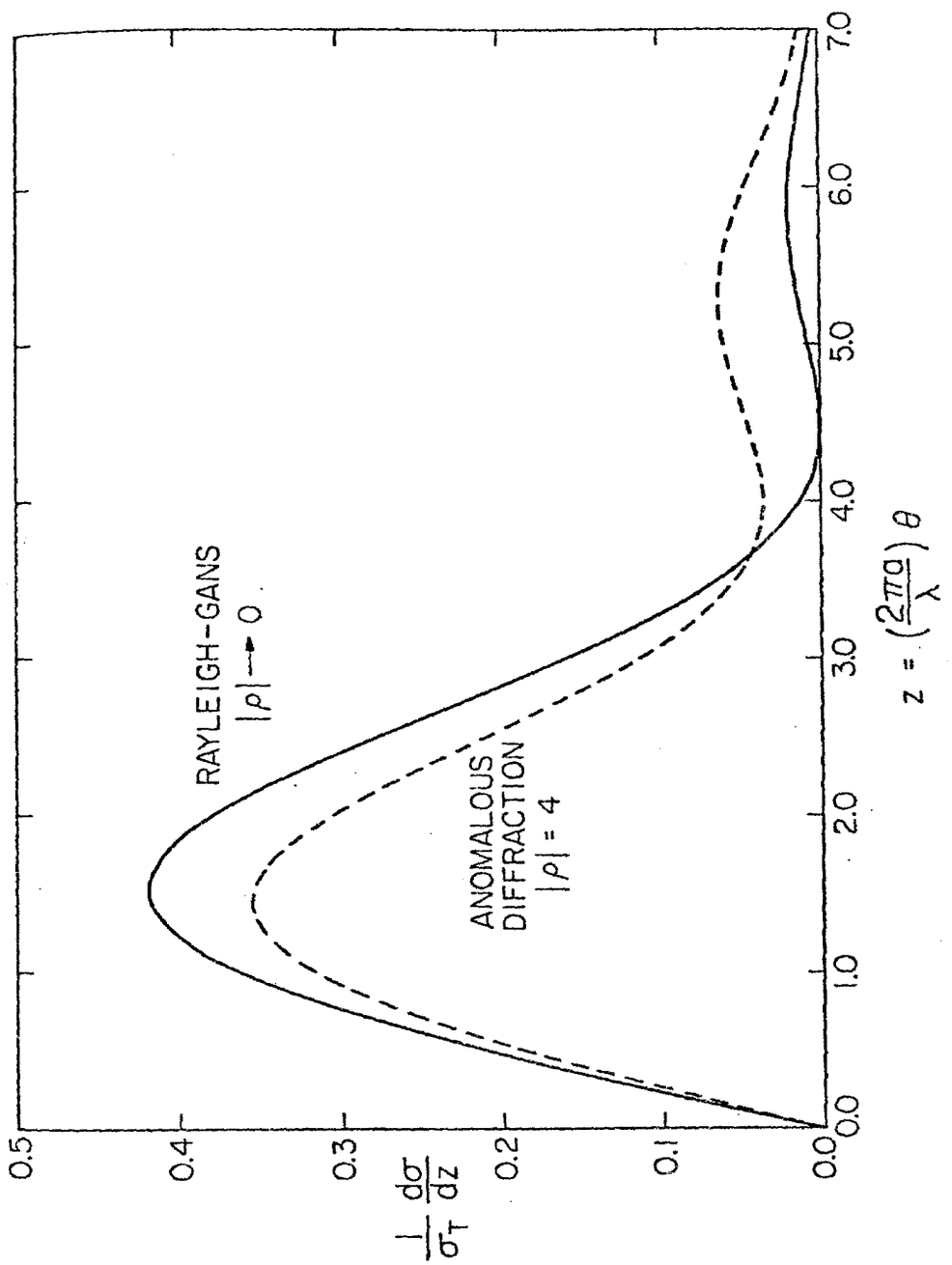
RAYLEIGH-GANS
|ρ| → 0
ANOMALOUS
DIFFRACTION
|ρ| = 4
0.0
0.1
0.2
0.3
0.4
0.5
1.0
2.0
3.0
4.0
5.0
6.0
7.0
$\frac{1}{\sigma_T}\frac{d\sigma}{dz}$
$z = (\frac{2\pi a}{\lambda})\theta$

Fig. 2

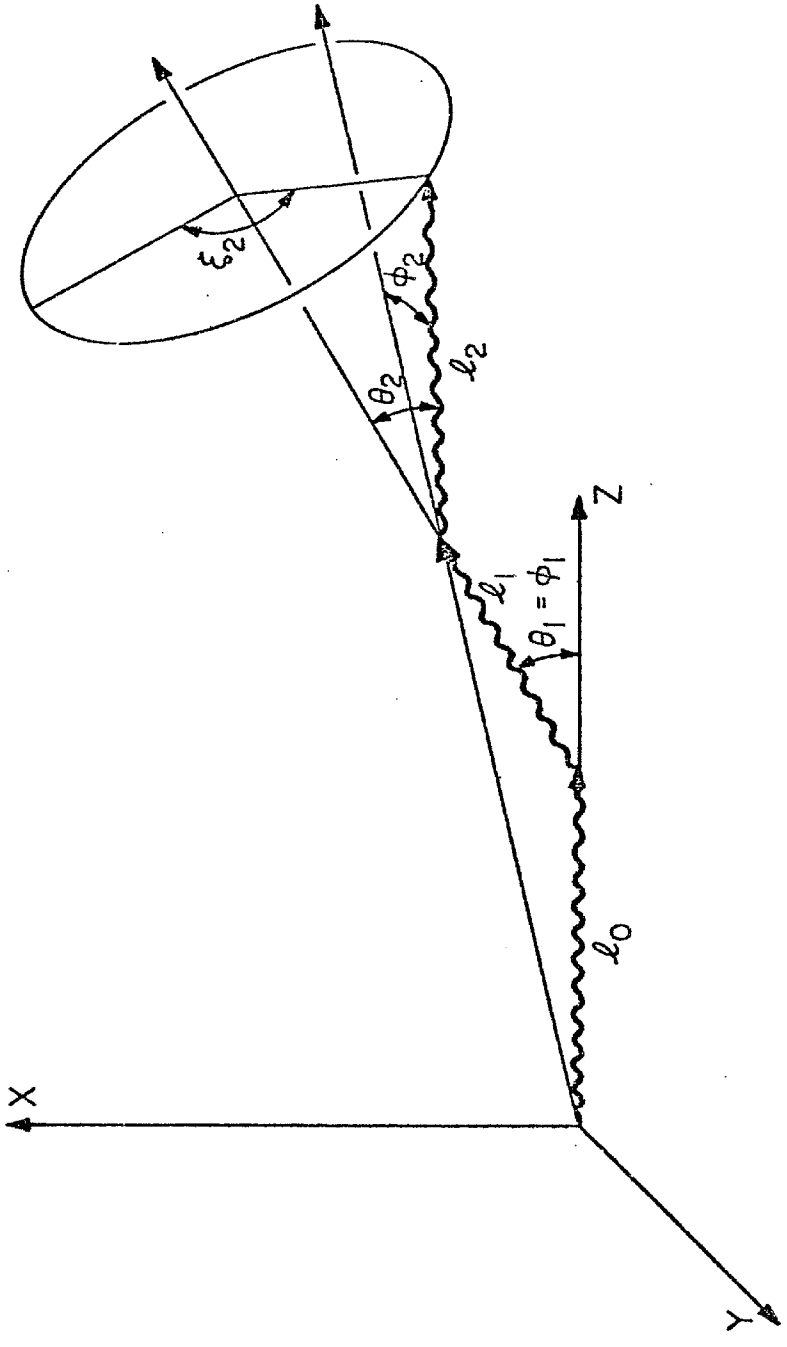

Fig. 3

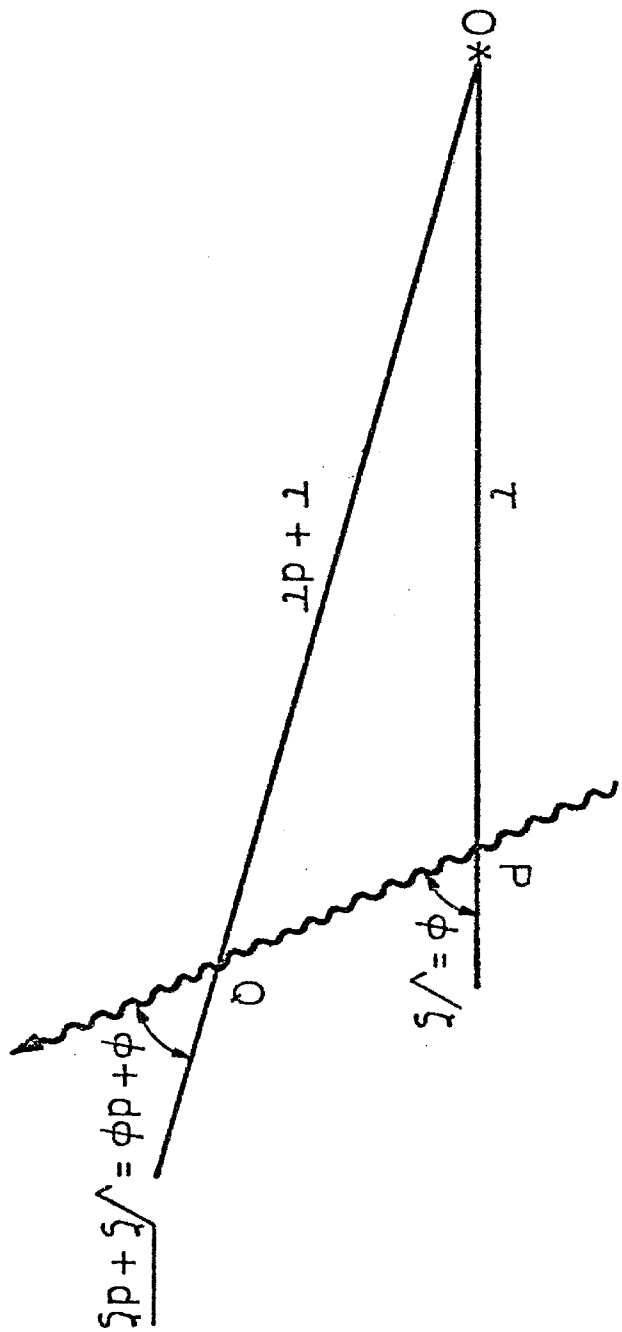

Fig. 4

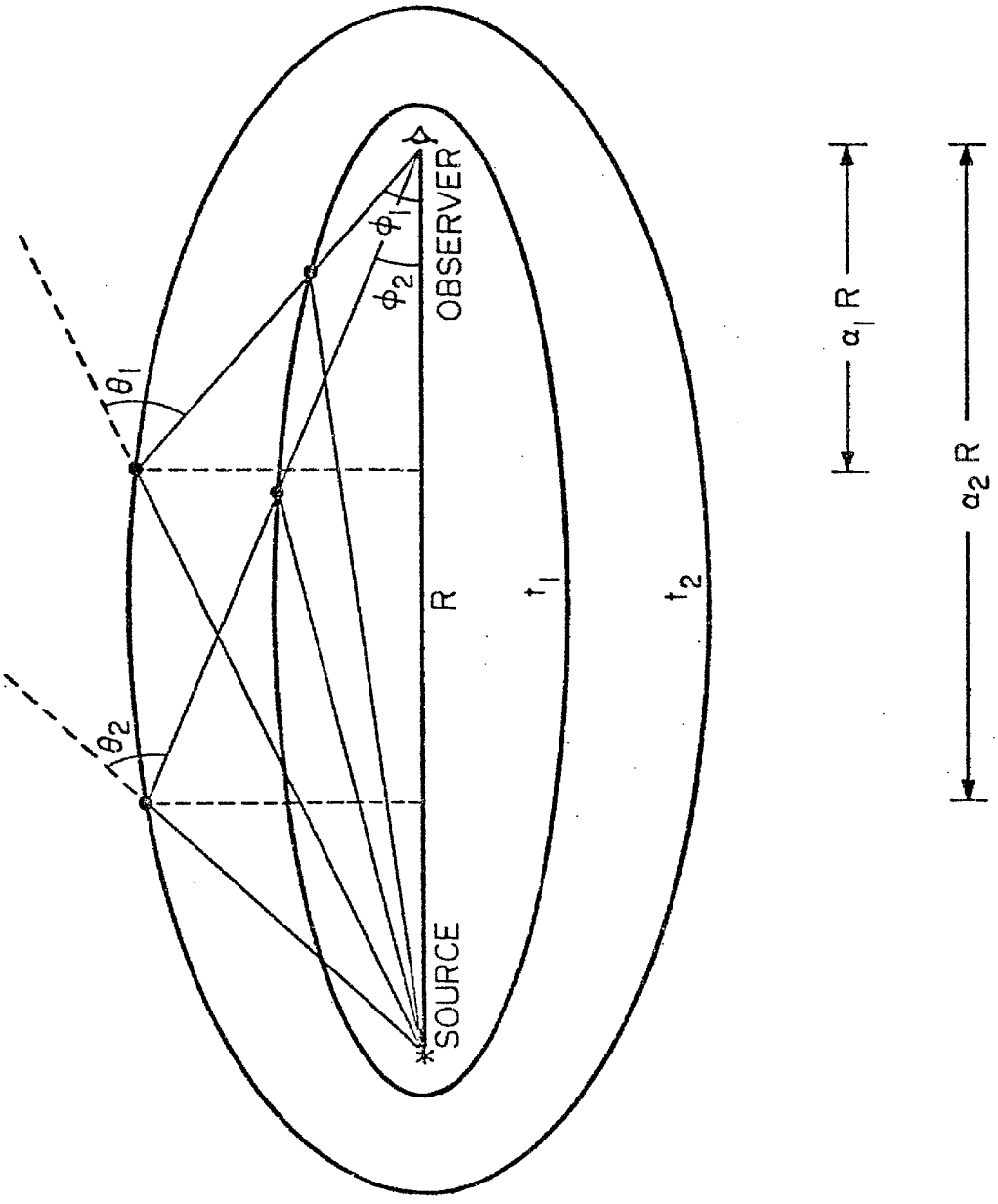

Fig. 5

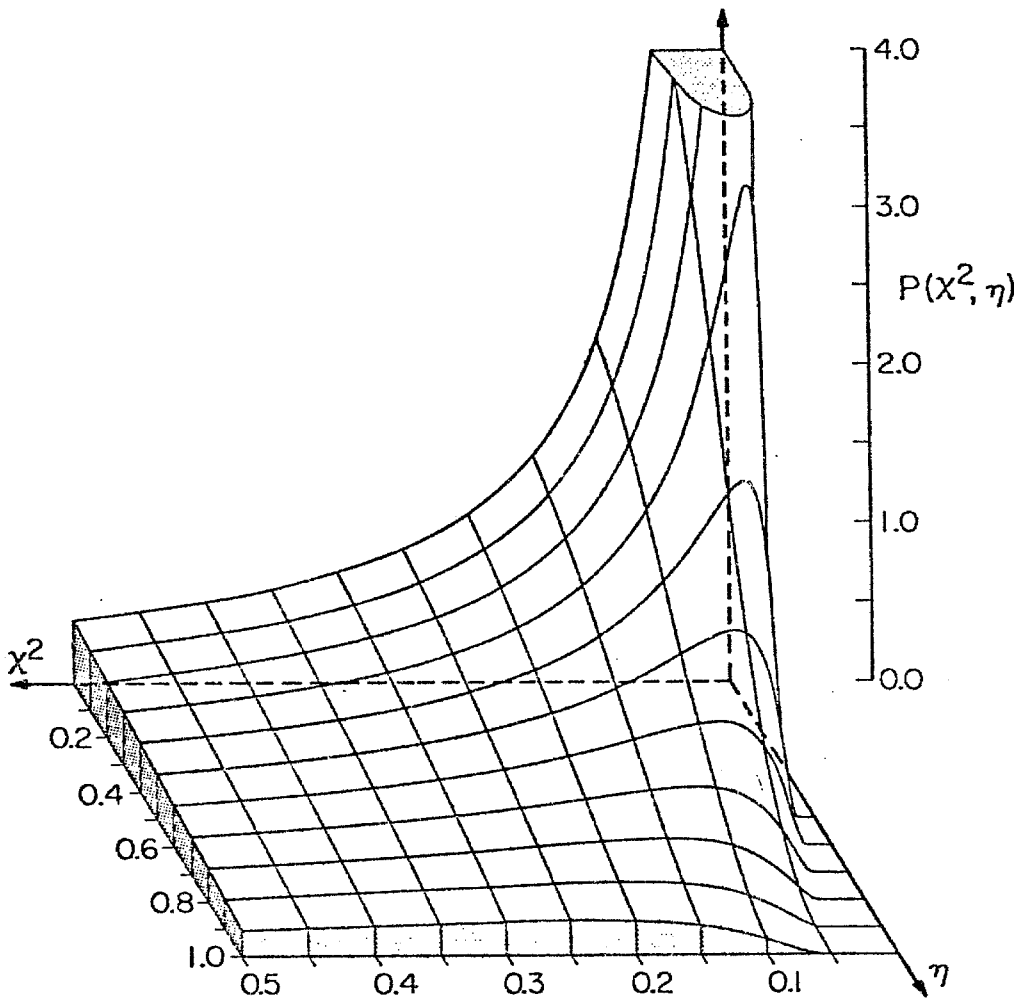

Fig. 6

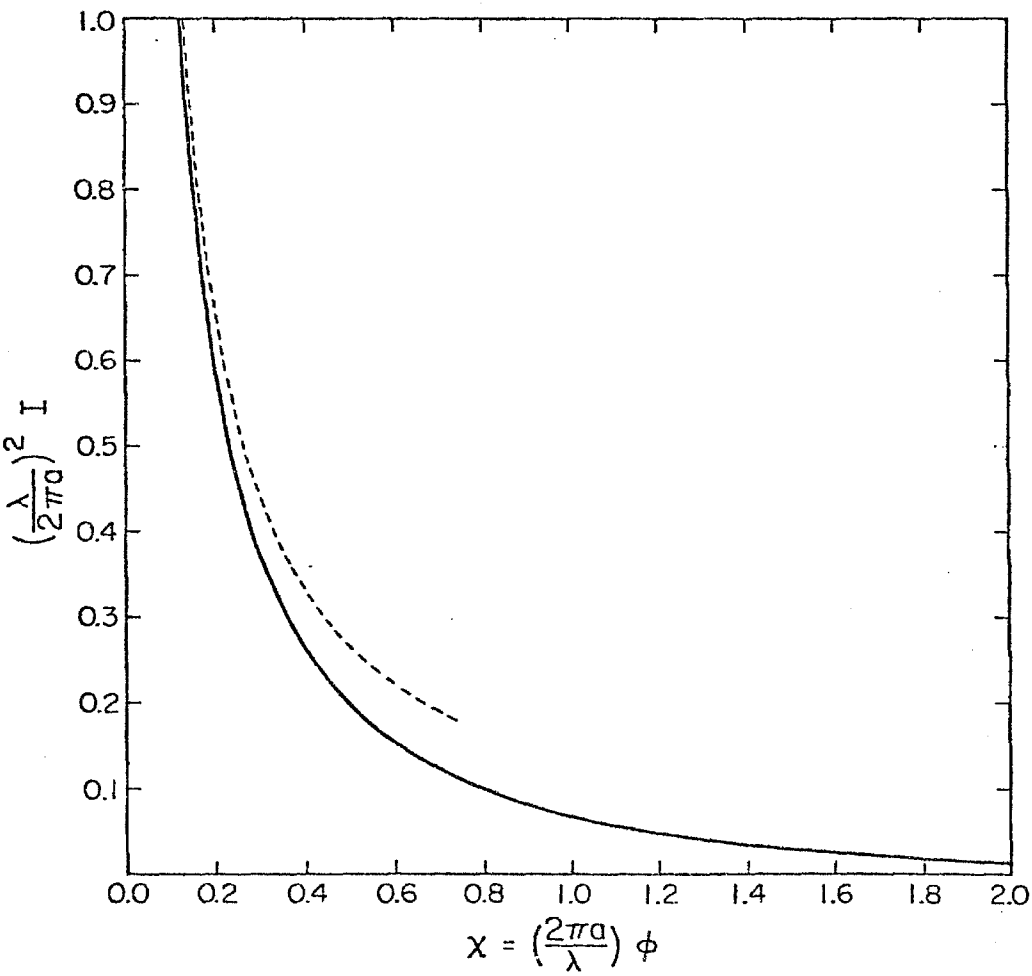
1.0
0.9
0.8
0.7
0.6
0.5
0.4
0.3
0.2
0.1
$(\frac{\lambda}{2\pi a})^2 I$
0.0
0.2
0.4
0.6
0.8
1.0
1.2
1.4
1.6
1.8
2.0
$\chi = (\frac{2\pi a}{\lambda})\,\phi$

Fig. 7

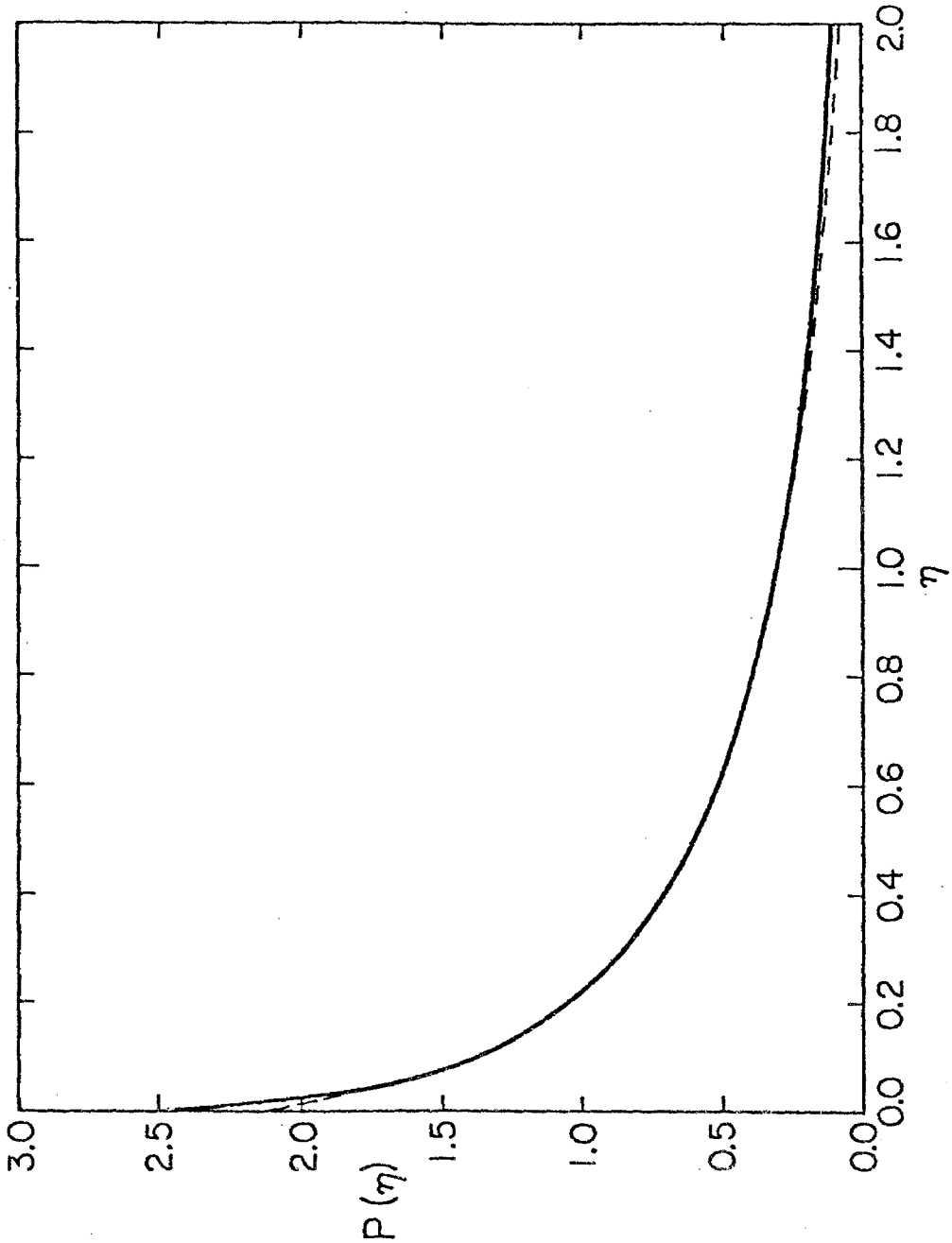

Fig. 8

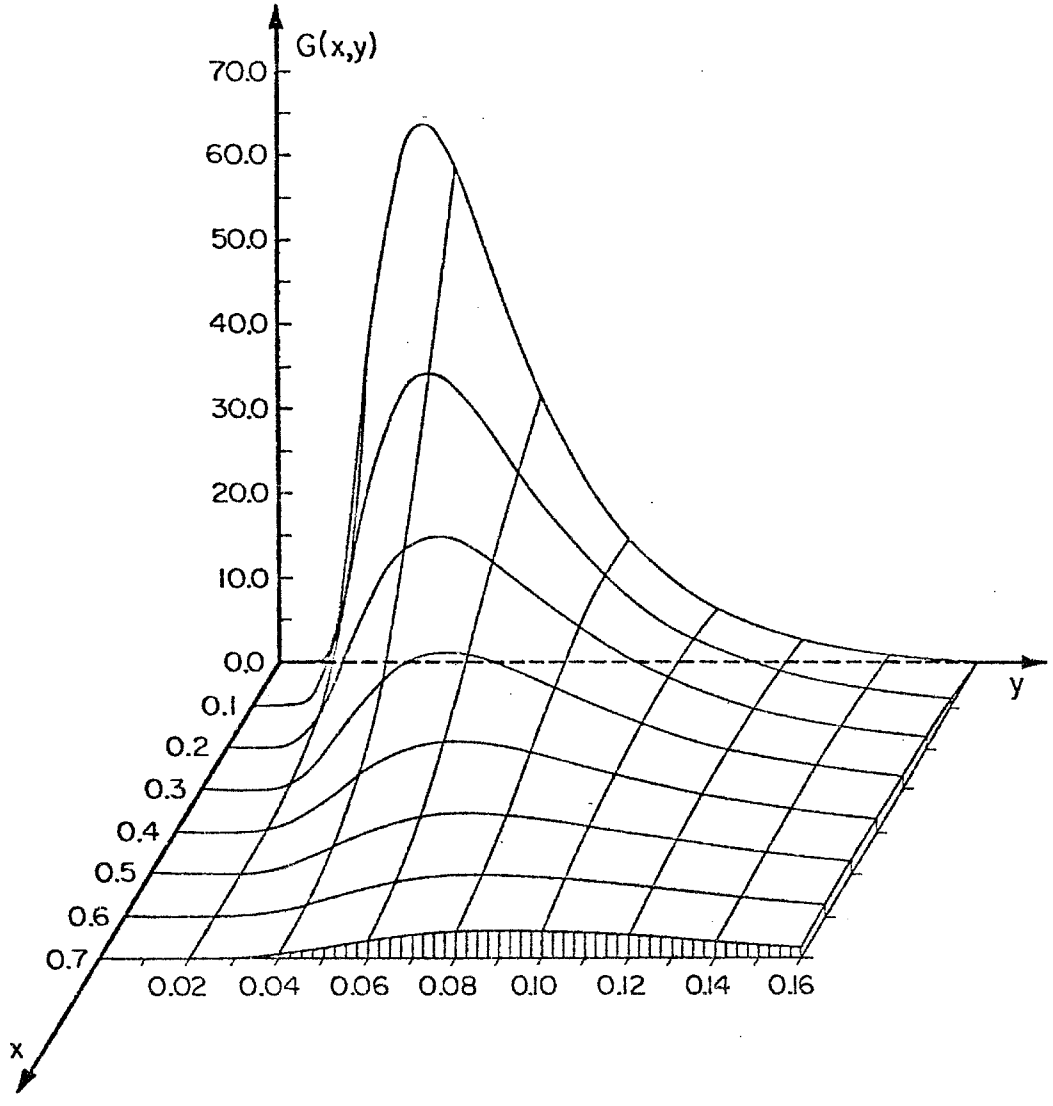
G(x,y)
70.0
60.0
50.0
40.0
30.0
20.0
10.0
0.0
y
0.1
0.2
0.3
0.4
0.5
0.6
0.7
x
0.02
0.04
0.06
0.08
0.10
0.12
0.14
0.16

Fig. 9

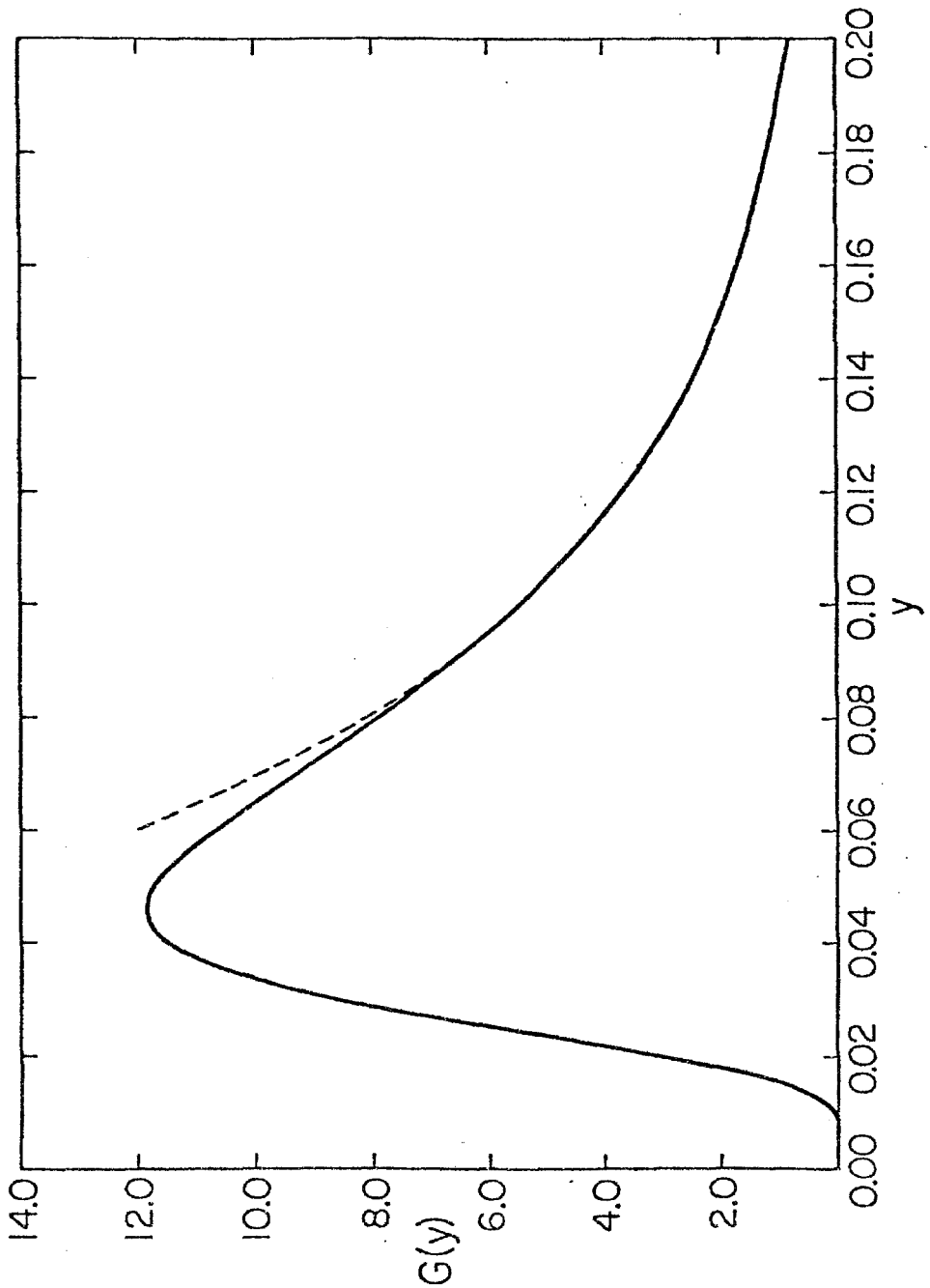
14.0
12.0
10.0
8.0
6.0
4.0
2.0
G(y)
0.00
0.02
0.04
0.06
0.08
0.10
0.12
0.14
0.16
0.18
0.20
y

Fig. 10

PAPER 2

MOLECULAR EMISSION FROM EXPANDING ENVELOPES AROUND EVOLVED STARS
I. NON-MASER SiO EMISSION LINES

by

Mark Morris
Owens Valley Radio Observatory
California Institute of Technology
Pasadena, California

Charles Alcock
Department of Astronomy
California Institute of Technology
Pasadena, California

Received: _____

ABSTRACT

We have investigated the excitation of the microwave lines in the ground vibrational state of the SiO molecule in the expanding envelope of cool Mira-type stars. The rotational levels are excited when an SiO molecule absorbs an 8μ photon and is left in the lowest excited vibrational state; the spontaneous decay of the excited vibrational state preferentially leaves the molecule with a higher rotational quantum number than it had before. In all of the cases investigated the majority of the microwave transitions were optically thick, and photon trapping causes the excitation temperature to increase with optical depth in such a way that the antenna temperature measured by a distant observer is proportional to the flux of SiO leaving the star, to the square root of the ambient 8μ flux and inversely to the square of the asymptotic velocity. We have analysed the reported detection of $J=2\rightarrow1$, $v=0$ emission from three Miras and VY CMa, and find that the flux of SiO leaving the stars is very low. This indicates that either they are losing very little mass, or more probably that grain formation very effectively removes a large fraction of gaseous SiO molecules.

§I. INTRODUCTION

Our understanding of mass loss from evolved stars has been considerably improved by the observation and interpretation of radio molecular lines arising in the expanding envelopes surrounding such stars. The most thoroughly studied molecular lines have been the maser emission lines of OH, H_2O and SiO, which have been observed towards many oxygen-rich Mira variable and M supergiant stars. The non-linear character of maser emission creates many difficulties in the interpretation of the observed spectra, and these problems motivate a deeper study of non-maser lines.

Many non-maser molecular emission lines have been observed in the expanding circumstellar envelope around IRC+10216, an object which appears to be an outstanding example of a class of carbon-rich stars (Zuckerman et al. 1976). The excitation of these lines has been analyzed by Morris (1975) and Kwan and Hill (1977). Recently, the increased sensitivity of radio receivers at millimeter wavelengths has allowed the detection of non-maser emission from SiO in several oxygen-rich objects (Buhl et al. 1975) and from CO in a number of carbon- and oxygen-rich objects (Zuckerman et al. 1977). In all cases these "thermal" lines are broad compared to those arising in galactic molecular clouds, characteristic of the expansion of the envelopes at velocities between 6 and 20 Km s^{-1}.

In this paper, we consider the non-maser emission from SiO in oxygen-rich circumstellar envelopes. By analysing the excitation processes and calculating line profiles, we hope to demonstrate

that non-maser emission lines may provide the most powerful means for determining such important physical parameters as the mass loss rate and the fractional abundances of many common molecules. The observations by Buhl et al. (1975) of the J=2→1, v=0 SiO line are limited to only 4 stars, but there is every reason to expect that such measurements can be extended to a large number of objects. Reid and Dickinson (1976) have used these observations to help solve the long-standing problem of the determination of true stellar velocities. Their interpretation is unambiguous if the v=0 SiO lines are not inverted and arise symmetrically from the entire envelope. The results presented below indicate that these assumptions appear to be valid.

We show in §II that the "thermal" SiO lines are ultimately excited by the 8μ infrared radiation field rather than by collisions, and decribe how the excitation process works. The detailed radiative transfer calculations for molecules in a spherically symmetric, expanding, circumstellar envelope are described in §III. In §IV, the resulting line profiles are presented, and in §V these are compared to the existing observations.

§II. EXCITATION OF THE ROTATIONAL LEVELS

We will first illustrate how the absorption of 8μ photons can populate levels of high rotational quantum number (J) in the ground vibrational state, (v=0) and then show that this process is more important than collisions with the H_2 molecules in the envelope.

The rate of absorption of infrared photons per molecule in a given rotational level of the ground vibrational state is:

$$R_{IR} = \frac{A}{(\exp\ (\frac{h\nu}{kT_*}) - 1)} \qquad (\frac{W}{4})\ (\frac{R_*}{r})^2$$

where A is the Einstein A coefficient for the v=0→1 transition of SiO (A = 4.1 s^{-1}, Hedelund & Lambert 1972,) T_* and R_* are the surface temperature and radius of the central star, W is the factor by which the 8μ flux exceeds the direct stellar contribution (due to dust re-emission) and r is the distance from the center of the star.

After a molecule (with initial rotational quantum number J) has absorbed an 8μ photon, it almost immediately re-emits another photon and decays back down to the ground vibrational state. The branching ratios between different vibration-rotation transitions will produce an average upward shift in the rotational ladder. If we define b^+, b^o and b^- to be the fraction of 8μ observations that lead to a shift in J in the ground vibrational state of +2, 0 and -2 respectively, then:

$$b^+ = \frac{2}{3} \qquad J=0$$

$$= \frac{2}{5} \qquad J=1$$

$$= \frac{(J+2)\,(J+1)}{(2J+3)\,(2J+1)} \qquad J\geq 2$$

$$b^- = 0 \qquad J=0,\ 1$$

$$= \frac{(J-1)J}{(2J-1\,(2J+1)} \qquad J\geq 2$$

$$b^o = 1-b^+ -b^-$$

In this way the 8μ photons preferentially populate the higher J levels in the ground vibrational state. The even-J

and odd-J ladders do not communicate via the infrared photons and are coupled together only by spontaneous emission in the microwave transitions, and by collisions. In general the collision rates greatly exceed the Einstein A values for these transitions. The first-order separation of even and odd J ladders only becomes important when there is some tendency to invert microwave transitions (which may occur if some of the infrared transitions become optically thick) and we stress that no computed inversion in the v=0 microwave transitions can be believed unless collisions have been included in the calculation. In the computations presented here the microwave emission distributes the populations about equally between the odd and even J levels, and hence the inclusion of collisions would have made a negligible difference. This was tested by including collisions in the computation of a test case.

We now show that this infrared pumping rate is faster than the collision rate in redistributing population among the ground vibrational levels. The net collision rate out of a level is approximately:

$$R_c \approx \frac{\dot{M}\,\sigma\,V_t}{4\pi r^2\, m_{H_2}\, V}$$

where $\dot{M}$ is the mass loss rate for the star, V the expansion velocity, σ (assumed to be 2×10^{-15} cm^2) is the cross-section for collisional transitions, m_{H_2} is the mass of the hydrogen molecule and V_t is the mean thermal velocity of the hydrogen molecules. If we assume $T_* = 2000\ ^oK$ then

$$\frac{R_{IR}}{R_c} \approx 56 \times \left(\frac{W}{4}\right) \times \left(\frac{2\times10^{-6}\ M_\odot\ yr^{-1}}{\dot{M}}\right) \times \left(\frac{V}{10\ km\ s^{-1}}\right) \times \left(\frac{R_*}{5\times10^{13}cm}\right)^2 \times \left(\frac{10\ ^oK}{T_g}\right)^{1/2}$$

where T_g is the gas temperature. For reasonable physical parameters, R_{IR} is much greater than R_c, and the 8μ photons seem to dominate the excitation of the rotational levels. The computations described in §III support this conclusion. If $\dot{M}$ were as high as $\sim10^{-5}\ M_\odot\ yr^{-1}$ then collisions might begin to have an effect upon the excitation, but it is unlikely that $\dot{M}$ is that high in the objects we are modelling. Note, however, that as $\dot{M}$ increases, W will increase because the amount of dust available to convert stellar photons to 8μ photons increases. This will partially counteract the increasing importance of collisions.

The conclusion that infrared excitation dominates holds true only as long as the vibration-rotation transitions are not optically thick in the radial direction. For the range of physical conditions considered in this paper, the radial optical depths in the 8 μ lines are indeed less than unity. However, we have assumed throughout that ΔV, the local linewidth due to thermal broadening plus microturbulence, is ~1 km s^{-1}. If ΔV is actually much less than this value, the radial optical depths of the infrared lines, which are inversely proportional to ΔV, may exceed unity in spite of the finite velocity gradient in the radial direction. In this paper we have assumed that the radial optical depth at 8 μ is small, both in the lines and the continuum, in the outer regions where the gas has approached its

asymptotic velocity to within ΔV. If microturbulence does not contribute to the linewidth then $\Delta V \ll 1$ km s^{-1} and extinction of the infrared lines, and thus also collisional excitation, must be taken into account.

§III. RADIATIVE TRANSFER CALCULATIONS

We assume a spherically symmetric envelope expanding away from a star which is losing mass at a constant rate. Minor deviations from either of these assumptions will not appreciably change the conclusions of this paper. The circumstellar material is presumably being accelerated radially with an ever-decreasing velocity gradient until it arrives at its asymptotic velocity.

As will be shown, most of the millimeter-wavelength SiO emission comes from the outer envelope ($r > 5 \times 10^{16}$ cm) well removed from the star. In this region we may safely assume that the expanding material has arrived at its asymptotic velocity to within the thermal velocity width of the gas (Goldreich and Scoville 1976). Therefore, we can also make the assumption that the outer envelope is expanding with uniform velocity, V_a, which simplifies the calculations.

A given molecule, at rest with respect to the expanding material, is thus in radiative contact only with other molecules which lie in the cone whose apex is centered on the star, and whose axis passes through the given molecule. (Two molecules are in radiative contact if their relative velocity is smaller than the local linewidth due to thermal broadening plus microturbulence.) The apex angle of this cone, assuming a rectangular

local line profile, is given by $\theta = 2 \sin^{-1} (\Delta V/V_a)$. Because expansion velocities of envelopes of Mira variables and M supergiants are large (5-20 km s^{-1}) compared to what one might expect the local linewidth to be ($\leq$1 km s^{-1}), θ is generally quite small. This simplifies the radiative transfer problem: to derive the radiation field at a given point, we have only to deal with the relatively simple geometry of a long, narrow cone. Thus the problem can be reduced numerically to a one-dimensional integration by dividing the narrow cone into radial zones (disks). The level populations in each zone are found by: 1) summing the radiation field from all zones in the cone and from the star, 2) using the resultant angle-averaged line intensities in a statistical equilibrium calculation to get the level populations, and 3) repeating this procedure iteratively until the level populations in all zones relax to a solution.

In deriving the radiation field in a given rotational line at the center of a given zone, we consider four contributions: 1) radiation from external zones, 2) radiation from internal zones, 3) radiation from the given zone, and 4) the cosmic background radiation, reduced by an optical depth factor and averaged over angle. The intensity contribution of each zone at a given point has been modified appropriately for the intervening optical depth and for the solid angle subtended by the zone at the given point. Furthermore, the interior or exterior zones which are velocity shifted by more than one linewidth from the given zone are excluded from contributing to the intensity in the given zone. The velocity field is taken from Goldreich and Scoville (1976). As it happens, zones are rarely excluded because the velocity gradient at the large radii being considered is rather small.

For our numerical calculations, we found it adequate to divide the cone of radiative contact into 32 zones. The outer radius was taken to be 3.0×10^{17} cm, the radius at which the excitation temperature across the transitions of interest becomes approximately equal to the background radiation temperature. Only about 10% of the total intensity in the J=1→0 line arises between 1.5 and 3.0×10^{17} cm; for transitions between higher levels, an even smaller percentage of the total flux arises in this region. Nineteen rotational levels in each of the lowest two vibrational states were included in the calculations; higher vibrational states were not included because the $\Delta v=2$ line strengths are much smaller than those for $\Delta v=1$, and because the v=1 rotational level populations are negligibly small.

As mentioned in §II, we normally assumed $\Delta V=1$ km s^{-1} (with the exception of the calculations for $V_a = 10$ km s^{-1}, for which $\Delta V=0.6$ Km s^{-1}). An investigation into the dependence of the results upon ΔV revealed that the calculated line intensities are rather insensitive to ΔV: a factor of two change in ΔV in either direction causes only about a 10% change in line intensities in the opposite direction. The effect of decreasing ΔV is 1) to increase the radial optical depth, which in turn increases the importance of trapping of the millimeter-wavelength photons for determining the level populations [the optical depth perpendicular to the radial direction is independent of ΔV - see eqn.1 of Morris (1975)], and 2) to change the geometry by narrowing the cone of radiative contact. Only the first of these effects will change the line intensities significantly. If ΔV is decreased to less than 0.5 km s^{-1}, then extinction of the

8 μ lines might become important and the calculated rotational line intensities would correspondingly decrease.

The results of this paper are expressed as functions of three parameters: the asymptotic velocity of the ejected gas, the mass loss rate of SiO molecules from the star, and the flux of 8 μ photons arising near the star. Three values of the asymptotic velocity are considered: 6, 10, and 17 km s^{-1}, covering the range observed in the non-maser SiO lines and the OH and H_2O masers. The mass loss rate of SiO is expressed as the product of $\dot{M}$, the total mass loss rate, and f, the mass fraction of SiO in the ejecta. For simplicity, we assume that f is constant in the envelope.

The variation with radius of the excitation temperature (T_{ex}) and the optical depth perpendicular to the radius vector (τ) are shown in figure 1 for three values of $f\dot{M}$. As $f\dot{M}$ increases, τ increases approximately proportionately, as might be expected. As τ increases, the number of trapped photons in the microwave lines increases, leading to the increase in the excitation temperature of those lines. Note that for the assumed physical parameters, the optical depth for the rotational lines is only moderately large tangentially whereas it is very large in the radial direction. Therefore, a photon preferentially escapes tangentially.

Because of the greater area subtended on the sky at larger distances from the star, most of the flux in the J=1→0 line arises between 5 and 2 x 10^{16} cm. The inversion found in

the 1→0 line in the zones nearest the star does not affect the total fluxes very much because it occurs over such a relatively small volume. However, our zones may be too coarse to assess it properly. Furthermore, such inversions tend to disappear when collisions are included (see below). We consider the possibility of maser radiation arising near the star as a separate problem and will address it in a later paper in this series. Higher-lying rotational transitions behave similarly to the J=1→0, except that they do not display inversions close to the star, and their excitation temperatures decline more abruptly away from the star.

The curves shown in figure 1 have been calculated under the assumption that collisions have negligible importance in determining the level populations. To test this assumption, the calculations were redone with the inclusion of collisions. A total cross section of 2×10^{-15} cm^2 was assumed for SiO, the kinetic temperature of the gas versus radius was taken from Goldreich and Scoville (1976), and $\dot{M}$ was assumed to be 1.3×10^{-6} $M_\odot/yr$. The resulting curves are negligibly different from those in figure 1 with the exception of the inner few zones, which contribute very little to the total intensity. The calculated line intensities (table 1) are also negligibly different between the models with and without collisions. Therefore, we feel justified in neglecting collisions throughout the remainder of this paper, although when precise observations become available, it will be worthwhile to redo the calculations with the inclusion of collisions for those situations in which the total mass loss rate exceeds a few times 10^{-6} $M_\odot/yr$.

The flux of 8 μ photons is estimated by assuming that the central star has $T_* = 2000$ K and $R_* = 2 \times 10^{13}$ cm, and that dust immediately surrounding the star converts much of the optical and near-infrared stellar flux to 8μ photons. To parameterize this, we multiply the stellar 8 μ flux (that would occur in the absence of extinction) by a factor W. If we imagine that the dust reradiates the stellar luminosity as if it were an optically thick, spherical surface, then we can calculate the maximum possible W as a function of the radius of that surface. In this way we find that $W < 10.6$ (19.6) for a star of surface temperature 2000 K (2500 K), the maximum occuring when the surface has a radius $\approx 19R_*$ ($31R_*$). Observations of cool stars undergoing mass loss (e.g., Gehrz and Woolf 1971; Gillett et al. 1971; Hyland et al. 1972) indicate that W varies between 1.5 and 10. We vary the 8 μ flux by investigating three values of W: 2, 4, and 8. Figure 2 shows how T_{ex} and τ vary with radius for three values of W. An increase in W increases T_{ex} at all radii because the increased 8 μ flux forces the rotational levels closer to thermal equilibrium at the high effective temperature of the infrared radiation field. The optical depth decreases as W increases, however, because more of the population is pushed to higher rotational levels at the expense of the populations of the lower levels.

§IV. LINE INTENSITIES AND PROFILES

After the solution for the level populations was found, the emission was integrated numerically over the envelope according to equation (2) of Morris (1975). The assumptions which led to this equation are the same as are invoked in the present paper, notably $\Delta V << V_a$.

The assumed beam response function for each rotational line is a Gaussian with a full halfpower beamwidth equal to that of the 11-m NRAO radiotelescope at Kitt Peak, where observations of the circumstellar SiO lines have all been made to date. In fact, since the size of the emitting region is smaller than the assumed telescope beam size in our model where the source is 500 pc distant, the results are not sensitive to the form of the beam response functions. Furthermore, the derived intensities can be scaled down for telescopes with larger beam widths simply by the ratio of main beam solid angles. For telescopes with significantly higher resolution than the 11-m telescope, or for objects much closer than 500 pc, the beam response function becomes important for determining the shape of the line as well as the intensity. For example, if the emitting region is resolved, a double peaked structure probably would be seen in the center of the region.

Table 1 lists the peak intensities (in terms of antenna temperature assuming no telescope or atmospheric losses) derived in our model calculations for the J=1→0 through J=4→3 lines. The most interesting result is that the antenna temperatures vary almost linearly with $\dot{f}_M$ for these transitions. This numerical result and the others presented below can be derived analytically; Appendix I gives a derivation of the dependences of T_A upon the various input parameters. Because all but the J=1→0 transition are optically thick throughout the envelope in all cases, we have here a clear example of photon trapping in a microwave line. If in a given model the number density of molecules increases, the number of trapped photons increases because of the increased optical depth, and thus the excitation temperature increases proportionately. The approximately

linear variation of T_A with $\dot{fM}$ (and thus with optical depth) over the whole range of parameters which were considered suggests that one may easily extrapolate our results to larger or smaller values of $\dot{fM}$. Of course, in the optically thin limit, the line intensities increase linearly with $\dot{fM}$, but in this case it is the increase of τ rather than T_{ex} that is directly responsible for the intensity increase. The line intensities vary with W less strongly than linearly--over the limited range investigated, $T_A \alpha W^{0.4-0.6}$.

For given values of $\dot{fM}$ and W, the line intensities decrease roughly as V_a^{-2}. This can be seen from table 1 by interpolation and the use of the linear dependence of T_A on $\dot{fM}$. The reasons for this are twofold: 1) for a given $\dot{fM}$, the density at any point is inversely proportional to V_a (conservation of mass flux across any spherical shell centered on the star), and 2) the apex angle of the cone of radiative contact is inversely proportional to V_a. Therefore the expression for τ contains two factors of V_a^{-1}.* We noted above that $T_A \alpha \tau$, and so $T_A \alpha V_A^{-2}$. This

*This is true of equation (1) of Morris (1975) if one notices that $k \alpha V_a^{-1}$

implies an observational selection effect against the detection of "thermal" radiation from molecules in circumstellar envelopes with relatively large asymptotic velocities. This bias would not arise if such objects had high mass loss rates, but this is unlikely because the radial momenta of the envelopes becomes in probably high.

If the intensities listed in table 1 are all corrected for aperture effects, i.e., if relative beam dilution of the signal

is removed, one sees that the 2→1 line is intrinsically the strongest in all cases. Thus it is no surprise that this is the first and only line detected to date. The relative line intensities vary as the physical parameters of the envelope vary and thus a measurement of, say, the J=2→1 and 3→2 lines in the same object would help sort out the values of $f\dot{M}$, W, and the distance to the source.

In all of the models which were investigated, the J=2→1 and the next few higher-lying transitions are optically thick. Morris (1975) has pointed out that optically thick lines arising from spherically symmetric, uniformly expanding envelopes have parabolic line profiles. Such is the case with our calculated line profiles for the J=2→1 and higher transitions. The J=1→0 line, however, often has an optical depth that is small or near unity, and therefore the profile has a shape that is intermediate between rectangular and parabolic. Because the profile of the J=1→0 line varies with the physical parameters of the circumstellar envelope, it provides useful independent information on the envelope parameters. With this in mind, we display in figures 3-5 the calculated J=1→0 line profiles for various values of V_a, $f\dot{M}$, and W. The indicated antenna temperatures scale with distance as $(500\ pc/D)^2$ unless D is much smaller than 500 pc, in which case the line shape and intensity are affected by the form of the beam response function.

§V. COMPARISON WITH OBSERVATIONS

Ideally one would have 5 important pieces of information from observations of the non-maser SiO lines towards a given star:

1) the line center velocities, which yield immediately the stellar velocity (Reid and Dickinson 1976), 2) the full line widths which lead immediately to the asymptotic expansion velocity, V_a, 3) the shape of the J=1→0 line, which gives an indication of the mean optical depth of this line, 4)the absolute intensity of a given line, and 5) the relative line intensities. Measurements 3, 4, and 5,. if accurate enough, can in principle provide a determination of $f\dot{M}$, W and the distance to the star, D, through a detailed comparison with the calculations. If W and/or D are independently determined from infrared or optical observations, then the remaining quantities can be fitted quite simply to our model. In fact, W for a large number of stars can be determined from existing infrared observation apart from a dependence on D. Note that for a comparison with observations, W must reflect not only reradiation by dust as in our models, but also the differences between our standard star and the actual stars under study.

The observations to date consist of only the J=2→1 line measured towards 4 stars. Therefore, we need to derive both W and D from independent observations. To see how strongly the result depends on measurable and assumed quantities, we start with the result discussed in §4 that

$$(1) \qquad T_A \propto \frac{W^{\frac{1}{2}} f \dot{M}}{V_a^2 D^2}$$

The dilution factor W can be expressed in terms of the measured 8 μ flux from the star, $F_{8\mu}$, the estimated distance D and the specific luminosity $L^{o}_{8\mu}$ of our "model star" (a 2000 ^{o}K spherical black body with radius 6×10^{13} cm.) The distance to each of the

stars analysed has been estimated from the measured visual flux F_v and an assumed visual luminosity L_v. Solving (1) for $f\dot{M}$, and using these new quantities we obtain

$$(2) \qquad f\dot{M} \propto T_A V_a^2 \left(\frac{L_{8\mu} \; L_v}{F_{8\mu} \; F_v} \right)^{\frac{1}{2}}$$

Notice that $f\dot{M}$ depends strongly only on quantities that can be easily measured, and rather slowly on the least understood parameter, the assumed luminosity L_v. The quantity $f\dot{M}$ is quite well determined; an independent estimate of either f or $\dot{M}$ could be used to obtain the other.

The application of our calculations to the observations made by Buhl et al. (1975) is presented in table 2. The second and third columns list the estimates of D and W which we have extracted from the literature. The fourth and fifth columns give the values of T_A and V_a which are indicated by the SiO observations. Equation (2) has been used to derive $f\dot{M}$ listed in column six; the constant of proportionality in this equation was found from the most appropriate model in table 1 (although the gist of section IV is that this "constant" is indeed quite constant over a large range of parameters, we use the closest model to minimize as much as possible the deviations from equation 1). The estimates of $f\dot{M}$ for all but VY CMa have been corrected slightly for the fact that these stars appear to be close enough (much less than 500 pc) for their envelopes to be partly resolved. Column eight gives the minimum total mass loss rates $\dot{M}$, which were derived from the values of $f\dot{M}$ under the assumption that all of the cosmic abundance of silicon is in the form of SiO molecules ($[SiO]/[H_2] = 6 \times 10^{-5}$ by number, or $f = 1.32 \times 10^{-3}$).

These minimum mass loss rates are disturbingly low. If we assume that the infrared excesses in these stars is due to reradiation from dust heated by stellar photons, then from the momentum transfer of the stellar radiation to the dust, and from the asymptotic velocity of the material, one may estimate a mass loss rate. Goldreich and Scoville in this way obtained a typical mass loss rate of 3×10^{-5} $M_\odot$ yr^{-1} for the OH-IR stars. Gehrz and Woolf (1971), on the other hand, deduce mass loss rates of $1\text{-}2\times10^{-6}$ $M_\odot$ yr^{-1} from infrared observations of the first three stars in table 2.

In either case, it appears that SiO in these envelopes comprises only a small fraction (< 10%) of the available silicon, assuming cosmic abundances. These fractions are remarkably small, gives that model atmosphere computations (Vardya 1966 Tsuji,1973) indicate that most of the silicon is processed into SiO in the outer parts of the stellar atmosphere. It is very likely that grain formation becomes efficient in these envelopes, and thus that a large fraction of the SiO is processed into some form of silicate grains. It is surprising, however, that the grain formation and growth processes are so efficient that such small proportions of SiO are left in the outer parts of the envelope.

ACKNOWLEDGEMENTS

We thank Dr. Peter Goldreich for helpful discussions. Financial support for this research came from National Science Foundation grants AST 73-04677 A03 to the Owens Valley Radio Observatory and MPS-72 05045 A02 to the California Institute of Technology.

REFERENCES

Buhl, D., Snyder, L.E., Lovas, F.J., and Johnson, D.R. 1975, Ap. J (Letters), 201, L29.

Gehrz, R.D., and Woolf, N.J. 1971, Ap. J., 165, 285.

Gillett, F.C., Merrill, K.M., and Stein, W.A. 1971, Ap. J., 169, 83.

Goldreich, P.A., Scoville, N.Z. 1976, Ap. J., 205, 144.

Hedelund, J., and Lambert, D.L. 1972, Ap. J. (Letters), 11, 71.

Herbig, G.H. 1969, Mem. [8°] Soc. Roy. Sci. Liège.

Hyland, A.R., Becklin, E.E., Neugebauer, G., Wallerstein, G. 1969, Ap. J., 158, 619.

Hyland, A.R., Becklin, E.E., Frogel, J.A., and Neugebauer, G. 1972, Astron. and Astrophys., 16, 204.

Kwan, J. and Hill, F. 1977, Ap. J., in press.

Morris, M. 1975, Ap. J., 197, 603.

Reid, M.J., and Dickinson, D.F. 1976, Ap. J., 209, 505.

Tsuji, T. 1973, Astron. & Ap., 23, 411.

Vardya, M. S. 1966, M.M.R.A.S., 134, 347.

Wilson, W. J., Schwartz, P. R., Neugebauer, G., Harvey, P. M., and Becklin, E. E. 1972, Ap. J., 177, 523.

Zuckerman, B., Gilra, D. P., Turner, B. E., Morris, M., and Palmer, P. 1976, Ap. J. (Letters), 205, L15.

Zuckerman, B., Palmer, D., Morris, M., Turner, B. E., Gilra, D. P., Bowers, P. F., and Gilmore, W. 1977, Ap. J. (Letters), in press.

TABLE I

Calculated Peak Line Antenna Temperature (K)
For D=500 pc, T_*=2000K, $R_*=6\times10^{13}$cm

V_a (Km s^{-1})	ΔV (Km s^{-1})	W	$\dot{f}M$ ($10^{-10} M_\odot yr^{-1}$)	T_A 1→0	2→1	3→2	4→3
6	1	4	0.87	.070	.342	.435	.354
6	1	4	1.74	.128	.804	.906	.749
6	1	4	3.48	.254	1.964	1.978	1.396
6	1	4	5.80	.321	3.208	4.827	2.979
8	1	4	5.80	.217	1.668	1.953	1.579
10	0.59	4	1.45	.057	.233	.278	.209
10	0.59	4	2.90	.095	.448	.557	.447
10	0.59	4	5.80	.171	.912	1.109	.932
10	1	4	5.80	.151	.934	1.136	.975
17	1	2	4.93	.042	.188	.237	.183
17	1	2	9.86	.069	.391	.516	.429
17	1	2	19.72	.126	.895	1.212	1.066
17	1	4	4.93	.064	.270	.327	.249
17	1	4	9.86	.108	.528	.655	.529
17	1	8	4.93	.095	.379	.479	.367
17	1	8	9.86	.158	.717	.908	.750
17	1	8	19.72	.266	1.385	1.756	1.484
17	0.5	4	4.93	.070	.287	.331	.247
17	2.0	4	4.93	.057	.245	.315	.246
with collisions:							
10	0.59	4	5.80	.163	.923	1.02	.789

TABLE 2

Comparison With Observations

(1) Star	(2) D (pc)	(3) W	(4)[8] T_A (K)	(5)[9] V_a (Km s^{-1})	(6) fM ($M_\odot$/yr)	(7) M_{min} ($M_\odot$/yr)
R Cas	195[1]	0.60[5]	0.47	8.9	1.0×10^{-10}	7.7×10^{-8}
W Hya	100[1]	0.67[6]	0.30	6.8	1.5×10^{-11}	1.1×10^{-8}
R Leo	150[2]	0.86[5]	0.35	3.9	9.8×10^{-12}	7.4×10^{-9}
Vy Cma	400[3]	14.7[7]	0.32	36.7	9.2×10^{-10}	6.9×10^{-7}
	1500[4]	206[7]			3.8×10^{-9}	2.9×10^{-6}

Notes to Table 2:

1) luminosity distance from Wilson et al. (1972)

2) luminosity distance derived with same assumptions as in Wilson et al. (1972) and IR data of Gillett et al. (1971)

3) luminosity distance from Hyland et al. (1969)

4) suggested by Herbig (1969)

5) derived using IR data of Gillett et al. (1971)

6) derived using IR data of Gehrz and Woolf (1971)

7) derived using IR data of Hyland et al. (1972)

8) Buhl et al. (1975)

9) Reid and Dickinson (1976)

APPENDIX

A Model for the Excitation of the Microwave Lines

It is instructive to try to make a simplified, analytical model for the excitation of the microwave lines in SiO. In this appendix we describe the excitation of an idealized model of a diatomic molecule, which has only one rotational ladder of scalar levels. The levels will have the usual energy spacing, but the statistical weights are now all equal to unity. The transfer of population that occurs via the excited vibrational state in the real SiO molecule is here represented by an imposed upward transfer of population between levels J and J + 1 given by:

$$R_{J\to J+1} = (n_J - n_{J+1})\, B_v\, \mathcal{J}_v \quad . \tag{A1}$$

Where the n_J are the level populations, $\mathcal{J}_v$ is the profile averaged mean intensity at 8μ and B_v is an "effective" value for the Einstein B coefficient for the 8μ transitions in SiO. We have assumed B_v is constant for all the transitions, and an appropriate value for B_v is half the asymptotic value of the true B coefficient, as J becomes large. The half arises because in the real molecule ~ half of the excitations to the excited vibrational state result in spontaneous decays back into the original level.

We have also ignored the fact that in the real molecule the 8μ transitions shift population in steps $\Delta J = \pm 2$. This greatly simplifies the calculations, and does not overlook any essential feature of the excitation mechanism. As mentioned in § II the near decoupling of the odd and even J levels is unimportant in this situation.

The net downward transfer of population is via the microwave transitions:

$$R_{J\to J+1} = \beta_{J,J+1}\, A_{J,J+1}\, n_{J+1} \quad . \tag{A2}$$

Here $A_{J,J+1}$ is the Einstein A coefficient for the transition, and $\beta_{J,J+1}$ is the escape probability for the photon. Streaming velocities greatly exceed the local turbulent velocities in this problem, so that the escape probability is locally determined. It is given by (Castor, 1970)

$$\beta_{J,J+1} = \int_0^1 \left\{ \frac{1 - \exp[-\tau_{J,J+1}(\mu)]}{\tau_{J,J+1}(\mu)} \right\} d\mu \quad . \tag{A3}$$

$\tau_{J,J+1}(\mu)$ is the optical depth in the transition, along a ray making an angle $\theta = \arccos(\mu)$ to a radius vector. Note that the dependence of the variables on radius has not been explicitly included. Continuing:

$$\tau_{J,J+1}(\mu) = \frac{hcr}{4\pi V} \frac{B_r (n_J - n_{J+1})}{1 + \mu^2 \left(\frac{d\ \ell n\ V}{d\ \ell n\ r} - 1 \right)} \quad . \tag{A4}$$

Where B_r is the Einstein B coefficient for the rotational transitions, and all other symbols have their usual meaning. Since these lines are optically thick, we may substitute (A4) into (A3) and obtain

$$\beta_{J,J+1} = \frac{8\pi V}{3hcr\, B_r (n_J - n_{J+1})} \left(1 + \frac{1}{2} \frac{d\ \ell n\ V}{d\ \ell n\ r} \right) \quad . \tag{A5}$$

At large distances from the star the gradient of the streaming velocity is asymptotically zero. We now evaluate the right hand of (A2) to obtain:

$$R_{J\to J+1} = \frac{16\pi V(J+1)^3}{3r\,\lambda_{10}^3}\left(\frac{n_J}{n_J - n_{J+1}}\right) \quad . \tag{A6}$$

Where λ_{10} is the wavelength of the $J = 1 \to 0$ transition. If we define

$$\eta^2 = \frac{16\pi V}{3r\,\lambda_{10}^3\, B_\nu\, \mathcal{J}_\nu} \quad , \tag{A7}$$

then using equations (A1), (A6) and (A7) we can form a difference equation for the level populations:

$$(n_J - n_{J+1})^2 = \eta^2 (J+1)^3\, n_{J+1} \quad . \tag{A8}$$

This can be solved approximately, when η^2 is small compared to n_o, yielding

$$n_J \approx \left(\sqrt{n_o} - \frac{1}{5}\,\eta\, J^{5/2}\right)^2 \quad . \tag{A9}$$

We will also need to express n_o in terms of the total number density of the molecule, N:

$$n_o \approx 1.22\,\eta^{1/3}\, N^{5/6} \quad . \tag{A10}$$

To estimate the number of photons emitted by the cloud, η, we need to integrate equation (A6) over volume, since each net downward transition results in a photon escaping to infinity. It is easier to use (A7) together with (A8) and (A10) to obtain:

$$\eta_{J,J+1} = \int_0^{r_c} 4\pi r^2 \, dr \, B_\nu \, \ell_\nu \, \eta (J+1)^{3/2} \left(1.11 \, \eta^{1/6} \, N^{5/12} - 0.2 \, \eta (J+1)^{5/2}\right) \quad . \quad \text{(A11)}$$

Since we are interested only in low lying levels we will neglect the second term in the large brackets from now on. The integral is proportional to $r_c^{3/4}$ (where r_c is the outer radius of the line emitting region) and we choose r_c to be that radius at which the optically thick assumption fails:

$$r_c = \frac{4\pi V}{hc \, B_r \, N} \quad , \quad \text{(A12)}$$

where we have used (A4) and set $\tau_{01} = 1$ and $\mu = 0$. We now evaluate the flux in the line at a distance D from the cloud, assuming $D \gg r_c$, and obtain:

$$\mathcal{F}_{\nu_{J,J+1}} (\text{line center}) = 6.98 \times 10^{-2} \left(\frac{(hc)^{7/4} B_r^{3/4} B_\nu^{5/12}}{\lambda_{10}^{3}} \right) \left(\frac{\ell_{8\mu}^{5/12} S^{7/6}}{V^{7/3} D^2} \right) (J+1)^{3/2} \quad , \quad \text{(A13)}$$

where we have introduced some new quantities. S is the number of SiO molecules passing through the inner edge of the cloud per unit second, so that

$$N = \frac{S}{4\pi r^2 V} \quad . \quad \text{(A14)}$$

$\mathcal{L}_{8\mu}$ is the specific luminosity of the central star in 8μ photons, so that

$$J_\nu = \frac{\mathcal{L}_{8\mu}}{4\pi r^2} \quad . \tag{A15}$$

In evaluating the numerical constant on the right of equation (A12) we assumed that the line profile of an optically thick line is parabolic, so that the flux at line center seen by an observer at a large distance D is related to $\eta_{J,J+1}$ by:

$$\mathcal{F}_{\nu_{J,J+1}}(\text{line center}) = \frac{3}{8\pi} \frac{hc\,\eta_{J,J+1}}{VD^2} \quad . \tag{A16}$$

Equation (A12) exhibits the dependences of the flux on the parameters fairly well. If we look more closely at how the flux depends on the input parameters, we find that:

$$\mathcal{F}_\nu \propto \left(\frac{\mathcal{L}_{8\mu}^{1/2}\, S}{V^2}\right)\left(\frac{S^{1/6}}{\mathcal{L}_{8\mu}^{1/12}\, V^{1/3}}\right) \quad . \tag{A17a}$$

We see that the flux nearly varies as very simple powers of $\mathcal{L}_{8\mu}$, S and V. The dependences in the first bracket were motivated in § IV, in particular we note that at constant fractional level population, the optical depth in each line varies as SV^{-2}. In this regime photon trapping ensures that the excitation temperature is proportional to τ, and the gradual transfer of population to higher levels with increasing 8μ flux shows in the fact that the emission rate goes only as $\mathcal{L}_{8\mu}^{1/2}$. The second, slowly varying

factor, shows how $\mathcal{F}_\nu$ varies due to the fact that the number of levels which are significantly populated varies, slowly, with the input parameters.

In this appendix we have used $\mathcal{L}_{8\mu}$ ($\propto$ W), S ($\propto$ $\dot{fM}$) and $\mathcal{F}_\nu$ ($\propto T_A$) since the equations are simpler when expressed in terms of these quantities. We may rewrite (A17 a) to see:

$$T_A \propto \left(\frac{W^{1/2}\ \dot{fM}}{V^2}\right)\left(\frac{(\dot{fM})^{1/6}}{W^{1/12}\ V^{1/3}}\right). \qquad \text{(A17b)}$$

We note that in different situations the choice of cloud radius in (A12) may be inappropriate. It may occur that the 3°K isotropic background is important in the excitation, and so the cloud may terminate where the excitation temperatures fall to 3°K. Another possibility is that η^2 may become comparable to n_o, in which case (A9) loses its validity.

Finally, if the microwave transitions are optically thin throughout the envelope, instead of (A12) we would have:

$$\mathcal{F}_{\nu_{J,J+1}}(\text{line center}) = \frac{\sqrt{2}}{3\pi}(hc)^{3/2}\left(\frac{B_r B_v}{\lambda_{10}^3}\right)^{1/2}\frac{\mathcal{L}_{8\mu}^{1/2}\ S}{V^2\ D^2}(J+1)^3 \quad , \qquad \text{(A18)}$$

where the dependences on environmental parameters are nearly the same, but on the molecular constants very different.

FIGURE CAPTIONS

Fig. 1 Curves of excitation temperature (T_{ex}) and tangential optical depth (τ) of the J=2→1 transition as a function of R, the radial distance from the center of the star. Three curves are shown for each parameter, each corresponding to a different value of the mass loss rate of SiO molecules from the star, $\dot{f}M$. The 8μ flux is four times the direct stellar contribution in all cases.

Fig. 2 Curves of excitation temperature (T_{ex}) and tangential optical depth (τ) of the J=1→0 transition as a function of R, the radial distance from the center of the star. Three curves are shown for each parameter, each corresponding to a different value of W, the factor by which the 8μ flux exceeds the direct stellar contribution. The mass loss rate of SiO molecules is held constant at 9.86×10^{-10} $M_\odot$ yr^{-1} in all cases.

Fig. 3 Line profiles for the SiO J=1→0 transition from the model circumstellar envelope at a distance of 500 pc and having an asymptotic velocity, V_a, of 10 km s^{-1}. The different profiles result from different values of $\dot{f}M$, the mass loss rate of SiO, indicated in units of 10^{-10} $M_\odot$ yr^{-1}. The J=2→1 profiles are almost always parabolic and thus are not shown; the parameter X indicated for each profile gives the ratio of peak antenna temperatures for the 2→1 and 1→0 lines as measured by an ideal antenna.

Fig. 4 Same as for figure 3, but with V_a=6 km s^{-1}, and different values of $\dot{f}M$.

Fig. 5 Same as figure 3, but with V_a=17 km s^{-1}. The dotted curves are for $f\dot{M} = 9.86 \times 10^{-10}$ $M_\odot$ yr^{-1} and the solid ones for $f\dot{M} = 4.93 \times 10^{-10}$ $M_\odot$ yr^{-1}. The different curves result from different values of W, the factor by which the 8μ flux exceeds the direct stellar contribution.

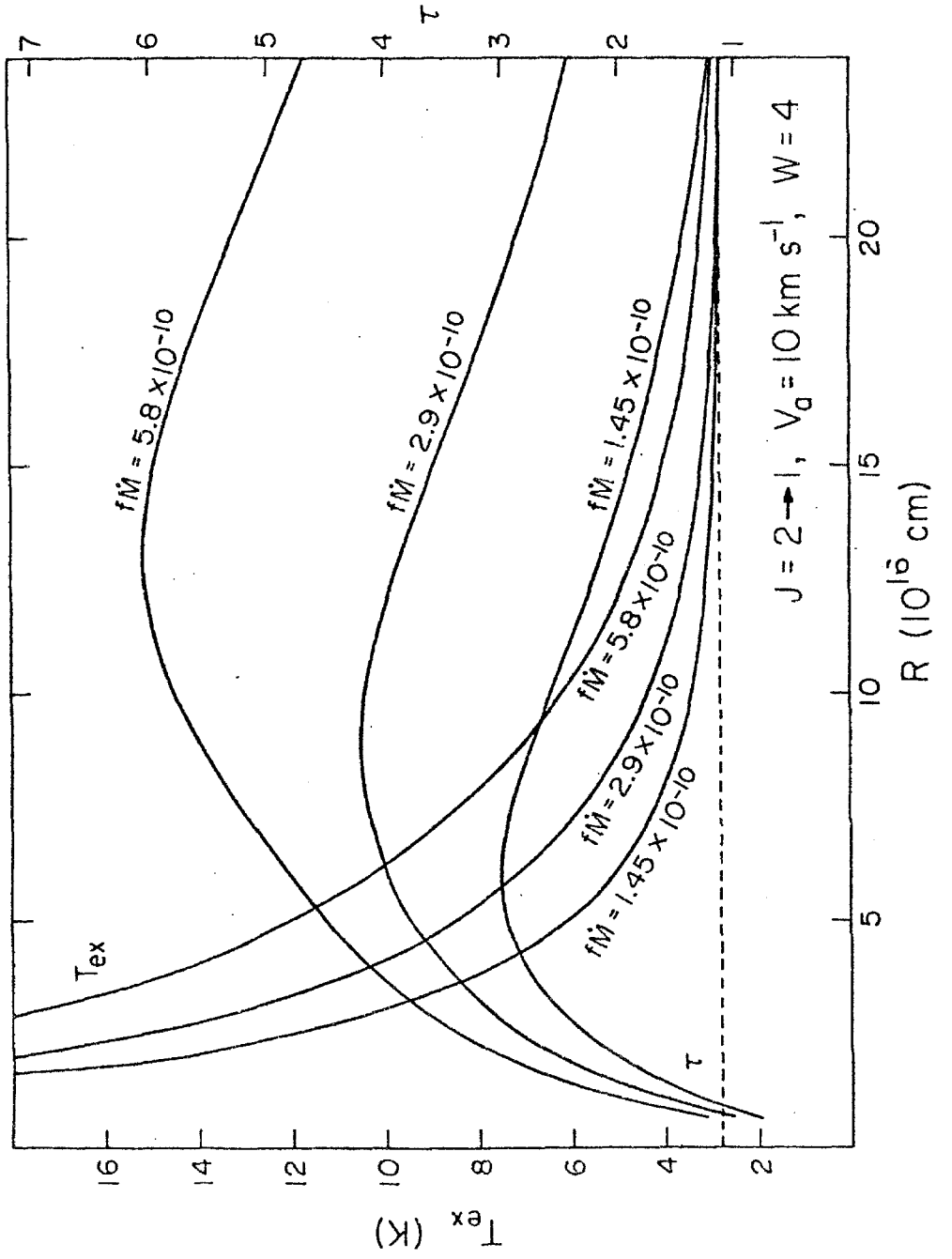
T_{ex} (K)
R (10^{16} cm)
τ
T_{ex}
τ
$\dot{fM}$ = 5.8 x 10-10
$\dot{fM}$ = 2.9 x 10-10
$\dot{fM}$ = 1.45 x 10-10
$\dot{fM}$ = 5.8x10-10
$\dot{fM}$ = 2.9x10-10
$\dot{fM}$ = 1.45 x 10-10
J = 2→1, V_a = 10 km s^{-1}, W = 4

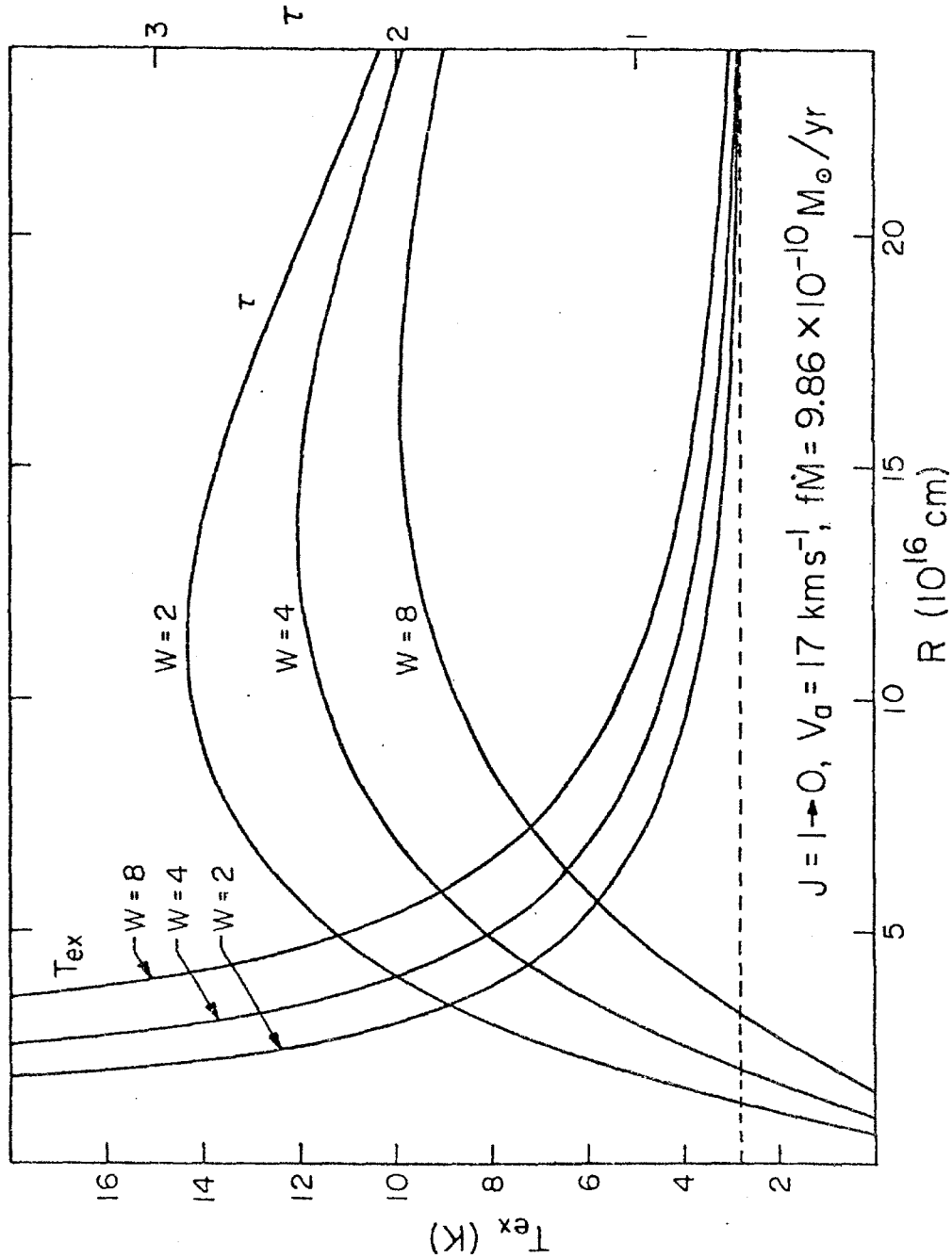
T_{ex} (K)
R (10^{16} cm)
$J = 1 \rightarrow 0$, $V_a = 17$ km s^{-1}, $\dot{fM} = 9.86 \times 10^{-10} M_\odot$/yr
W = 2
W = 4
W = 8
τ
τ
W = 8
W = 4
W = 2
T_{ex}

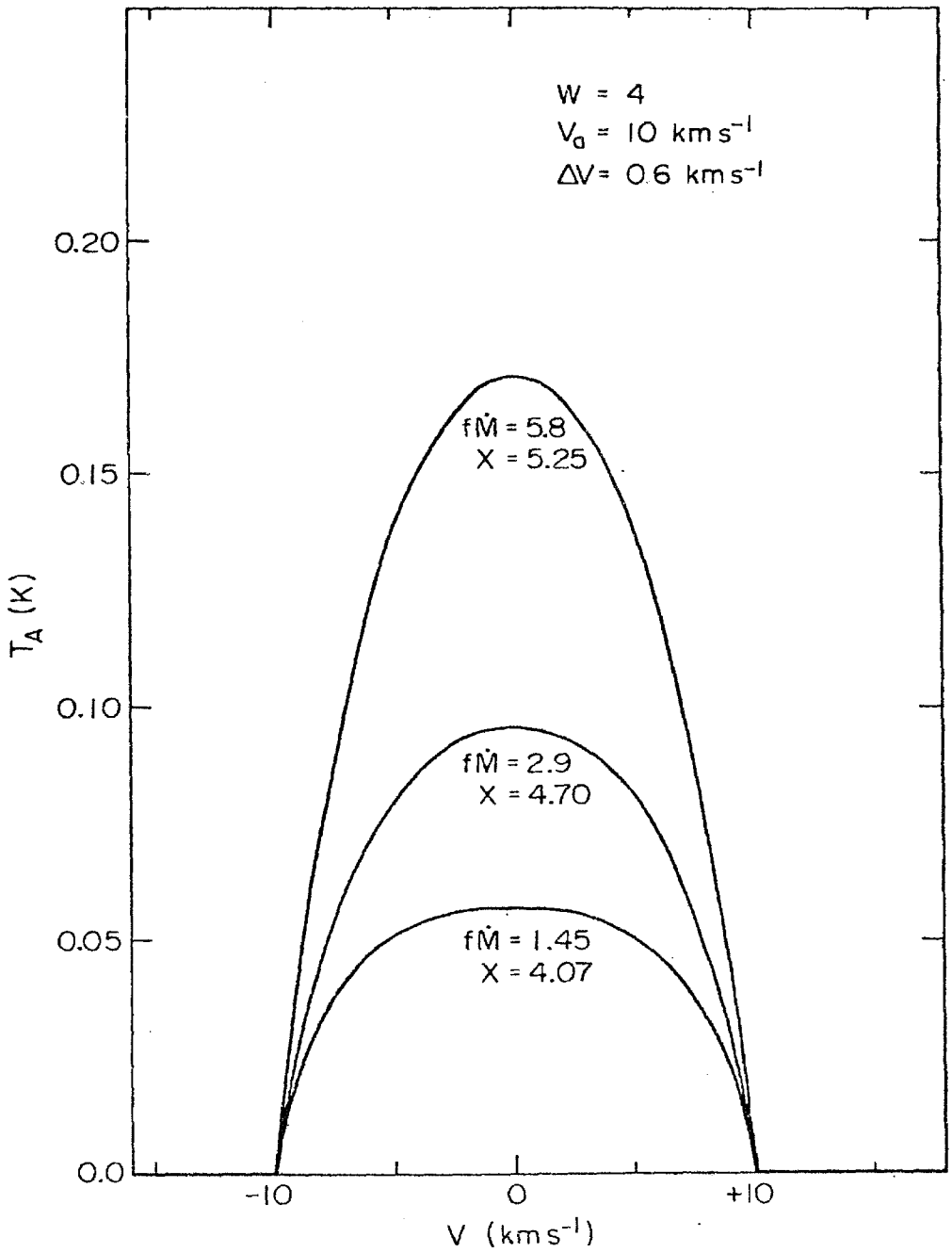
W = 4
V_a = 10 km s^{-1}
ΔV = 0.6 km s^{-1}
fṀ = 5.8
X = 5.25
fṀ = 2.9
X = 4.70
fṀ = 1.45
X = 4.07
0.20
0.15
0.10
0.05
0.0
T_A (K)
-10
0
+10
V (km s^{-1})

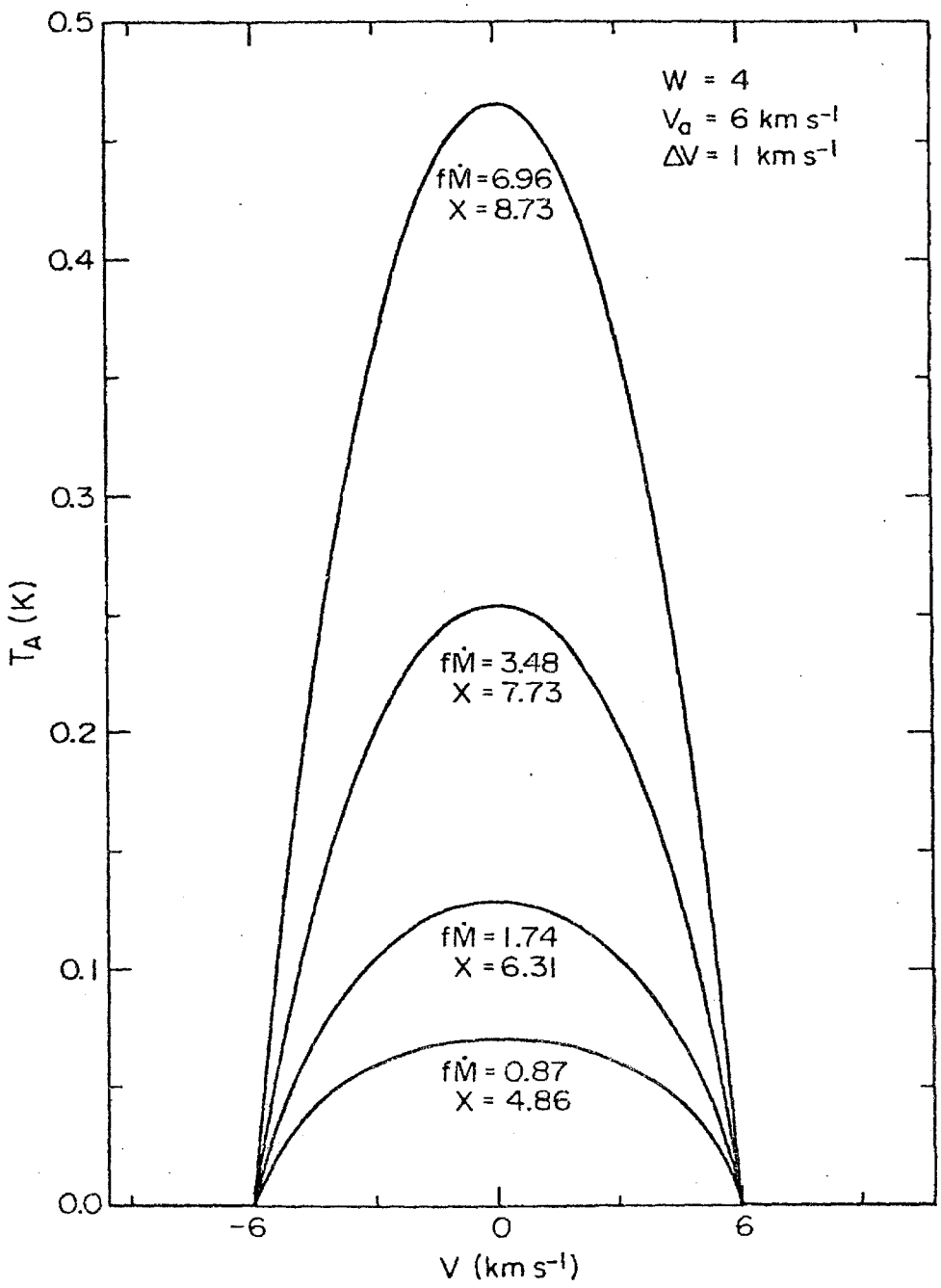
W = 4
V_a = 6 km s^{-1}
ΔV = 1 km s^{-1}
fṀ = 6.96
X = 8.73
fṀ = 3.48
X = 7.73
fṀ = 1.74
X = 6.31
fṀ = 0.87
X = 4.86
T_A (K)
0.0
0.1
0.2
0.3
0.4
0.5
-6
0
6
V (km s^{-1})

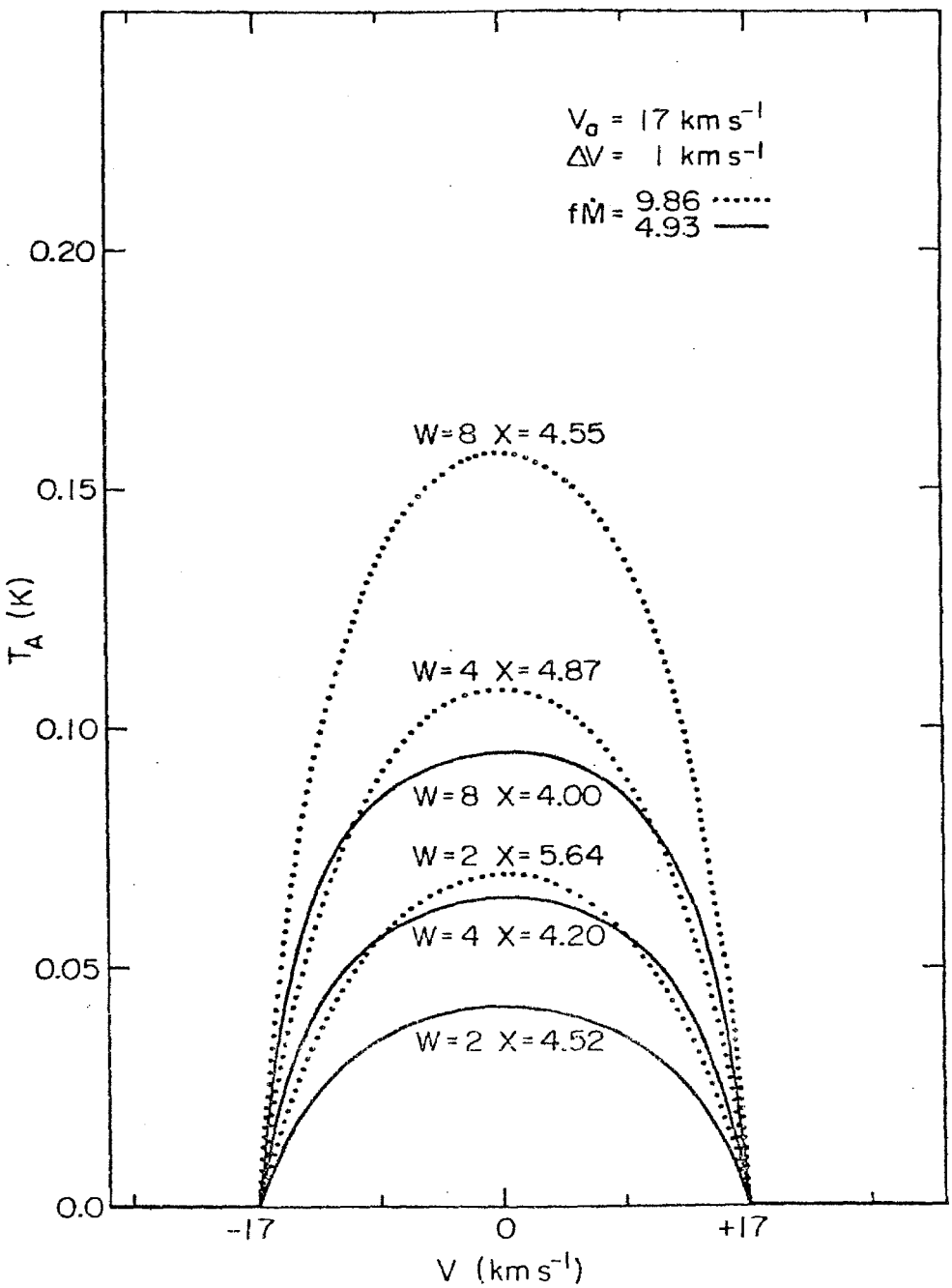
V_a = 17 km s^{-1}
ΔV = 1 km s^{-1}
$f\dot{M}$ = 9.86 ·····
4.93 ——
W=8 X=4.55
W=4 X=4.87
W=8 X=4.00
W=2 X=5.64
W=4 X=4.20
W=2 X=4.52
0.20
0.15
0.10
0.05
0.0
T_A (K)
-17
0
+17
V (km s^{-1})

PAPER 3

MOLECULAR EMISSION FROM EXPANDING ENVELOPES AROUND EVOLVED STARS

II. MASER EMISSION LINES*

CHARLES ALCOCK

Division of Physics, Mathematics and Astronomy

California Institute of Technology, Pasadena, California 91125

and

MARK MORRIS

Owens Valley Radio Observatory

California Institute of Technology, Pasadena, California 91125

*Supported in part by the National Science Foundation [AST76-80801], [AST73-04677 A03] and [MPS72-05045 A02].

ABSTRACT

We have investigated the excitation of the microwave lines in the excited vibrational states of the SiO molecules in the expanding envelopes of cool Mira-type stars. The excited vibrational states are populated principally by the absorption of 8μ photons. The inversions occur when the gas temperature exceeds the excitation temperature of the vibrational levels, and upward vibrational collisions selectively populate higher rotational levels. The masers are all saturated. We discuss the line profiles, and show how the profile is determined by the velocity gradient and the ambient radiation field.

The SiO abundance required for the masers is large. We discuss this in the light of our earlier calculation that the abundance is low in the outer envelope, and argue that grain formation is an efficient process.

Key Words: masers --- molecules, circumstellar radiative transfer

I. INTRODUCTION

In an earlier paper (Morris and Alcock 1977, hereafter referred to as Paper I) we analysed the excitation of the non-maser emission from SiO molecules in oxygen-rich stellar envelopes. We showed that the rotational transitions in the ground vibrational ladder were very efficiently excited by the absorbtion of 8μ photons. Using this calculation, we were able to estimate the number of SiO molecules in the circumstellar envelopes for which observations of v = 0 rotational lines exist. This may be used, together with independent estimates of the mass loss rates and the molecular abundances, to estimate the efficiency of grain formation in these envelopes.

In this paper we look at the excitation of the masers in the rotational lines in the first and second excited vibrational states of SiO. We also compute line shapes for our models (as we did in Paper I) and, because there exists some confusion in the literature about maser line shapes, discuss in a fairly general way these lines are formed.

Geballe and Townes (1974) proposed radiative pump mechanisms that depend on chance coincidences between various lines in the SiO spectrum. Their model is not able to explain the richness of the SiO maser spectrum, and in particular fails to explain the J = 1 → 0 line in the second excited vibrational state. Kwan and Scoville (1974) pointed out the importance of radiative trapping in the excitation of vibrationally excited SiO. Their paper clearly describes many of the key features of any SiO excitation mechanism. They did not discuss the maser in the second excited vibrational state, and unfortunately their numerical calculations suffer from an incorrect value of the $\Delta v = 2$ transition rate. They did not discuss maser line

shapes. Deguchi and Iguchi (1976) discussed radiative pumping of the SiO maser, but did not adequately describe the pump cycles their numerical computations produce. They did not take saturation of the masers into account, even though Kwan and Scoville had shown how saturation in one transition could lead to an inversion in the next higher transition. We will show below that their model would produce the wrong line shapes.

Olnon (1977) discussed the line shape for masers formed in expanding envelopes, but (as we show in §III) his discussion is incorrect. The correct description of the shape of the 1612 MHz OH maser lines was given by Elitzur et al. (1976) and Kwok et al. (1975), and we will generalize this discussion to cover masers formed in all regions of the envelope.

In the next section we briefly summarize the key observations that this paper discusses. In §III we show how the maser emission line is formed, and discuss its shape carefully. In §IV we describe in some detail the numerical calculations of the excitation of the masers in SiO and present the results. We compute line shapes for these models. In §V the pump cycles for each of the masers is discussed carefully, and the results are compared with the observations. In §VI we discuss the implications of these results.

II. THE OBSERVATIONS

The observations of the objects around which SiO masers have been detected has been extensively reviewed by Olnon (1977). We present only those features we are concerned with here. The masers occur around cool giant and supergiant stars (typically long period variable stars) which are believed to be losing mass (see e.g., Gehrz and Woolf 1971, and references therein). The transitions that have been detected are v = 1,

$J = 1 \rightarrow 0$ (Thaddeus et al. 1974, Snyder and Buhl 1975); $v = 1$, $J = 2 \rightarrow 1$ (Snyder and Buhl 1974, Kaifu et al. 1975); $v = 1$, $J = 3 \rightarrow 2$ (Davis et al. 1974); and $v = 2$, $J = 1 \rightarrow 0$ (Buhl et al. 1974). There have been unsuccessful searches for masers in the transitions $v = 0$, $J = 1 \rightarrow 0$; and $v = 3$, $J = 1 \rightarrow 0$ (Buhl et al. 1974). "Thermal" emission in the $v = 0$, $J = 2 \rightarrow 1$ line has been detected (Buhl et al. 1975); we discussed the excitation of this line in Paper I.

The lines are either double peaked, with a typical separation of ~ 8 km s^{-1}, or singly peaked. Where 1612 MHz or 1665/1667 MHz OH masers coexist, the SiO emission falls midway between the OH emission peaks. Some of the stars are also 22.2 gHz H_2O maser sources: the H_2O maser lines are generally single peaked at a velocity between the SiO peaks (if the SiO line is double peaked) or nearly coincident with SiO peak (if the SiO line is singly peaked). In general the structure of the lines in the different transitions is similar for any given star. Not all of the transitions are detected in all of the stars.

The lines are observed to vary in phase with the light curves of the stars, and two objects have been reported to vary in a few days (Spencer and Schwartz 1975, Balister et al. 1977).

III. THE LINE SHAPE

The previous work mentioned above has largely concerned the mechanisms that leads to population inversion in the various microwave lines for which non-thermal emission has been observed. Of these only Elitzur et al. (1976) and Kwok et al. (1975) discussed the shape of the microwave line that would be observed at infinity for their model of the 1612 MHz OH masers. Olnon (1977) attempted a more

general discussion of the determination of maser line shapes around cool giant and supergiant stars. He used this discussion to analyse the lines of OH, H_2O and SiO and infer details about the expanding envelopes of these stars. We will show below that his discussion is incorrect. We present here a fairly detailed description of how the velocity field, optical depth and source function of an inverted transition produce characteristic emission line shapes. Using a simplified model of a maser in an expanding envelope, we demonstrate how it is possible to approximately infer the location of the maser and the logarithmic gradient in the vicinity of the maser from the observed line. This inverse procedure is not unique, and is somewhat sensitive to the assumptions made, but provides new information about these envelopes.

We assume throughout this section that the envelope around the star is spherically symmetric, and that the material is accelerated from the surface so that its velocity is a monotonically increasing function of radius. The escape probability formalism is not used in this section, but the notation is similar to that used by Castor (1970) where a fuller description of the input quantities is presented. The interested reader may wish to refer to this earlier paper.

The source function in a given transition at a radius r is:

$$S(r) = \frac{2h\nu_0^3}{c^2} \frac{1}{n_\ell/n_u - 1} \quad , \qquad (1)$$

where ν_0 is the frequency of the transition, n_ℓ and n_u are the fractional sublevel populations of the lower and upper levels, respectively. All unspecified symbols have their usual meanings. The optical depth in the line of radius r and along a ray at angle $\theta = \arccos(\mu)$ to a radius is

given by:

$$\tau(r,\mu) = \frac{-\tau_0(r)}{1 + \sigma(r)\,\mu^2} \tag{2}$$

where

$$\tau_0(r) = \frac{\pi e^2}{mc} (gf)_{\ell,u} \frac{rc}{\nu_0 V(r)} (n_\ell - n_u) \tag{3}$$

and

$$\sigma(r) = \frac{d\ ln\ V}{d\ ln\ r} - 1 \ , \tag{4}$$

where $V(r)$ is the expansion velocity at radius r. In the integrals needed to evaluate the flux in the line at a given frequency ν, we have to integrate over a surface of constant Doppler shift to a distant observer (see Fig. 1). This specifies the value of μ:

$$\mu = \frac{c}{V(r)} \left(\frac{\nu - \nu_0}{\nu_0} \right) \ . \tag{5}$$

The line will have a local width due to thermal motions and microturbulence. We will assume that this local velocity width is small compared to the streaming velocities. If the normalized local profile is $\phi(\nu - \nu_0)$, we define

$$y(r,\nu) = \int_{-\infty}^{\nu_*} \phi(\nu - \nu_0)\ d\nu \tag{6a}$$

with

$$\nu_* = (\nu - \nu_0) \left\{ 1 - \frac{1}{\mu r} (r_c^2 - [1 - \mu^2]\ r^2)^{1/2} \right\} \ . \tag{6b}$$

With these quantities we may evaluate the ratio of the flux F_ν in the line to the continuum flux F_c, when these are measured by a distant observer:

$$\frac{F_\nu - F_c}{F_c} = P_1 + P_2 + P_3 + P_4 \tag{7}$$

$$P_1 = \int_{r_m(\nu)}^{\infty} \frac{2r\,dr}{r_c^2} \frac{S(r)}{I_c} (1 + \sigma\mu^2) \left(1 - \exp\left\{\frac{-\tau_0}{1 + \sigma\mu^2}\right\}\right) \qquad (8a)$$

$$P_2 = \int_{r_m(\nu)}^{r_p(\nu)} \frac{2r\,dr}{r_c^2} \left(\exp\left\{\frac{-\tau_0 y}{1 + \sigma\mu^2}\right\} - 1\right) \qquad (8b)$$

$$P_3 = \int_{r_m(\nu)}^{r_p(\nu)} \frac{2r\,dr}{r_c^2} \frac{S(r)}{I_c} (1 + \sigma\mu^2) \left(\exp\left\{\frac{-\tau_0}{1 + \sigma\mu^2}\right\} - \exp\left\{\frac{-\tau_0 y}{1 + \sigma\mu^2}\right\}\right) \qquad (8c)$$

$$P_4 = \int_{r_p(\nu)}^{\infty} \frac{2r\,dr}{r_c^2} \frac{I_{BB}}{I_c} (1 + \sigma\mu^2) \left(\exp\left\{\frac{-\tau_0}{1 + \sigma\mu^2}\right\} - 1\right) . \qquad (8d)$$

In these equations I_c is the specific intensity in the continuum at the surface of the star; it is usually set equal to the Planck function at the stellar surface temperature. I_{BB} is the specific intensity of the 3 ^{o}K background radiation, and r_c is the radius of the central star. The two frequency dependent radii $r_m(\nu)$ and $r_p(\nu)$ are shown in Figure 1. They are defined by

$$\frac{V\left(r_m(\nu)\right)}{c} = \left|\frac{\nu - \nu_0}{\nu_0}\right| \qquad (9a)$$

$$r_p(\nu) = r_c\left(1 - \mu^2\left(r_p(\nu)\right)\right)^{-1/2} \qquad (9b)$$

The expression for the flux in the line has been broken down into these four pieces because they represent physically distinct parts of the process. P_1 evaluates the amplification by the maser of its own spontaneous emission, under the assumption that the central star is transparent. It is symmetric

about the line centre, and depending on the location of the population inversion may have a single peak at ν_0 or two peaks at $\sim\nu_0(1 \pm V(\infty)/c)$. In those situations where the maser inversion occurs, a singificant distance from the star, P_1 is usually the dominant component.

P_2 evaluates the amplification by the maser of the stellar continuum. Because of this, only frequencies blueshifted from ν_0 are observed. It generally peaks at a frequency significantly blueshifted from ν_0. In masers where the population inversion is fairly close to the star this component usually dominates. The ratio of the peak intensity in P_1 to the peak intensity in P_2 is approximately given by

$$\mathrm{Max}\left\{\frac{P_1}{P_2}\right\} \approx \frac{S(r)}{I_c} \frac{d\ \ell n\ V}{d\ \ell n\ r} \left(\frac{r}{r_c}\right)^2 \quad , \tag{10}$$

where the right-hand side should be evaluated at the radius where $-\tau_0(d\ \ell n\ r/d\ \ell n\ V)$ is maximized. Using equation (1) and expressing I_c in terms of the stellar surface temperature T_c (in the Rayleigh-Jeans approximation since $kT_c \gg h\nu_0$ for all microwave lines):

$$\mathrm{Max}\left\{\frac{P_1}{P_2}\right\} \approx \left(\frac{n_\ell}{n_u} - 1\right)^{-1} \frac{h\nu_0}{kT_c} \frac{d\ \ell n\ V}{d\ \ell n\ r} \left(\frac{r}{r_c}\right)^2 \quad . \tag{11}$$

P_3 is a correction to P_1 which subtracts out that portion of P_1 that is absorbed by the central star. P_4 evaluates the amplification of the 3 ^oK background by the maser. This is not often likely to be important, with one possible exception. The model for the 1612 MHz OH maser published by Elitzur et al. (1976) would have P_4 about 20 percent of P_1. If the inversion were more pronounced, P_4 might dominate.

The apparent complexity of equations (8) disguise their principal features. To demonstrate these we will construct a simplified three

parameter set of models of a "maser" around a "star" that is losing mass. No discussion of the origin of this "maser" will be made, but instead the run of velocity, source function and optical depth with radius will be specified a priori, and then simplified versions of the integrals in equations (8) will be evaluated. We will set $r_c = 1$ and $I_c = 1$ since they scale out of the equations. The velocity field we will use is:

$$V(r) = \tanh\left(\frac{r - 1}{r_E}\right) \quad , \tag{12}$$

where r_E is a parameter that determines how close to the star the acceleration occurs. In Figure 2 we plot V and $d\ \ell n\ V / d\ \ell n\ r$ for the various r_E used. On this same figure we show the (appropriately scaled) velocity field determined by Goldreich and Scoville (1976). The optical depth of this "maser" will have the radial dependence:

$$\tau_0(r) = -\tau_M \exp\left\{-\left(\frac{r - r_M}{r_E}\right)^2\right\} \quad , \tag{13}$$

where r_M is a parameter that locates the "inversion" and τ_M parameterizes its strength. In these models we will take $S(r) = -1$, a simplification that is not strictly consistent with the assumed variation of the optical depth. However, in most situations the variation of $S(r)$ is much slower than variation of the exponentials in the integrands, so this assumption does not qualitatively change the results.

The two integrals we calculate are:

$$P_A = -\int_{r_m(\nu)}^{\infty} 2r\ dr(1 + \sigma\mu^2)\left(1 - \exp\left\{\frac{-\tau_0}{1 + \sigma\mu^2}\right\}\right) \tag{14a}$$

$$P_B = \int_{r_m(\nu)}^{r_p(\nu)} 2r\, dr \left(\exp\left\{ \frac{-\tau_0}{1 + \sigma\mu^2} \right\} - 1 \right) \quad . \tag{14b}$$

P_A is precisely P_1 for the simplified case presented here. In the limit that the Doppler width of the line may be neglected, the function y defined in equation (6) becomes a step function and then $P_B = P_2$. As mentioned before, P_3 is merely a correction factor to P_1, and of course in this situation P_4 is just P_1 multiplied by an appropriate constant.

In Figures 3, 4 and 5 we have plotted P_A and P_B for a representative set of the parameters. These illustrate the principal features of the line formation process. In Figures 3a and 3b the effects of moving the "acceleration region" further away from the star are seen. In the case where $r_E = 0.5$, most of the acceleration occurs close to the star. The logarithmic gradient (and hence σ) is large in the vicinity of the maser, and the greatest optical gains (see eq. [2]) are along rays perpendicular to radii. Because of this, most of the amplification of spontaneous emission occurs in directions nearly perpendicular to radii, and P_A peaks strongly about the zero of relative velocity. As the acceleration region moves futher away from the star, the logarithmic gradient in the vicinity of the inversion approaches zero (see Fig. 2) and the amplification becomes predominantly radial. In the most extreme case shown in Figure 3a the line peaks very close to the asymptotic radial velocity and there is a deep minimum at the stellar velocity. The situation for P_B (see Fig. 3b) is quite different, especially when the acceleration occurs very close to the star. This is because only material directly in front of the star (see Fig. 1) can contribute. There is always a minimum at the stellar velocity, and a peak in the emission line which becomes more intense, narrower and toward larger radial velocities, as the

acceleration region moves futher from the star.

In Figures 4a and 4b the optical depth of the maser is varied. This has only a small effect on P_B, because the geometrical limitation on the integrand holds $(1 + \sigma\mu^2)$ to a narrow range of values. However, since this quantity in the integrand of P_A can vary between $1 + \sigma$ and 1, the exponential term varies considerably. As the magnitude of τ_0 increases, the contrast due to the $(1 + \sigma\mu^2)$ term in the exponential becomes more pronounced, and amplification in nearby radial directions becomes dominant. This shows in the gradual trend of the line profile from a broad, almost square topped line to a line with a wide minimum and a narrow peak at high radial velocities.

In Figures 5a and 5b the dependence of the line shape on the location of the inversion is shown, ranging from the stellar surface to beyond most of the acceleration. All of the effects seen here are due to the contrast in $\tau_0/(1 + \sigma\mu^2)$. When the matter is being accelerated strongly, $\sigma > 0$ and the greatest optical gain is perpendicular to a radius. Far from the star $\sigma \approx -1$, and amplification in the radial direction is extremely pronounced. It is this latter situation that occurs in the model for the 1612 MHz OH masers constricted by Elitzur et al. (1976).

Most of the features discussed above were overlooked by Olnon (1977). In particular he missed the importance of knowing which source of radiation is being amplified, and was completely mistaken about the significance of saturation on the maser line shapes. The optical depth always enters the line integrals in an exponential, whereas the physical path length (which he appears to confuse with optical depth) only enters linearly if the maser is saturated. The dominant effect of saturation is to reduce the inversion. We will not discuss his interpretation of maser line shapes any further.

The correct nature of the double peaked lines characteristic of both mainline and 1612 MHz OH masers was appreciated by earlier authors (Elitzur et al. (1976), and references therein) but the detailed structure of the lines was not discussed.

IV. THE NUMERICAL CALCULATIONS

We describe here the equations of statistical equilibrium used and the method of solution employed in our numerical modelling of the SiO masers. In all of the calculations we have used the escape probability formalism developed by Sobolev (1960) and extended by Castor (1970) and Lucy (1971). The validity of this approach requires that the local line width (due to thermal motions, microturbulence, etc.) be small compared to the streaming velocities: this allows an approximate local solution to the radiative transfer. We use the formalism as presented by Castor, and only quote his results here.

The profile averaged mean intensity in a given line at radius r is given by:

$$\bar{J}(r) = (1 - \beta)\, S(r) + \beta_c (I_c - I_{BB}) + \beta\, I_{BB} \quad , \tag{15}$$

where β is the escape probability for the photon, and β_c is the probability that an escaping photon will strike the central star. We have included the dependence on the isotropic background radiation because in this way we can model the enhanced emission of 8μ photons due to the radiation from dust. A lunar occultation measurement (Zappala et al. 1974) of IRC + 10011 indicated that the dust shell had an inner radius $\geq 5 \times 10^{14}$ cm. It will turn out that the interesting effects in SiO occur closer to the star than this, and consequently we can model the dust re-emission by setting I_{BB} equal to

a Planck function at 500 °K when we evaluate $\bar{\beta}(r)$ for a $\Delta v = 1$ transition.

The expressions for β and β_c we take from Castor:

$$\beta = \int_0^1 d\mu \left\{\frac{\tau_0}{1 + \sigma\mu^2}\right\}^{-1} \left(1 - \exp\left\{\frac{-\tau_0}{1 + \sigma\mu^2}\right\}\right) \tag{16a}$$

$$\beta_c = \frac{1}{2} \int_{(1-r_c^2/r^2)^{1/2}}^1 d\mu \left\{\frac{\tau_0}{1 + \sigma\mu^2}\right\}^{-1} \left(1 - \exp\left\{\frac{-\tau_0}{1 + \sigma\mu^2}\right\}\right) . \tag{16b}$$

Using equation (15) to evaluate the mean intensity, we can write the equations of statistical equilibrium in the form:

$$\frac{dn_k}{dt} = \sum_{j>k} \left\{B_{jk}\, \bar{\beta}_{jk}(n_j - n_k) + A_{jk}\, n_j + C_{jk}(n_j - n_k \exp[-h\nu_{jk}/kT])\right\}$$
$$+ \sum_{i<k} \left\{B_{ki}\, \bar{\beta}_{ki}(n_i - n_k) - A_{ki}\, n_k - C_{ki}(n_k - n_i \exp[-h\nu_{ki}/kT])\right\} . \tag{17}$$

In these equations $E_i > E_j$ if $j > i$, and $h\nu_{ij} = E_i - E_j$. B_{ij} and A_{ij} are the Einstein coefficients for the transitions, where

$$B_{ij} = \frac{32\pi^4\mu^2}{3h^2c} \frac{J_m}{2J_m + 1} R_{v_i v_j} \tag{18a}$$

$$A_{ij} = \frac{2h\nu_{ij}^3}{c^2} B_{ij} . \tag{18b}$$

In equation (18a) J_m is the larger of J_i and J_j, the two rotational quantum numbers; μ is the dipole moment of the molecule. $R_{vv'}$ is the line strength, equal to unity when the two vibrational quantum numbers are equal, but < 1 when $v \neq v'$. In this calculation we use $\mu = 3.0885$ Debye, $R_{10} =$ 9.2E-4, $R_{21} =$ 1.79E-3, $R_{32} =$ 2.6E-3, $R_{20} =$ 2.39E-6, $R_{31} =$ 7.18E-6 and $R_{30} =$ 8.58E-9. Kwan and Scoville (1974) assumed $R_{10} = R_{21} =$ 1.0E-3 and $R_{20} =$ 2.0E-4; the fact that R_{20} is in fact so much smaller significantly weakens

their model.

The dipole moment is taken from Raymonda et al. (1970). It was measured in a molecular beam resonance spectrometer, in which a collimated beam of SiO molecules was passed through an electric field of ~875 V cm^{-1}. The electric field removes the degeneracy of the magnetic sublevels. The $|\Delta m_J| = 1$ transitions in the J = 1 levels occur at ~13 MHz, and these were measured. In this way, the dipole moment was measured to a precision of about 1 part in 10^4, for each of the lowest four vibrational levels. Combining these data with the known spectroscopic constants (Herzberg 1950) they measured a dipole moment derivative $d\mu/dr = 2.5 \pm 0.5$ Debye $\mathring{A}^{-1}$.

Hedelund and Lambert (1972) used these data to compute the line strengths given above. They computed wavefunctions for the vibrational states using a Morse potential, and evaluated the matrix elements for the transitions in two ways: (i) making a linear fit to the dipole moment and (ii) fitting a theoretical curve that had been derived for CO. The two answers agreed to within the errors due to the data. The authors claim 5 percent and 25 percent accuracies in their computed rates for $\Delta v = \pm 1$ and $\Delta v = \pm 2$ transitions, respectively. These errors are smaller than the errors due to the data. We think that the rates for $\Delta v = \pm 1$ or ± 2 transitions are certainly good to a factor of two, and probably 50 percent. In any event, R_{20} is considerably less than 2×10^{-4}, the value Kwan and Scoville (1974) assumed.

There is an observational argument in favour of a low R_{20}. Cudaback et al. (1971) observed the $v = 2 \rightarrow 0$ absorption band in the spectrum of α Orionis, with an instrumental resolution of 2 cm^{-1}. It is clear from the profile that the band head is at most weakly saturated. Hedelund and Lambert (1972) calculated equivalent widths at the band head using a simple model atmosphere and the SiO abundance computed by Tsuji (1973). They found that

the band head was weakly saturated. If R_{20} was significantly larger, the band would saturate.

We found that collisions, in particular collisions among the rotational levels of the ground vibrational state, and between the ground and first excited vibrational state, were very important. There is no good theory of collisions between H_2 and SiO molecules, so the collisions were treated approximately in the form described below. We tried several different models for the collisions. It turns out that the results are sensitive only to the ratios between the $\Delta v = 0$, and $\Delta v = 1$ collision rates and the corresponding radiative rates. The results are mercifully insensitive to the precise form adopted for the collision terms. The results presented in this paper *are for the following choice of* C_{ij}:

$$C_{ij} = \frac{N_{H_2} q v_t Z_{v_i v_j}}{1 + |J_i - J_j|} , \tag{19}$$

where N_{H_2} is the number density of H_2 molecules, and v_t is the mean thermal relative velocity of the H_2 and SiO molecules. If $v_i = v_j$, then $Z_{v_i v_j} = 1$. When $v_i \neq v_j$ we use a refinement of the Landau-Teller theory of quasi-adiabatic collisions described by Zel'dovich and Raizer (1966):

$$Z^{-1}_{v_i v_j} = \pi^2 \left(\frac{3}{2\pi}\right)^{1/2} \left(\frac{h\nu_{ij}}{\epsilon_0}\right)^2 \left(\frac{kT}{\epsilon_0}\right)^{1/6} \exp\left\{-\frac{h\nu_{ij}}{2kT} - \frac{\epsilon_1}{kT} + \frac{3}{2}\left(\frac{\epsilon_0}{kT}\right)^{1/3}\right\} \tag{20a}$$

with

$$\epsilon_0 = 16\pi^4 a^2 \nu_{ij}^2 \left(\frac{m_{H_2} m_{SiO}}{m_{H_2} + m_{SiO}}\right) . \tag{20b}$$

There are two parameters which describe the van der Waals interaction of SiO and H_2 molecules. The depth of the potential well due to van der Waals

attraction is given by ϵ_1, and we adopt $\epsilon_1 = 0.3$ eV. The range of the van der Waals force is given by a, and we adopt $a = 2\text{Å}$. The cross section σ we take to be 10^{-15} cm^2. The equations (17) are solved numerically using Newton's method. The convergence criterion employed was that $\Delta\mathcal{J}/\mathcal{J} < 10^{-2}$ for all of the transitions; this turns out to be a more stringent requirement than $\Delta n/n < 10^{-4}$, which is more commonly used. It is this condition that gives us some confidence that the line profile we compute is accurate to a few percent. For a given model the equations are solved at many radii; the source function and optical depth are stored for each transition we want at each radius. The line profiles are then calculated using equations (8) and a smooth interpolation on the tables of $S(r)$ and $\tau_0(r)$.

In these calculations we included 12 rotational levels in the v = 0 and v = 1 ladders, and 8 rotational levels in the v = 2 and v = 3 ladders. Close to the star, both collisions among the rotational levels and the 8μ excitation mechanism described in Paper I very efficiently distribute the molecules over many rotational levels in the ground vibrational state. It is important to estimate what fraction of the population exists in levels with J > 12. We did this by solving the balance equations at a few radii with 30 rotational levels in each of the v = 0 and v = 1 ladders, and thereby making a table which gave the fraction of the population in the high rotational levels for various values of the mean decay of the sublevel populations with J in the levels J = 9, 10, 11 and 12. We interpolated on this table to estimate the fraction of population in levels J > 12 in the computations presented here. For the two models we describe, ~ 1/2 of the population is pumped into these higher levels in the region where the masers operate. We used a velocity field of the form given by equation (12). Other models have been constructed, but no new features arose in those

calculations. We constructed models with and without the increased emission of 8μ photons due to dust re-emission; the models we describe in detail include the dust re-emission, but some of the other models are discussed in §V. We explored the dependence of the sublevel populations at two particular radii on the parameters σ, V and T_{gas}; these calculations are also discussed in the next section.

The input parameters that the two models we describe have in common are: stellar surface temperature, $T_c = 2000\ ^{o}K$; stellar radius, $r_c = 5.8 \times 10^{13}$ cm; mass loss rate, $\dot{M} = 10^{-5}\ M_{\odot}\ yr^{-1}$; fractional molecular abundance, $f = 2 \times 10^{-5}$; and asymptotic velocity of the outflow, $v_N = 17$ km s^{-1}. The gas temperature was computed by assuming that H_2O cooling equalled adiabatic cooling. The dust re-emission was modelled by setting I_{BB} equal to a Planck function at 500 ^{o}K. The two models we present here have $r_E = 3 \times 10^{14}$ cm and $r_E = 1.0 \times 10^{14}$ cm, respectively. All other features are the same. In Figures 6 and 7 the run of optical depth with radius for those transitions which invert are shown, and in Figures 8 and 9 the computed line profiles for the masers in the J = 1 → 0 transition of the first excited vibrational state are given. The peaks of these lines would yield antenna temperatures of ~ 10 ^{o}K at the 11-m NRAO radiotelescope at Kitt Peak for a source 100 pc away. We do not give antenna temperatures because the computations are insufficiently precise. In Table 1 we give the fractional sublevel populations at $r = 1.5 \times 10^{14}$ cm for the case $r_E = 3 \times 10^{14}$ cm, and in Table 2 the fractional sublevel populations at $r = 10^{14}$ cm for the case $r_E = 10^{14}$ cm.

V. THE MASERS

The pump cycle for the masers depends, in this situation, on a combination of collisions and radiative transitions. We look just at the excitation of the v = 1 maser transitions, and then discuss the v = 2 masers. In our computations we find a strong tendency to invert the v = 0, J = 1 → 0 transition which can be suppressed by collisions within the ground vibrational ladder. This transition has not been detected, and we use its absence to argue for a high gas temperature near the star, or perhaps a high mass loss rate.

In the region where the masers form the gas temperature, $T_{gas} \sim 10^3$ °K and the particle density (mostly H_2) is $\gtrsim 10^9$ cm^{-3}. The mean rate for pure rotational collisions in SiO is then ~ 1 s^{-1} and for vibrational collisions is $\sim 10^{-5}$ s^{-1}. This must be contrasted with the mean radiative transition rates A/τ (for optically thick lines), which are typically $\sim 10^{-7}$ s^{-1} for the rotational transitions and ~ 1 s^{-1} for the vibrational transitions. We see that collisions dominate the distribution among the rotational levels, and the radiation field determines the excitation of the vibrational levels. To zeroth order then, the population distribution in the rotational levels is thermal at T_{gas}, and in the first excited state the fractional sublevel populations are a constant $\exp\{-h\nu/kT_{ex}\}$ times the corresponding ground state population (cf. Kwan and Scoville 1974). For masers to occur we require $T_{gas} > T_{ex}$.

The radiative transitions between the v = 1 and v = 2 ladders occur more rapidly than the vibrational collisions, but do little to change the distribution of population in the rotational levels in the v = 1 ladder. Similarly, the precise regularity in the line strengths guarantees that radiative absorbtions from v = 0 to v = 2 will not redistribute population

in the v = 1 ladder if that transition is optically thin. In all our calculations this transition is thin, and here we diverge from Kwan's and Scoville's model.

If $T_{gas} > T_{ex}$, then net upward vibrational collisions will occur. These collisions can lead to inversions in the v = 1 ladder, because collisions can exchange angular momentum easily. Suppose that collisions occurred with equal likelihood for $\Delta J = 0, \pm 1$ and never if $|\Delta J| > 1$. There are two collisional routes into the lowest rotational level, but three into all the higher levels. This tends to invert the lowest rotational transition. If we included also $\Delta J = \pm 2$ collisions, there would be three routes into the lowest level, four into the next and five routes into each of the higher levels. In the computations presented here we used the collision term in equation (19). This process depends only on the ability of collisions to exchange angular momentum among molecules. The fractional inversion we might expect from this process would be the ratio of the collision rate between vibrational ladders to the rate within the ladders, multiplied by $\exp\{h\nu/kT_{ex}\}$. It turns out that the masers strongly saturate and the inversion is reduced. The outer edge of the maser region occurs where $T_{gas} \leq T_{ex}$, and the inner edge where the $v = 2 \rightarrow 1$ transition become optically thick.

In the numerical models, we found in general that the collisions would only invert the lower two levels, but that saturation in the $J = 2 \rightarrow 1$ line would produce an inversion in the $J = 3 \rightarrow 2$ line. An example of this is the model presented in Table 1, for which the optical depths in the inversions are plotted in Figure 6. The line seen by a distant observer is plotted in Figure 8. It shows the double peak characteristic of many SiO masers (cf. §II)

but does not have the sharpness seen in many sources. We tried unsuccessfully to produce models in which the two peaks were more clearly separated. In our models the optical depths were always too low, or the inversion occurred over too large a range in radius.

The difference in model II is that the acceleration occurs closer to the star, so that all the processes we describe occur closer to the star. The line profile (Fig. 9) is single peaked. In both models the amplification of the stellar continuum and spontaneous emission were comparable.

Not surprisingly, we find that $T_{gas} > T_{ex}$ for the transition between $v = 2$ and $v = 1$ over a wider range in radius. The inversions in the lower two transitions are often pronounced. However, the results for these computations are less reliable than for the lower transitions because of numerical difficulties in solving the rate equations when the level populations vary by many orders of magnitude. We have included them here (together with the results for $v = 3$) only to demonstrate that this mechanism can work effectively in the higher vibrational levels.

We found in many of the computer models that close to the star there was a region where $T_{gas} < T_{ex}$, using our temperature model. In this region (typically between 7×10^{13} cm and 9×10^{13} cm) the inverse collisional process would strongly invert the $J = 1 \rightarrow 0$ line in the ground vibrational state. This line has not been detected. The inversion disappears if we invoke a high mass loss rate, which would increase T_{ex} so that vibrational collisions could not so effectively compete with rotational collisions. For this to work we required $\dot{M} \geq 2 \times 10^{-5}\ M_{\odot}\ yr^{-1}$.

Some of the SiO emitters do not have very large infra-red excesses (see, e.g., Gehrz and Woolf (1971) and references therein) and probably do not have these very large mass losses. It is most probable that our

temperature model is inadequate. If shocks are travelling outward in this region, the temperature could reach 3000 ^{o}K, hot enough to dissociate H_2 (D_o = 4.48 eV) but not SiO (D_o = 7.8 eV). In the model of Goldreich and Scoville (1976) T_{gas} is higher than our approximate model yields. A sample numerical calculation in which we raised T_{gas} showed that the inversion disappeared when $T_{gas} > T_{ex}$. Note that in our calculations the v = 1 → 0 transitions are only moderately optically thick, because so much of the population is pushed up to high rotational levels. This was apparently overlooked by Kwan and Scoville (1974), and it strengthens our conclusion that the v = 2 → 0 transitions are optically thin.

We constructed models with lower mass loss rates and lower 8μ fluxes. *Since it is most likely that $\dot{M}$ is proportional to the 8μ flux, we discuss* here what happens as we lower the two together. The effect of lowering $\dot{M}$ is to reduce the effect of collisions, while the absolute sublevel populations in the low rotational levels of the ground vibrational state remain very nearly constant. This is because collisions are less effective at exciting to high levels, and at the same time downward radiative transitions are more effective. In this way the v = 1 → 0 lines remain optically thick. However, the excitation temperature of the v = 1 ladder is reduced because of the lower 8μ flux, and consequently the fractional sublevel populations in the v = 1 ladder decrease. The collisional pump cycle becomes much more effective, and thus the inversions become greater and occur over a wider range in radius. The source function is reduced, so that the amplification of starlight becomes more important than the amplification of spontaneous emission. This leads to the production of a singly peaked at negative radial velocities.

Given the uncertainties in the collision rates, we feel unable to predict antenna temperatures from these calculations. However, one result that does come from the computations is that the emitted flux is very insensitive to $\dot{M}$, given the assumption that the 8μ flux is radiated from the dust. Thus we expect the SiO antenna temperature to vary approximately inversely as the square of the distance to the source.

In Paper I we found that the fractional SiO abundance was very low in the envelope at large radii. We computed here a series of models with low SiO abundances and found that the masers became much weaker when we reduced f by more than a factor of 2 or more. This is because the $v = 1 \rightarrow 0$ transitions become optically thin, and the excitation temperature falls drastically. The inversions are still present, but the absolute sublevel populations in the excited vibrational states are so low that the optical gains are less than unity.

VI. DISCUSSION

We have shown above how each of the masers can be pumped, and argues that these masers must form at radii between 10^{14} cm and 2×10^{14} cm. A substantial enhancement of the 8μ flux due to dust re-emission is required to pump the masers. A large number density of SiO molecules is required to achieve sufficient optical depth in the 8μ transitions since the distribution of the level population up the $v = 0$ rotational ladder is so efficient. The flux in the emission lines is insensitive to $\dot{M}$ if the 8μ flux is proportional to $\dot{M}$. If $\dot{M} \lesssim 3 \times 10^{-6}\ M_{\odot}\ yr^{-1}$, we expect a single peaked line at a negative velocity. If $\dot{M}$ is high, we may have single or double peaked lines.

Both single and double peaked lines are observed. Since the infra-red excesses are increasing functions of $\dot{M}$, in those stars with low excesses we should expect only singly peaked lines. This is difficult to test statistically because there are so few objects. However, for those objects whose [3.5μ] - [11μ] colors have been measured by Gehrz and Woolf (1971), those with [3.5μ] - [11μ] < 1.7 (R LMi, RU Hya, RX Boo, R Aql, UX Cyg) have singly peaked lines. (The color of a 2000 ^{o}K black body is [3.5μ] - [11μ] = 1.1.)

The requirement (in our model) of a high SiO abundance must be contrasted with the conclusion of Paper I, that the number density of SiO molecules in the envelope at larger ($> 10^{15}$ cm) radii is surprisingly low. In fact, if $\dot{M} = 10^{-5}\ M_{\odot}\ yr^{-1}$, then the fractional molecular abundance of SiO (cf. Paper I) is typically $f \lesssim 10^{-6}$. This indicates that only a small fraction of the available silicon is in gaseous SiO, whereas the calculations in this paper appear to require the reverse. Abundance computations of Vardya (1966) and Tsuji (1973) also show that in cool oxygen-rich atmospheres most of the silicon is in the form of SiO.

This clearly suggests that the SiO is very efficiently processed into grains once the temperature in the envelope falls to ~ 1000 ^{o}K or below. In this way we can have the high SiO abundance near the star, needed to effectively pump the masers, and the lower SiO abundance in the outer regions of the envelope. Grain formation must be especially efficient in the objects with large infra-red excesses, such as IRC + 100011, and so for the purposes of discussion we adopt the following scenario:

(a) The mass loss rate is $1\text{-}3 \times 10^{-5}\ M_{\odot}\ yr^{-1}$.

(b) Most of the available silicon is in the form of gaseous SiO between the stellar surface and ~ 2×10^{14} cm.

(c) At ~ 2×10^{14} cm grain formation begins and proceeds very efficiently; 90% of the SiO is locked into grains.

(d) Radiation pressure on the grains, which are momentum coupled to the gas, then further accelerates the material outwards.

(e) The grains emit a large number of 8μ photons, which effectively excite the ground vibrational state rotational transitions in SiO, and pump the maser transitions.

Goldreich and Scoville (1976) have argued fairly convincingly for these high mass losses: if one assumes that the infra-red excesses in these stars are due to re-radiation from dust heated by stellar continuum photons, then one can estimate the liminous momentum transfer to the grains. This momentum is then transferred to the gas, which achieves a radial outflow velocity obtainable from the OH maser lines. They obtained $\dot{M} \sim 3 \times 10^{-5}\ M_{\odot}\ yr^{-1}$. Given the numerical calculations in Paper I, and in §VI above, we have to accept the high efficiency in (c) above. This is not unreasonable. If half of the refractory material is already in grains of ~ 10^4 atoms each, then the mean time between collisions with a grain is ~ $10^6(\dot{M}/10^{-5}\ M_{\odot}\ yr^{-1})$ seconds, whereas the convective time at 2×10^{15} cm is ~ 2×10^8 seconds.

There is other evidence that grain formation can effectively remove refractory elements from the gas. Interstellar ultra-violet absorbtion line studies on the Copernicus satellite first indicated substantial depletions (Spitzer and Jenkins (1975), and references therein). The natural interpretation of these depletions is that much of the C, O, Si and Fe is locked into grains. Unfortunately there is at present no model of grain formation that is sound enough to estimate the efficiency of grain formation (see for example, Salpeter 1974a).

The mechanism by which these stars eject mass is not well understood. It is clear that radiative pressure on grains is sufficient to drive the matter off, but the grains cannot form at the stellar surface. Radiation pressure in the photosphere is not responsible (Żytkow 1972). The most promising mechanisms are direct acceleration by shock waves (Slutz 1976) or perhaps an asymmetric mechanism in which grains can form in regions of the photosphere that are temporarily cooled to ~ 1400 ^{o}K (Salpeter 1974b). The Salpeter mechanism would produce a strongly aspherical velocity field in the region where the SiO masers operate, which is somewhat inconsistent with the symmetry of the lines. The shocks that Slutz invokes are seen in the stellar emission lines, and we favor this hypothesis.

The computations presented in §III depend on the assumption that the streaming velocity is a monotonically increasing function of radius. It is possible that shells ejected following a shock wave would decelerate until the grains formed, and were then accelerated out from the star. Olnon (1977) discussed such velocity fields. However, even if the velocity is not monotonic, our calculation will describe at least qualitatively the behaviour of the masers. This is because the masers occur in excited vibrational states, which are only populated to any degree very close to the star. The "local" approximation would suffice because the optical depths in the important transitions for the pump cycle are very low elsewhere in the envelope.

VII. CONCLUSION

The principal conclusion of this paper is that the SiO masers observed around evolved stars occur in levels which are excited by the optically thick absorbtion of 8μ photons, with the inversions being pumped by collisions. The lines are formed very close to the star. The pump cycle is only effective if most of the available silicon is in gaseous SiO. This can be reconciled with Paper I, if grain formation is very efficient.

ACKNWOLEDGMENTS

We thank Peter Goldreich for some useful conversations.

TABLE 1

Fractional sublevel populations for model I at $r = 1.5 \times 10^{14}$ cm. The gas temperature is 912 ^{o}K; 56% of the molecules are in higher rotational levels. The optical depth in the transition $v = 1$, $J = 1 \rightarrow v = 0$, $J = 0$ is 2.64, and in the transition $v = 2$, $J = 1 \rightarrow v = 0$, $J = 0$ is 6.86×10^{-3}.

J	v = 0	v = 1	v = 2	v = 3
0	1.238 ($\times 10^{-2}$)	6.612 ($\times 10^{-4}$)	1.532 ($\times 10^{-5}$)	2.177 ($\times 10^{-7}$)
1	1.236	6.793	1.741	2.178
2	1.219	6.910	1.904	2.178
3	1.214	7.091	1.813	2.160
4	1.195	7.065	1.709	2.141
5	1.169	7.037	1.614	2.119
6	1.140	6.997	1.527	2.986
7	1.119	6.956	1.630	2.990
8	1.078	6.929		
9	1.068	6.898		
10	1.031	6.854		
11	1.016	6.830		

TABLE 2

Fractional sublevel populations for model II at $r = 10^{14}$ cm. The gas temperature is 1086 ^{o}K; 61% of the molecules are in higher rotational levels. The optical depth in the transition $v = 1$, $J = 1 \rightarrow v = 0$, $J = 0$ is 1.78, and in the transition $v = 2$, $J = 1 \rightarrow v = 0$, $J = 0$ is 4.62×10^{-3}.

J	v = 0	v = 1	v = 2	v = 3
0	9.017 ($\times 10^{-3}$)	1.058 ($\times 10^{-3}$)	4.696 ($\times 10^{-5}$)	8.118 ($\times 10^{-7}$)
1	9.017	1.079	4.545	8.207
2	8.984	1.091	4.519	8.211
3	8.932	1.086	4.429	8.202
4	8.865	1.080	4.331	8.151
5	8.751	1.074	4.236	8.009
6	8.608	1.069	4.129	7.812
7	8.514	1.064	4.131	7.961
8	8.476	1.058		
9	8.401	1.051		
10	8.323	1.042		
11	8.267	1.031		

REFERENCES

Balister. M., Batchelor, R. A., Haynes, R. F., Knowles, S. H., McCulloch, M. G., Robinson, B. J., Wellington, K. J., and Yabsley, D. E. 1977, M.N.R.A.S., 180, 415.

Buhl, D., Snyder, L. E., Lovas, F. J., and Johnson, D. R. 1974, Ap. J. (Letters), 192, L97.

_____ 1975, Ap. J. (Letters), 201, L29.

Castor, J. I. 1970, M.N.R.A.S., 149, 111.

Cudaback, D. D., Gaustad, J. E., and Knacke, R. F. 1971, Ap. J. (Letters), 166, L49.

Davis, J. H., Blair, G. N., Van Till, H., and Thaddeus, P. 1974, Ap. J. (Letters), 190, L117.

Deguchi, S., and Iguchi, T. 1976, Publ. Astron. Soc. Japan, 28, 307.

Elitzur, M., Goldreich, P., and Scoville, N. 1976, Ap. J., 205, 384.

Geballe, T. R., and Townes, C. H. 1974, Ap. J. (Letters), 191, L37.

Gehrz, R. D., and Woolf, N. J. 1971, Ap. J., 165, 285.

Goldreich, P., and Scoville, N. 1976, Ap. J., 205, 144.

Hedelund, J., and Lambert, D. L. 1972, Astrophys. Letters, 11, 71.

Herzberg, G. 1950, Spectra of Diatomic Molecules (Van Nostrand, New York).

Kaifu, N. Buhl, D., and Snyder, L. E. 1975, Ap. J., 195, 359.

Kwan, J., and Scoville, N. 1974, Ap. J. (Letters), 194, L97.

Kwok, S., Gilman, R. C., and Woolf, N. J. 1975, Ap. J., 198, 583.

Lucy, L. B. 1971, Ap. J., 163, 95.

Morris, M., and Alcock, C. 1977, Ap. J., in press.

Olnon, F. M. 1977, "Shells Around Stars" (Ph.D. thesis, University of Leiden).

Raymonda, J. W., Muenter, J. S., and Klemperer, W. A. 1970, J. Chem. Phys., 52, 3458.

Salpeter, E. E. 1974a, Ap. J., 193, 579.

_____ 1974b, Ap. J., 193, 585

Slutz, S. 1976, Ap. J., 210, 750.

Snyder, L. E., and Buhl, D. 1974, Ap. J. (Letters), 189, L31.

_____ 1975, Ap. J., 197, 329.

Sobolev, V. V. 1960, Moving Envelopes of Stars (Harvard University Press).

Spencer, J., and Schwartz, P. R. 1975, Ap. J. (Letters), 199, L111.

Spitzer, L., and Jenkins, E. B. 1975, Ann. Rev. Astron. and Ap., 13, 133.

Thaddeus, P., Mather, J., Davis, J. H., and Blair, G. N. 1974, Ap. J. (Letters), 192, L33.

Tsuji, T. 1973, Astron. and Ap., 23, 411.

Vardya, M. S. 1966, M.N.R.A.S., 134, 347.

Zappala, R. R., Becklin, E. E., Matthews, K., and Neugebauer, G. 1974, Ap. J., 192, 109.

Zel'dovich, Ya. B., and Raizer, Yu, P. 1966, Physics of Shock Waves and High Temperature Phenomena (Academic Press, New York).

Żytkow, A. N. 1972, Acta. Astronomica, 22, 103.

FIGURE CAPTIONS

Fig. 1. The geometry of a star (radius r_c) and a typical surface of constant Doppler shift to a distant observer. The surface intersects the symmetry axis at $r_m(v)$. The amplification of starlight can only occur out to $r_p(v)$.

Fig. 2. The family of streaming velocity curves (solid lines) and the logarithm of their logarithmic derivatives (dotted lines) for the analytic form given by equation (12). The parameter r_E takes the values (1) $r_E = 0.5$, (2) $r_E = 1.0$, (3) $r_E = 2.0$, (4) $r_E = 3.0$, (5) $r_E = 5.0$ and (6) $r_E = 10.0$. The dashed line shows the (appropriately scaled) streaming velocity obtained by Goldreich and Scoville (1976).

Fig. 3a. The integrals P_A are plotted versus radial velocity. Note that V increases to the right, but only negative velocities are plotted. These plots are symmetric in V. Each curve has $\tau_M = 3$ and $r_M = r_E$. The different curves are for the family of streaming velocity curves shown in Figure 2, and are numbered accordingly. The curves as drawn are all normalized to a maximum value unity. The maxima in fact are (1) 6.69 E - 1, (2) 2.95 E + 1, (3) 1.66 E + 2, (4) 3.83 E + 2, (5) 1.73 E + 3 and (6) 1.41 E + 4.

Fig. 3b. The same as for Figure (3b) but for P_B. $P_B = 0$ for $V > 0$. The maxima are (1) 1.26 E - 1, (2) 2.02, (3) 1.67 E + 1, (4) 5.57 E + 1, (5) 2.08 E + 2 and (6) 7.26 E + 2.

Fig. 4a. The integrals P_A, where each curve has $r_E = r_M = 5.0$. The curves are labelled with the optical depth parameter τ_M. The maxima of the curves are (1) 1.32 E + 2, (2) 4.49 E + 2, (3) 1.73 E + 3 and (4) 7.48 E + 3.

Fig. 4b. The same as Figure 4a, but for P_B. The maxima are (1) 4.93, (2) 3.42 E + 1, (3) 2.08 E + 2 and (4) 1.24 E + 3.

Fig. 5a. The integrals P_A, where each curve has $r_E = 2.0$ and $\tau_M = 2.0$. The different curves have (1) $r_M = 0.0$, (2) $r_M = 2.0$, (3) $r_M = 4.0$ and (4) $r_M = 6.0$. The maxima are (1) 9.81, (2) 6.46 E + 1, (3) 4.02 E + 3 and (4) 5.10 E + 10.

Fig. 5b. The same as for Figure 5a, but for P_B. The maxima are (1) 6.13 E - 1, (2) 5.79, (3) 3.72 E + 3 and (4) 1.14 E + 10.

Fig. 6. The optical depths in the lowest three rotational transitions of the v = 1 ladder (solid lines) and the lowest two in the v = 2 ladder (dotted lines) for model I.

Fig. 7. The optical depths in the lowest three rotational transitions of the v = 1 ladder for model II. The v = 2 transitions do not invert.

Fig. 8. The maser line profile seen by a distant observer for model I. The ordinate has an arbitrary scale (see discussion in text).

Fig. 9. The maser line profile seen by a distant observer for model II.

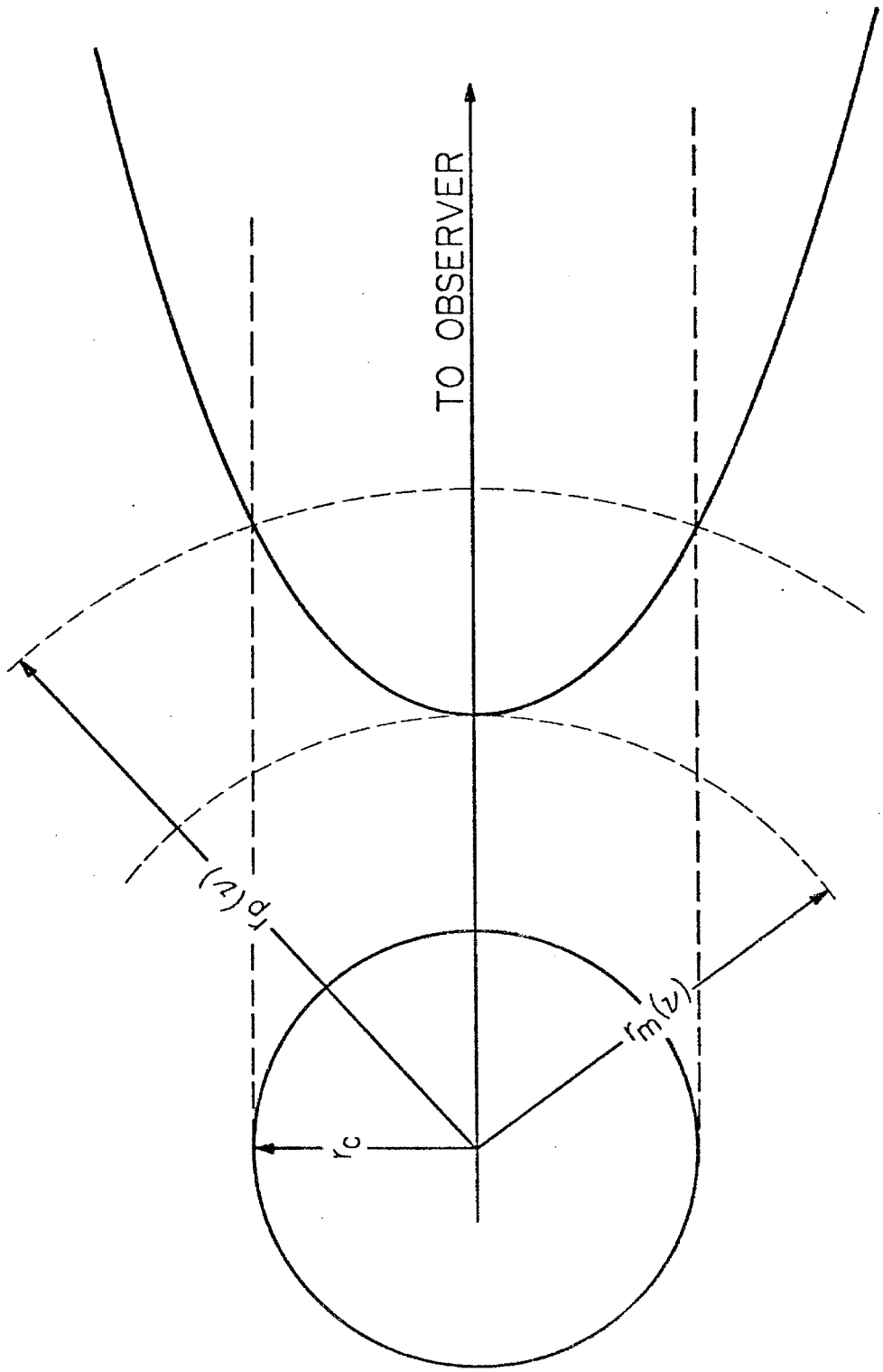

Figure 1

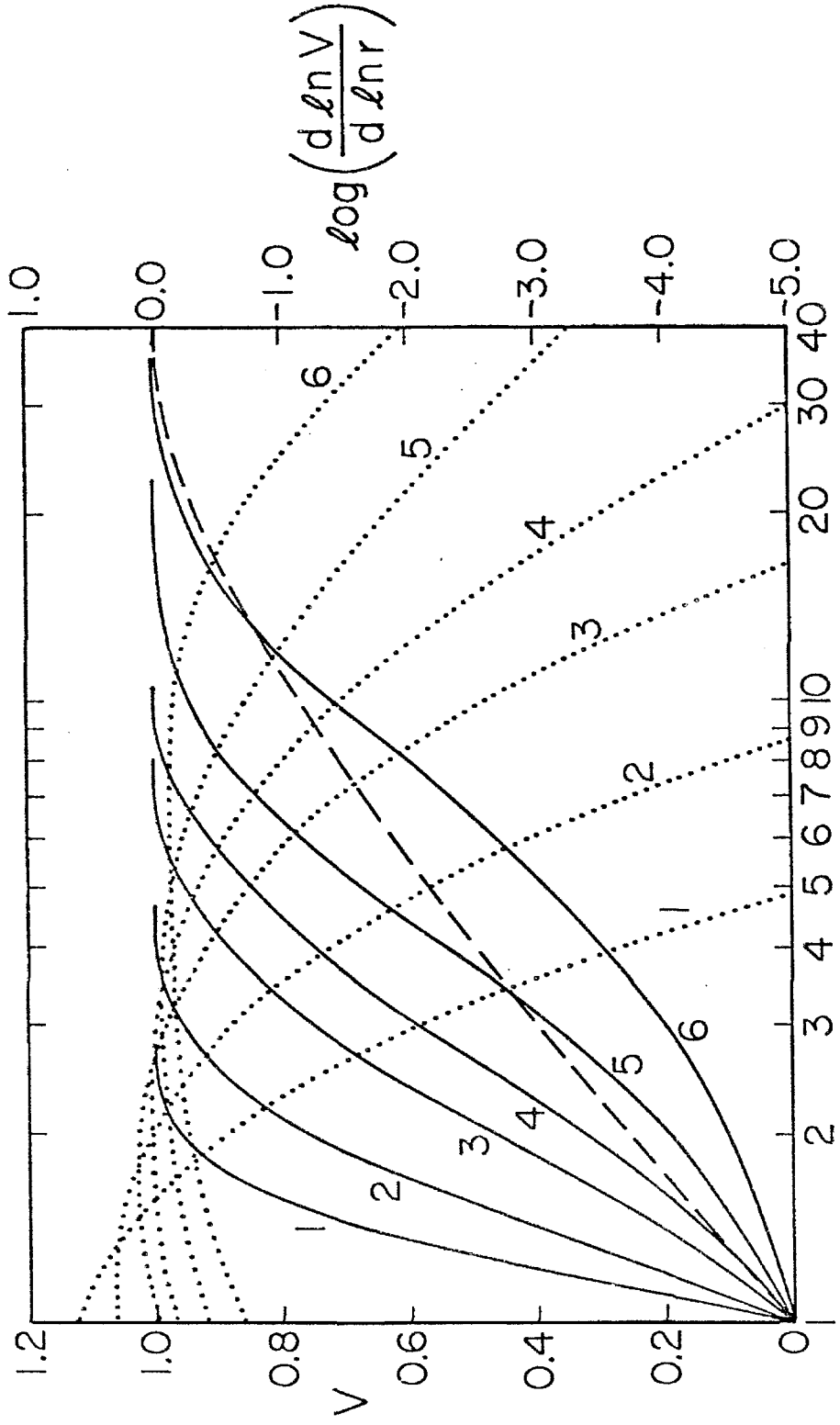
log (d ln V / d ln r)
1.0
0.0
-1.0
-2.0
-3.0
-4.0
-5.0
6
5
4
3
2
1
1.2
1.0
0.8
0.6
0.4
0.2
0
V
1
2
3
4
5
6
2
3
4
5
6
7
8
9
10
20
30
40
r

Figure 2

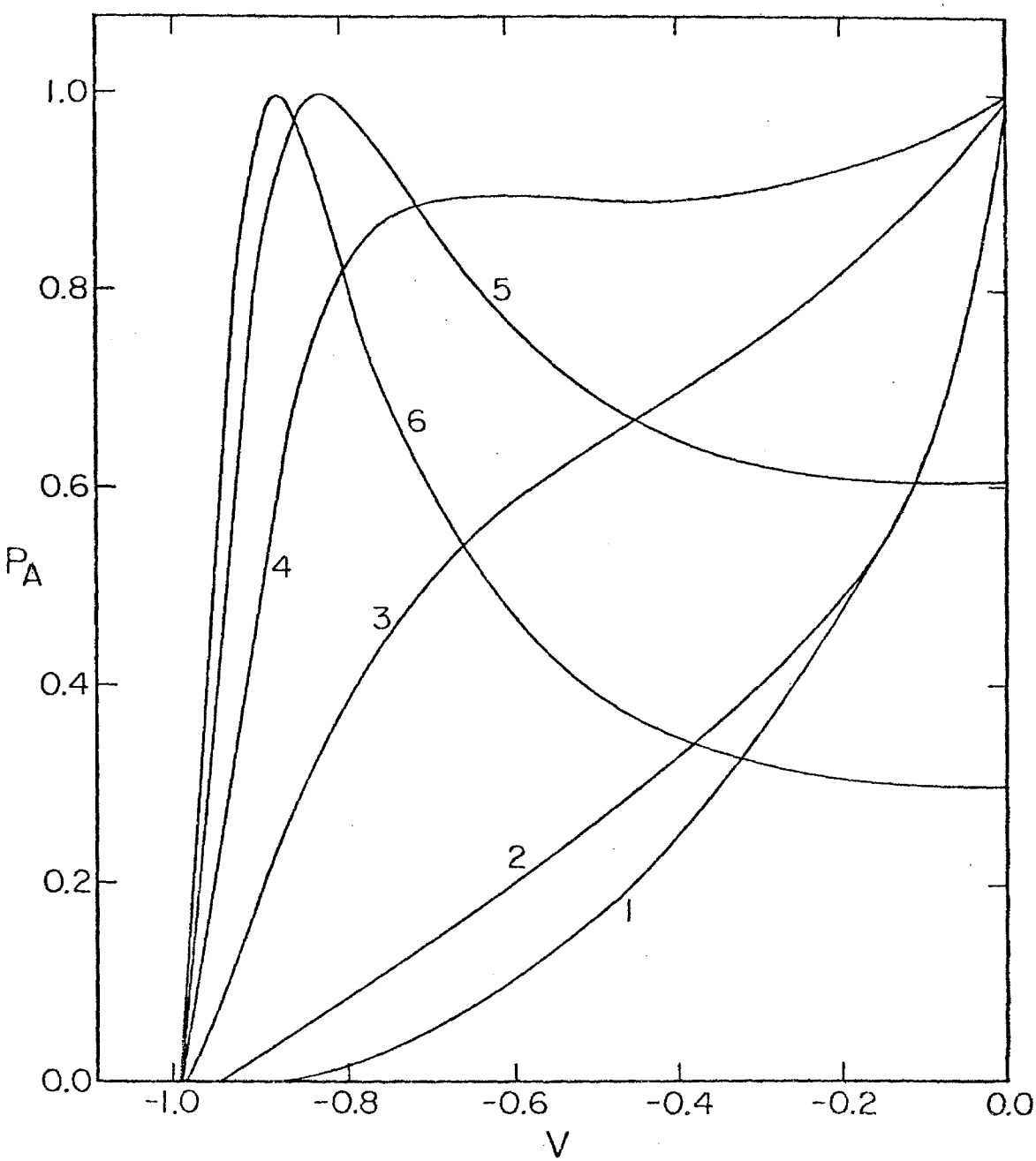

Figure 3a

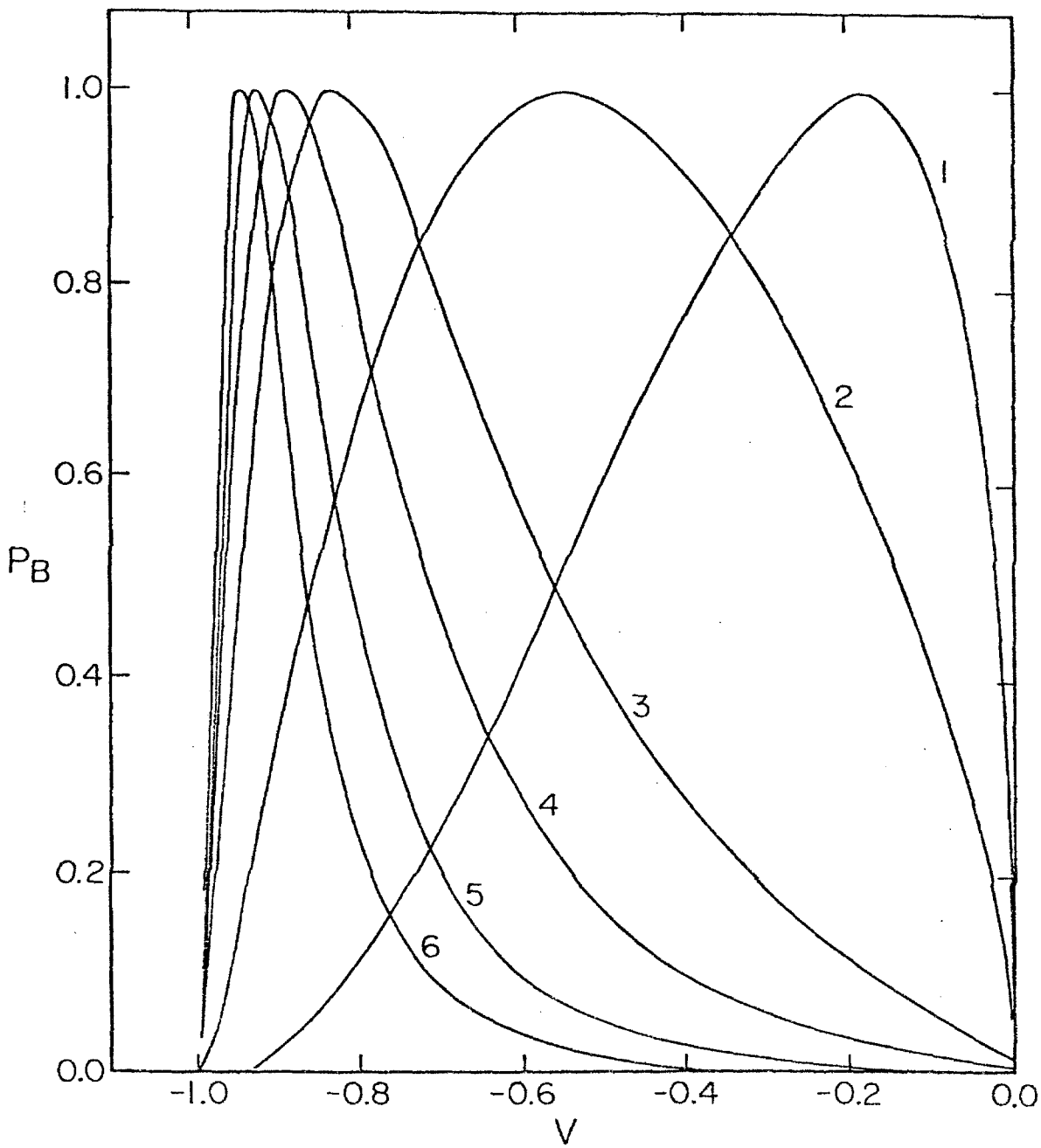

Figure 3b

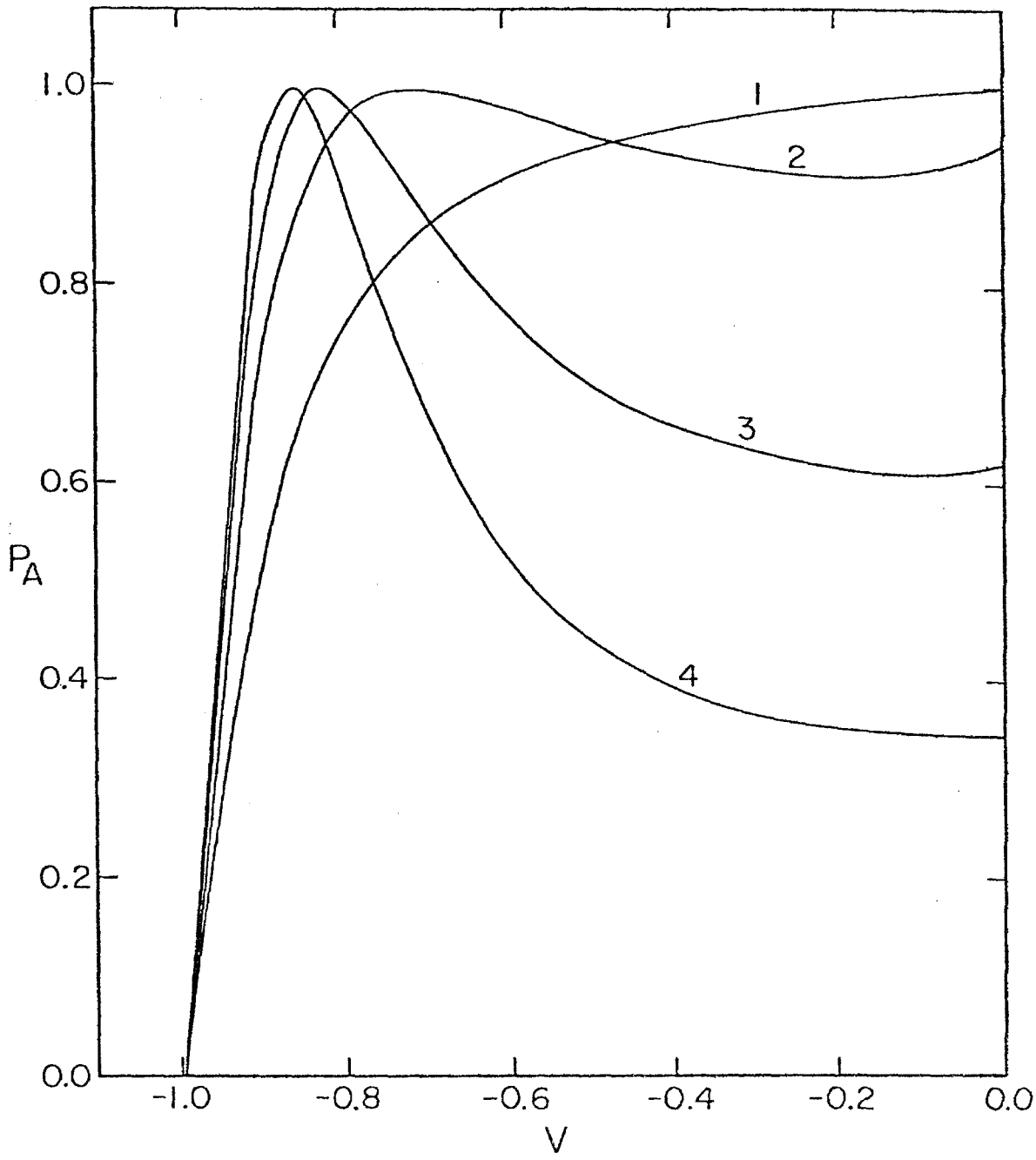

Figure 4a

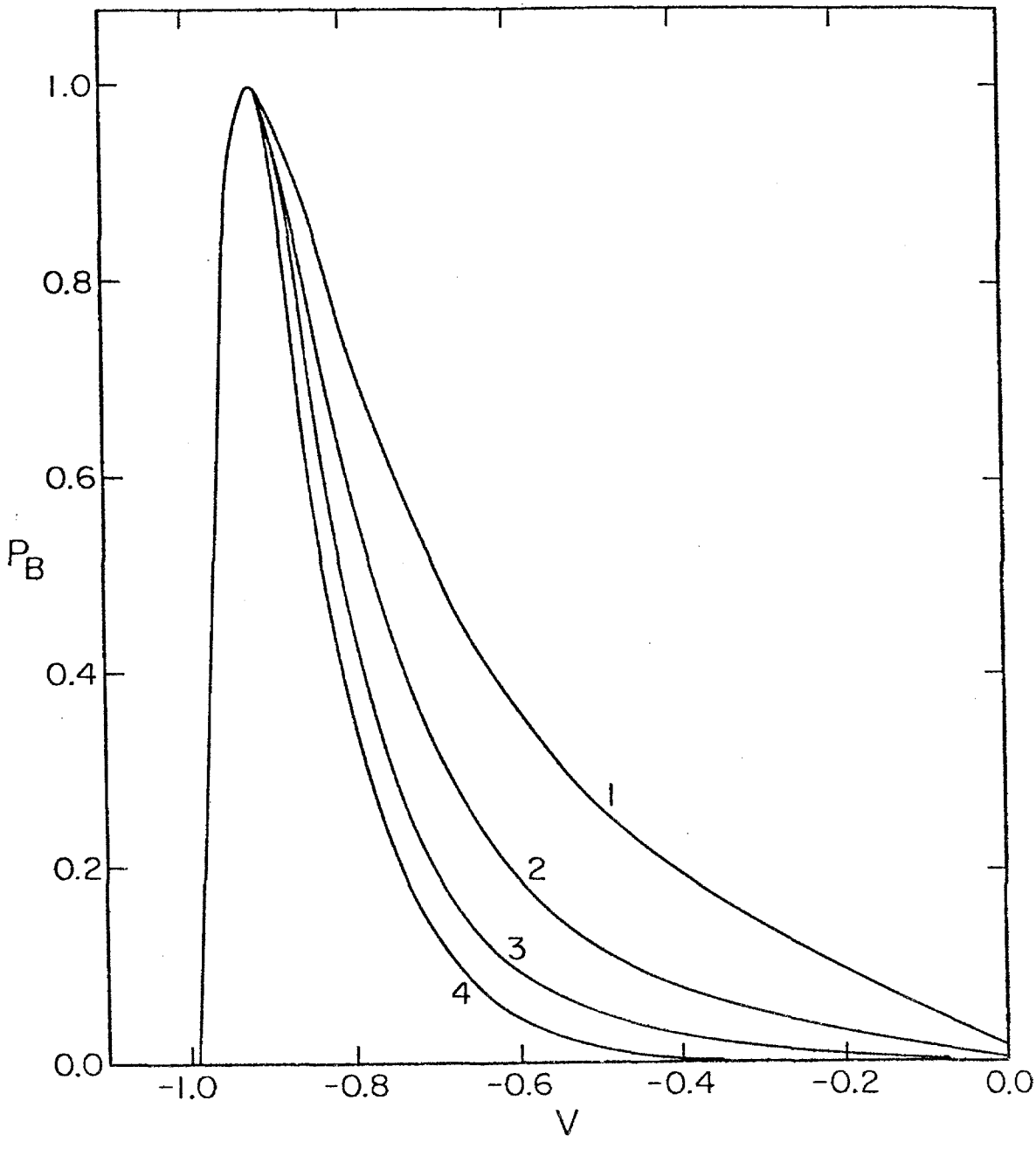

Figure 4b

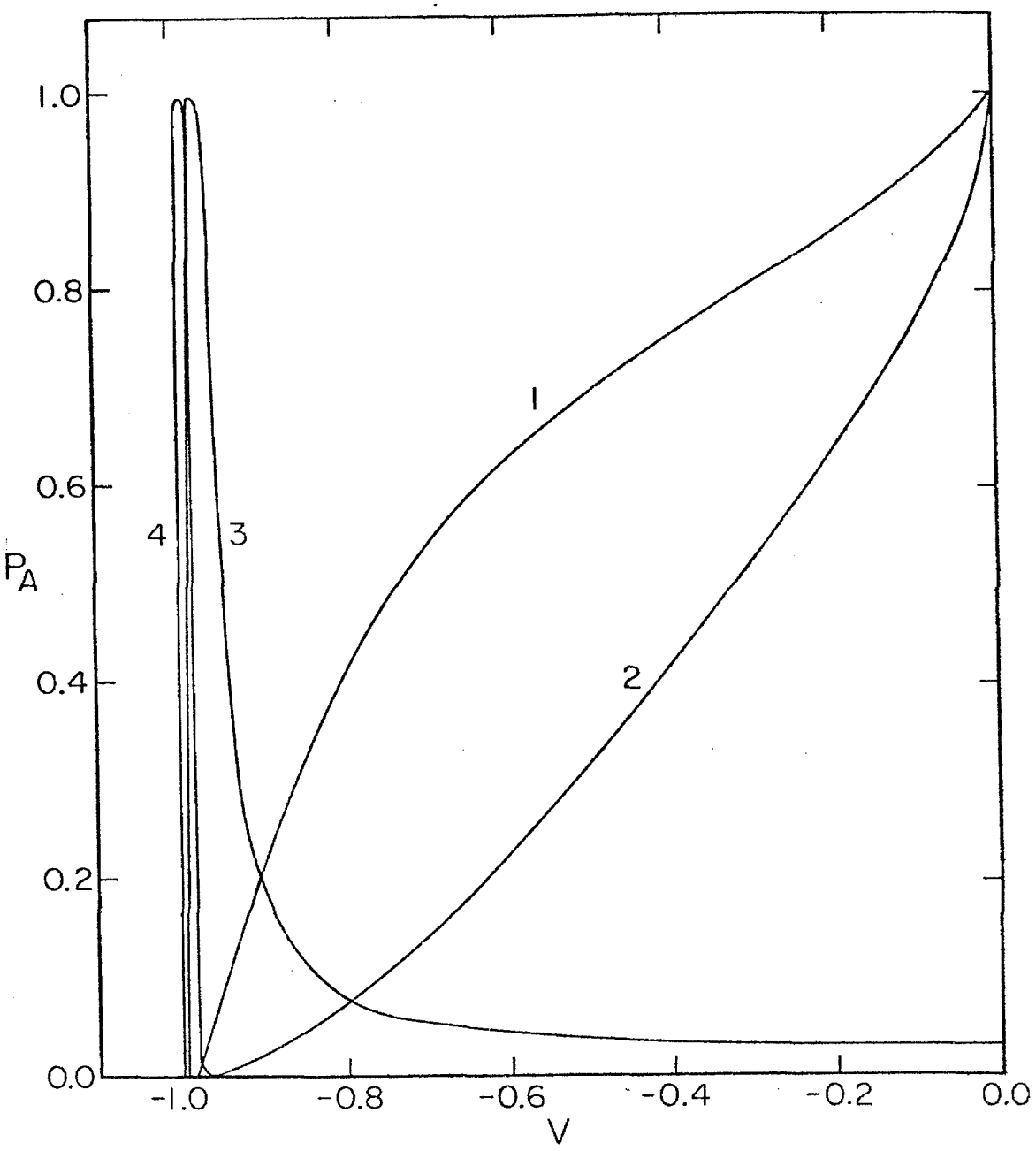

Figure 5a

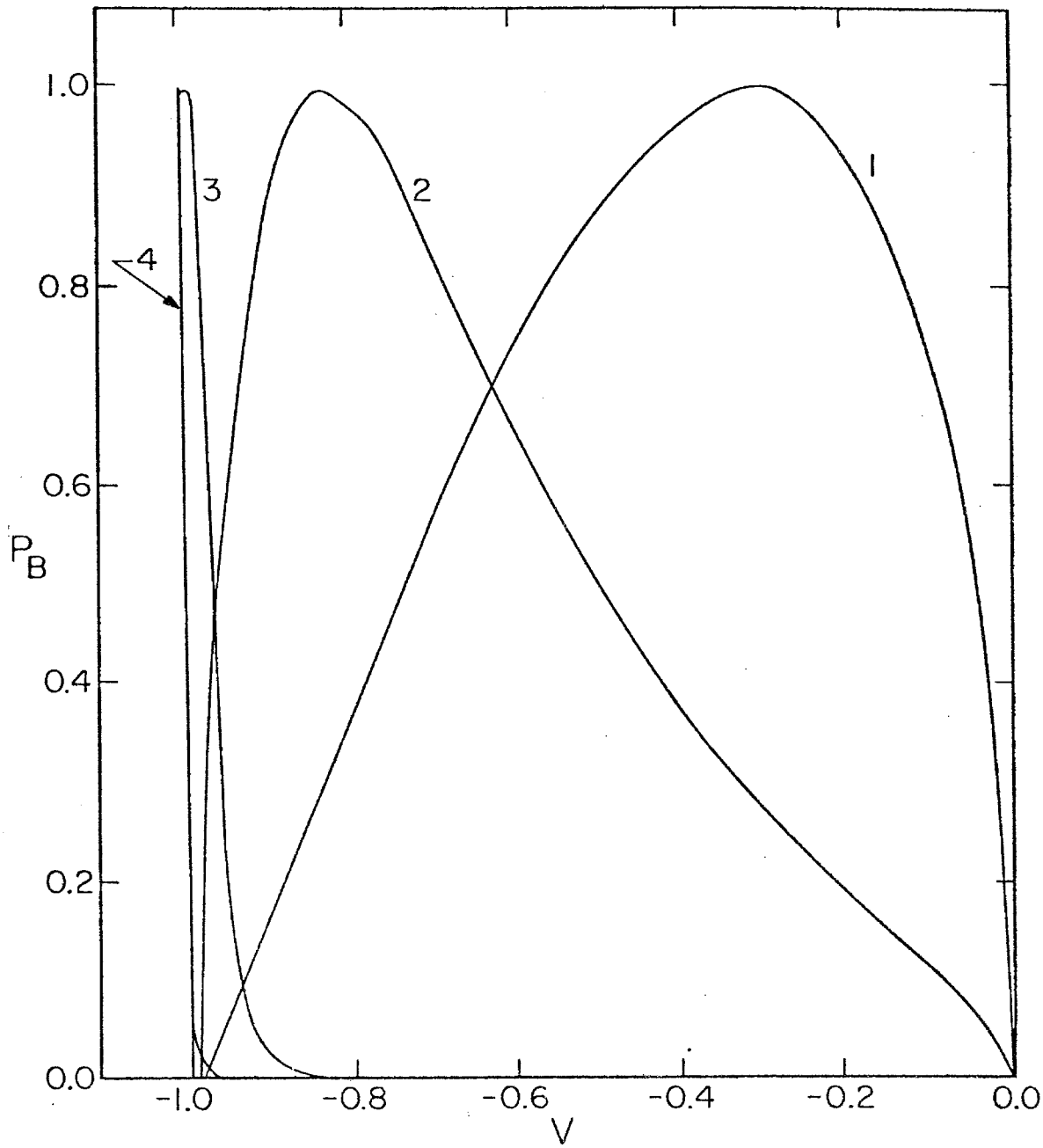

Figure 5b

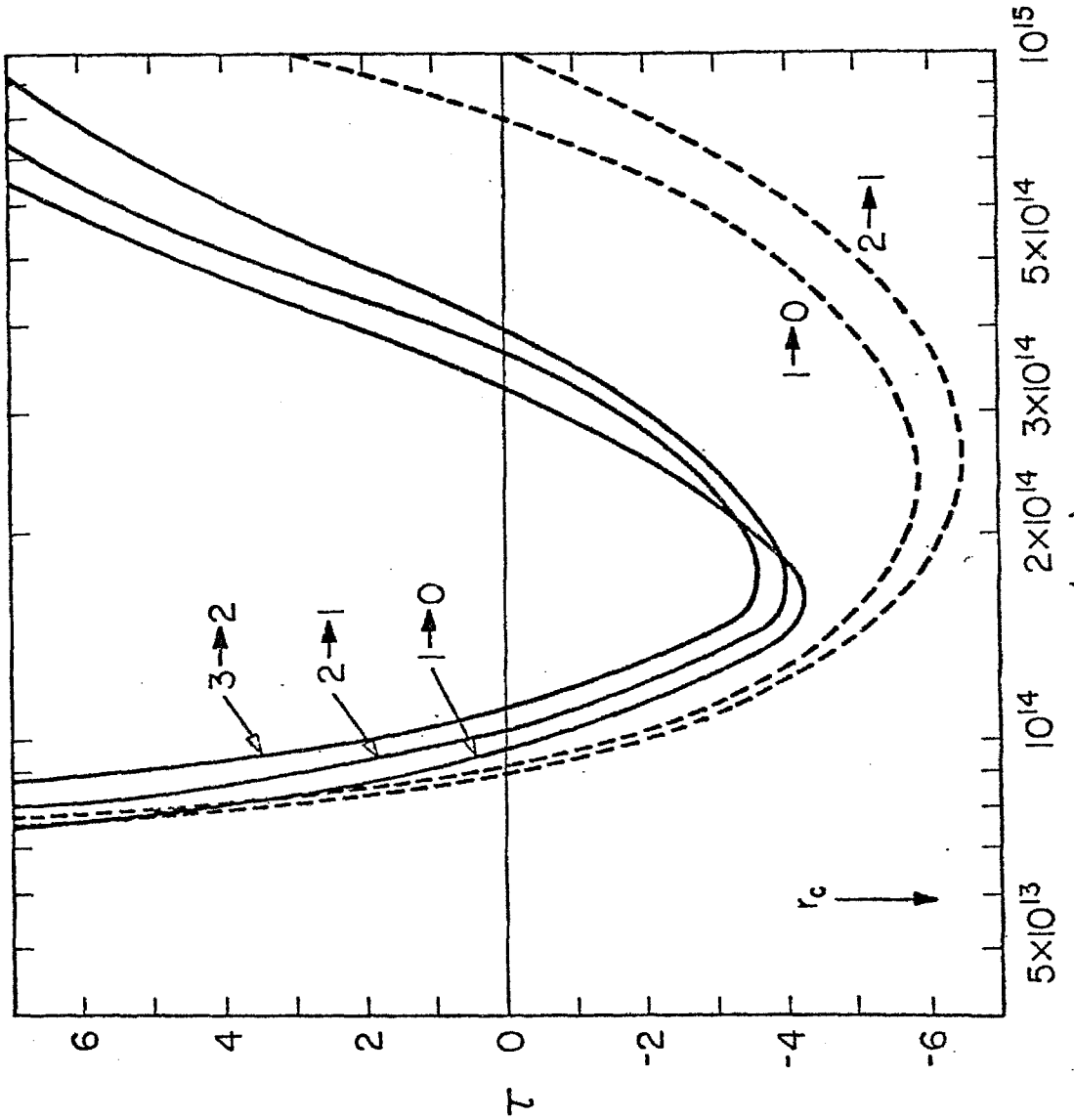
τ
6
4
2
0
-2
-4
-6
r (cm)
5×10^13
10^14
2×10^14
3×10^14
5×10^14
10^15
r_c
3→2
2→1
1→0
1→0
2→1

Figure 6

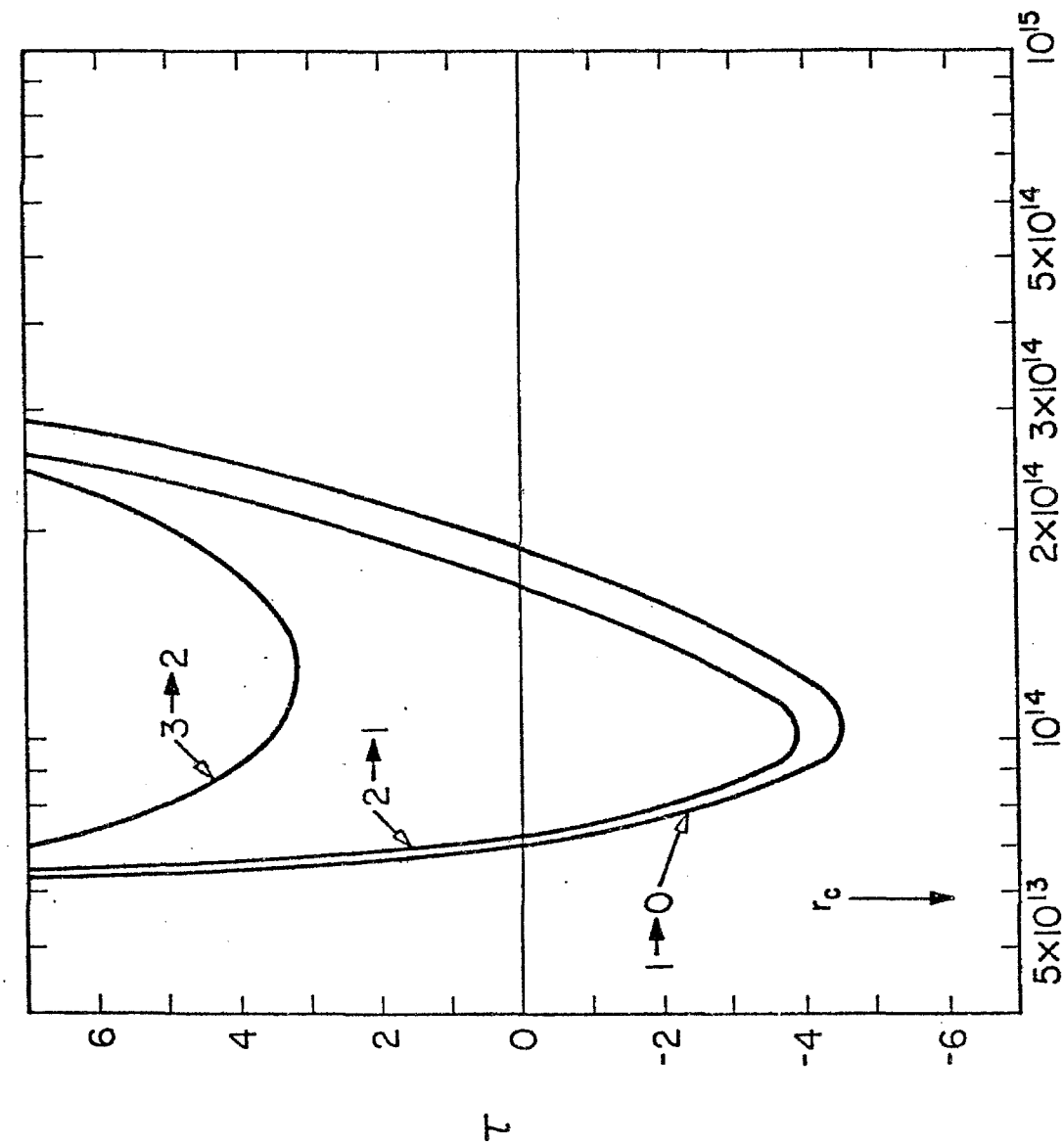

Figure 7

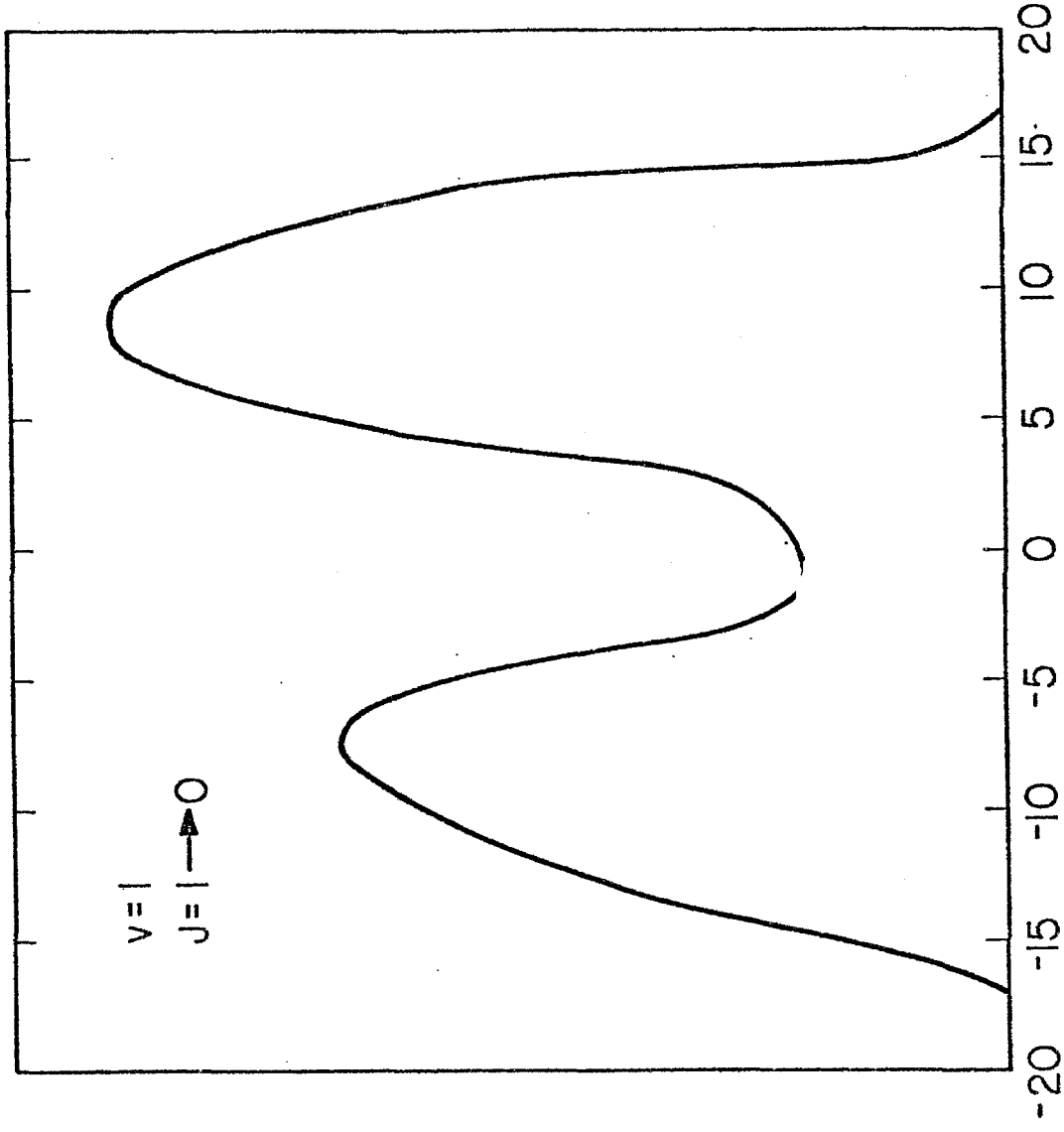

Figure 8

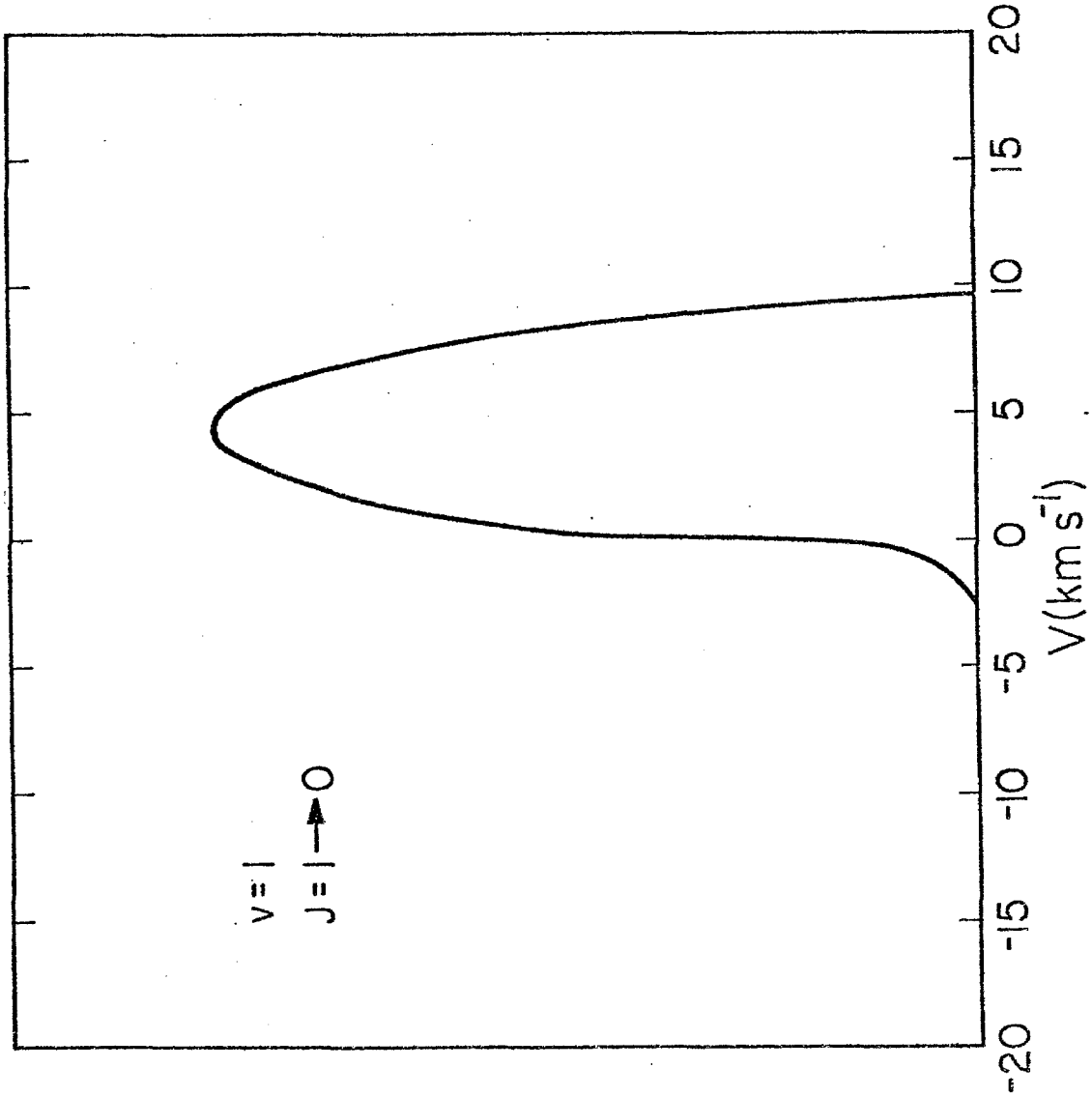

Figure 9